WIDEBAND REFLECTARRAY USING COMPACT COUPLED ELEMENT AND RECTIFYING ANTENNA COMBINED WITH REFLECTARRAY

A Dissertation

by

SEONG WON OH

Submitted to the Office of Graduate Studies of
Texas A&M University
in partial fulfillment of the requirements for the degree of

DOCTOR OF PHILOSOPHY

August 2011

Major Subject: Electrical Engineering

WIDEBAND REFLECTARRAY USING COMPACT COUPLED ELEMENT AND RECTIFYING ANTENNA COMBINED WITH REFLECTARRAY

A Dissertation

by

SEONG WON OH

Submitted to the Office of Graduate Studies of
Texas A&M University
in partial fulfillment of the requirements for the degree of

DOCTOR OF PHILOSOPHY

Approved by:

Chair of Committee,	Kai Chang
Committee Members,	Robert D. Nevels
	Laszlo Kish
	Ping Yang
Head of Department,	Costas N. Georghiades

August 2011

Major Subject: Electrical Engineering

ABSTRACT

Wideband Reflectarray Using Compact Coupled Element and Rectifying Antenna Combined with Reflectarray. (August 2011)

Seong Won Oh, B.S., Republic of Korea Naval Academy;

B.S., Yonsei University;

M.S., Pohang University of Science and Technology

Chair of Advisory Committee: Dr. Kai Chang

The reflectarray has been considered as a suitable candidate to replace the conventional parabolic reflectors because of its high-gain, low profile, and beam reconfiguration capability. Narrow bandwidth of the reflectarray is the main obstacle for the various uses of the reflectarray. The wide band element with a large phase variation range and a linear phase response is one of the solutions to increase the narrow bandwidth of the reflectarray. Several elements with a large phase range and a linear response have been developed, but their configurations are complex.

Simple methods have been investigated in this dissertation to develop wide band elements. A microstrip ring and slot element with a large phase range is introduced and modified for a better linear response. A coupled element with a linear response has been developed. A method is proposed to design a two-layer reflectarray with multi-resonant elements of various sizes for wideband operation. The element dimensions are adjusted by Particle Swarm Optimization routine to achieve the appropriate phase distribution for

a predetermined frequency band. In another approach to increase the operation bands, a six-band reflectarray has been developed.

As a new application of a reflectarray, a rectifying reflectarray, which is composed of a rectenna and a reflectarray, is introduced in this dissertation. The reflectarray directs RF energy from its aperture to the rectenna located on the feed point of the reflectarray. This configuration eliminates complex feeding networks and design difficulties of the conventional rectenna array.

A Double Sided Parallel Strip Line (DSPSL) is adapted for the feeding network of the Archimedean spiral antenna. The DSPSL operate very well to feed the Archimedean spiral antenna over the bandwidth.

The research presented in this dissertation suggests useful techniques for wideband reflectarrays, wireless power transmission, and wideband antenna designs.

DEDICATION

To my parents, wife, daughters,

and

Republic of Korea Navy

ACKNOWLEDGEMENTS

I would like to express my deepest appreciation to Dr. Kai Chang for his support and guidance throughout my Ph.D. education at Texas A&M University. I also appreciate Dr. Robert D. Nevels, Dr. Laszlo Kish and Dr. Ping Yang for serving as my committee members and for their helpful comments.

I would also like to thank Mr. Ming-Yi Li for his technical assistance. I would like to express thanks to Dr. John Huang at the Jet Propulsion Laboratory and Dr. Chulmin Han at Ethertronics and Dr. Shih-Hsun Hsu at AOI Inc for their helpful instructions and comments for the reflectarray design. I gratefully acknowledge Mr. Jeongkyu Lee, Mr. Chanho Kim, Mr. Travis Eubanks, Mr. Jonathan Hansen, Mr. Dongjin Jeong and other members of the Electromagnetics and Microwaves Laboratory at Texas A&M University for invaluable discussions. My sincere thanks go to the Republic of Korea Navy for their support.

Lastly, I would like to express my deep appreciation to my parents and my wife's parents for their constant love, encouragement, and support. Finally, I would like to thank my family, especially my wife, for their love, support, and patience.

TABLE OF CONTENTS

Page

CHAPTER Page

CHAPTER Page

LIST OF FIGURES

Page

Page

Page

Page

Page

LIST OF TABLES

Page

CHAPTER I

INTRODUCTION

1.1 Background

For many decades, large reflector antennas have been widely used in high gain applications such as satellite communications, radars, radio astronomy, and deep-space communications. The reflector antenna features high gain over wide frequency ranges. However, their curved surface is an obstacle for some applications that require small volume, low profile, and mounting simplicity, because the curved geometry result in heavy weight, bulky size, and manufacturing difficulties. Also, the capability of pattern reconfiguration, beam steering and beam shaping, is limited without mechanical devices.

A class of antennas, called a reflectarray, was introduced by D.G. Berry in 1963[1]. It combines the versatility of the array that the array can produce variable radiation pattern with the simplicity of reflector that the complex and loss feeding network is not required. A reflectarray consists of many unit antenna elements placed on a grid and a main feed antenna. After developing microstrip patch antennas, a reflectarray using microstrip patch elements, called a microstrip reflectarray, has emerged as an alternative of high-gain reflector antennas, especially, parabolic reflector antennas. This microstrip reflectarray antenna has same merits with microstrip antennas such as manufacturing

---

This dissertation follows the style of *IEEE Transactions on Antennas and Propagation*.

simplicity, light-weight, and low- profile, and it also have merits of the phased array such as the beam scanning capability. So microstrip reflectarrays have been intensively studied.

However, one drawback associated with the reflectarray antenna is its inherent narrow bandwidth due to the limited bandwidth of the microstrip element and the differential spatial phase delays [2, 3]. To overcome this narrow bandwidth of the reflectarrays, multi-band configuration of the reflectarrays [4-6] and wide-band reflectarray are presented [7-9].

Another application of the reflectarray is microwave wireless power transmission (WPT). The primary source of energy is now fossil fuels like oil and natural gas, and it has been in short supply. As the amount of fossil fuels has been decreasing, reusable energies obtained from wind, sun, and tide have been attracted as new energy sources. WPT as well as reusable energy have been focused as one of the technologies for solving the world energy problems. WPT will make an important role in transmitting the energy generated from reusable source.

In WPT, the rectenna which is rectifying circuit integrated with an antenna is the key component. The rectenna which means '*rectifying antenna*' was developed in the 1960's by W.C. Brown. The rectenna combined a half-wave dipole antenna and a single diode to convert 2.45 GHz RF to DC. Brown achieved 90.6% conversion efficiency using GaAs-Pt shottky barrier diode and aluminum bar dipole [10]. During oil crisis, the concept of WPT extend to solar power satellites (SPS) and solar power transmission (SPT) [11, 12]. The SPS collects sun's radiation energy in space and transfers it to

ground stations on the earth using microwave power transmission technology. The demonstration of a large-scale wireless power transmission was conducted in 1975 by the Jet Propulsion Laboratory and Raytheon, which built a 18 x 24 ft^2 rectenna array with 5,000 elements working at 2.45 GHz [13]. After the demonstration, several measurements were conducted in Japan and the United states. For higher DP power output, rectennas were combined into several array types. However, the rectenna array designs have some difficulties because of lossy feeding networks and coupling between neighborhood elements.

1.2 Dissertation organization

This dissertation presents a several topics including multi-band reflectarray, wide-band microstrip reflectarrays using elements with linear phase response, a wide-band reflectarray optimized by Particle Swarm Optimization techniques, rectenna combined with a reflectarray, and spiral antenna fed by Double Sided Parallel Strip Line (DSPSL).

Chapter II reviews the fundamental theory of the reflectarray based on parabolic reflector geometry. Theoretical analysis for center-fed reflectarray, offset-fed reflectarray, simulation setup using a waveguide approach, and efficiency of the reflectarray, are presented.

Chapter III deals with microstrip reflectarrays achieving large reflection phase range. Variable microstrip ring and slot element is proposed, and it shows large phase variation range of 682º on single layer. Simple technique to add a circular slot on ground plane increases the phase range almost twice than a conventional ring element. To get a linear

response, a modified microstrip ring and slot element is proposed. This element shows linear phase response with same phase variation range.

Chapter IV proposes a coupled element composed of a split ring and a strip line as a reflectarray unit cell. The two components in the element are coupled through gaps, and the element shows linear response which results in wide 3-dB gain bandwidth of 19%.

Chapter V reviews Particle Swarm Optimization technique, and introduces a wideband reflectarray using the optimization routine. The each element on the reflectarray is adjusted to achieve the required phase distribution in a predetermined frequency band. The prototype reflectarray shows wide bandwidth and gain stability improvements in the given band.

Chapter VI presents a six-band reflectarray configuration on two layers. The elements of 6.6, 18.7, 57.5, 52.5, 166, 183.3 GHz are located on top and bottom layers. Each substrate layer accommodates three frequency bands. The possibility of this configuration, the achievable phase range and the coupling effect, is investigated.

Chapter VII introduces a new class of rectenna configuration combined with a reflectarray. The main purpose of this configuration is to reduce the complex feed network in a rectenna array. A wireless power transmission theory and system are reviewed. A high gain rectenna based on CPS structure is presented. A quadruple pentagonal loop antenna achieves a high gain of 12.5 dBi. The proposed antenna is combined with rectifying circuit, and located on the feed point of the reflectarray. The combination shows the conversion efficiency of 71%.

Chapter VIII proposes a DSPSL-fed Archimedean spiral antenna. Using wide bandwidth characteristics of Double Sided Parallel Strip Line, the spiral antenna shows wide bandwidth from 2.5GHz to 20GHz.

CHAPTER II

FUNDAMENTALS OF REFLECTARRAYS

2.1 Introduction

In this chapter, some basic theoretical aspects concerning reflectarrays are described, and then a method to calculate a reflection phase from a reflected wave is introduced. The fundamental theory of the reflectarray in this section is cited from [3, 14]. Fig. 1 shows the geometry of a parabolic reflector and a microstrip reflectarray. Contrary to a metallic curved surface of parabolic reflector, a reflectarray consists of a flat array of microstrip radiating elements, printed on a grounded substrate. A feed antenna of both antennas is located at the focal point of a parabolic curve, and they illuminate the curved reflector or the array. When the wave from the feed antenna is incident on the reflectarray surface, the elements of the reflectarray will reradiate the incident wave into the space. However as can be seen from Fig. 1 (b), the incident path lengths for the field propagating from the feed antenna to the elements are different. Therefore the reradiated field will not be coherent in a desired direction. In a reflectarray, the path adjustment of different rays is done by the array elements instead of geometrical shape of the parabolic reflector.

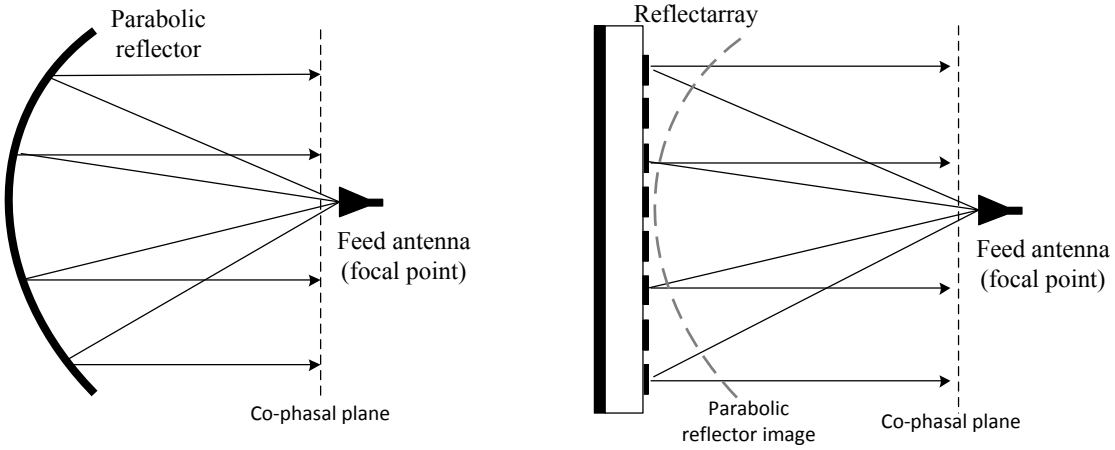

(a) Parabolic reflector (b) Microstrip reflectarray

Fig. 1. Parabolic reflector as compared to microstrip reflectarray

The key to the reflectarray design is to adjust the reflection phase of each element to compensate for the path differences so that the reradiated fields from each element would be collimated towards a specific direction.

2.2 Front-fed reflectarray

The analysis is derived by comparing the configurations of a parabolic reflector and a flat microstrip reflectarray. Fig. 2 shows the block diagram of a flat reflectarray with its virtual parabolic curve. An incident plane wave strikes the parabolic reflector's metal surface and bounces to a focal point a distance f above the center of the parabolic reflector. Each reflectarray elements are located at a position (x', y') from the center of the array (0,0). The distance between the focal point and any antenna element is denoted as r_{mn}. The angle $\theta^{'}$ is the angle between the path connecting the focal point and the array center and the path connecting the focal point and the antenna element.

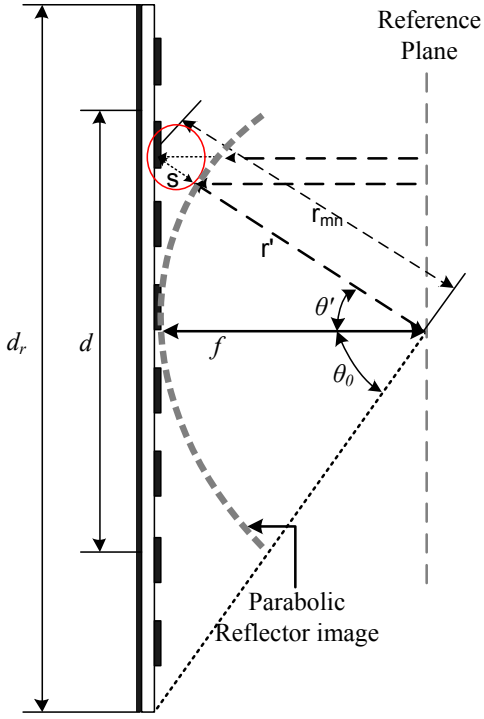

Fig. 2. Path calculation of reflectarray

The dimension of the reflector (*d)* and the largest angle (θ_0) from the center of the parabolic reflector to its edge are related [15] as

$$\theta_0 = \tan^{-1}\left(\frac{\left|0.5\frac{f}{d}\right|}{\left(\frac{f}{d}\right)^2 - \frac{1}{16}}\right) \tag{1}$$

From equation(1), the diameter of the reflectarray can be determined by

$$d_r = 2f\tan(\theta_0) \tag{2}$$

The angle $\theta^{'}$ can also expressed as

$$\theta' = \tan^{-1}\left(\frac{\sqrt{x'^2 + y'^2}}{f}\right) \tag{3}$$

The distance from the focal point to any point on the parabolic surface is [15]

$$r' = \frac{2f}{1+\cos\theta'} \tag{4}$$

For any angle θ', the distance from the reference plane of the reflectarray to the focal point is ($s + s \cos \theta'$) longer than the corresponding ray trace from the reference plane of the parabolic dish to the focal point. This additional path length must be compensated in the design of the reflecting element array in order to provide the parabolic phase front across the surface of the array. The path length in radians is

$$\Delta\ell \qquad s\cos\theta') = \frac{2\pi f_0}{c}(s + s\cos\theta') \tag{5}$$

where f_0 is the design frequency of the array and c is the speed of light. The distance s is equal to

$$s = \frac{f}{\cos\theta'} - r' \tag{6}$$

The antenna elements are designed properly to compensate for the additional path lengths Δl. Once the field reflected from identical elements in the infinite array is known, the equation to find out the phase of the reflected field at the n-elements can be written as:

$$\frac{2\pi f_0}{c}(s + s\cos\theta') - \varphi_n = 2\pi N \tag{7}$$

$$\varphi_n = ang(\bar{E}_n) \tag{8}$$

where φ_n is the phase of the reflected field at the n-elements, and $N = \{1, 2, 3...\}$ is an integer. The equation (7) states that the total phase from the feed to an aperture in front of the reflectarray should be constant.

2.3 Offset-fed reflectarray

The analysis to calculate the needed phase delay is derived based on the comparison of the geometrical configurations between an offset parabolic reflector and a flat microstrip reflectarray. The block diagram of the reflectarray with its virtual parabolic surface is shown in Fig. 3. The microstrip reflectarray elements are placed at (x_{re}, y_{re}, z_{re}) in the (x, y, z) coordinate system.

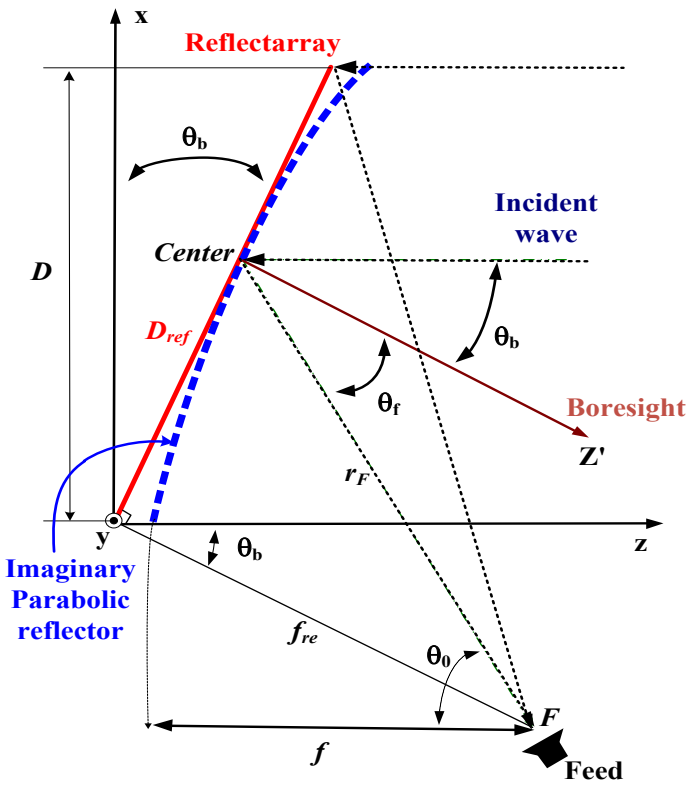

Fig. 3. Offset reflectarray block diagram

Referring to Fig. 3 and specifying the reflectarray's dimension D_{ref}, the vertical distance from the reflectarray's lower edge to the feed f_{re}, and the desired scan angle θ_b, the phase center of the feed is

$$x_f = -f_{re}\sin(\theta_b),\quad y_f = 0,\quad z_f = f_{re}\cos(\theta_b) \tag{9}$$

From the phase center of the feed, the center of the microstrip arrays on the reflectarray's surface is obtained such that the incident angle of the feed horn θ_f, relative to the normal of the reflectarray's surface is very close to the main beam scan angle θ_b. By choosing the value of θ_f very close to θ_b, the effect of beam squint with frequency can be minimized to a great extent for an offset feed system.

Since the center of the microstrip arrays on the reflectarray's surface lies on the surface formed by the parabolic reflector, the subtended angle θ_0 can be determined with its corresponding focal length defined as

$$F = \frac{r_F(1+\cos(\theta_0))}{2} \tag{10}$$

Now the origin in the (x, y, z) coordinate system is redefined such that the phase center (x_f, y_f, z_f) of the feed is placed at $(0, 0, F)$ and the (x_{re}, y_{re}, z_{re}) coordinates of the microstrip reflectarray elements are also transformed accordingly. The surface of a parabolic reflector is formed simply by expressing the value of z_{sh} coordinate in terms of x_{re} and y_{re}. That is,

$$z_{sh} = \frac{x_{re}^{\,2} + y_{re}^{\,2}}{4F} \tag{11}$$

Finally, the path difference is given by

$$\Delta l = \sqrt{x_{re}{}^2 + y_{re}{}^2 + (z_{re} - F)^2} - \sqrt{x_{re}{}^2 + y_{re}{}^2 + (z_{sh} - F)^2} + z_{sh} - z_{re} \tag{12}$$

2.4 Phase of reflected field from element

In this work, the phase of the reflected field from an element is computed using HFSS^{TM} 3D Full-wave Electromagnetic Field Simulation software[16]. As shown in Fig. 4.(a), the phase of the reflected field from a single unit cell can be calculated using suitable boundary conditions: two E-walls and two H-walls, that is, perfect electric conductor and perfect magnetic conductor respectively. According to image theory, the excited current on an element will be duplicated to four-way like Fig. 4.(b), so this configuration is equivalent to an infinite array with identical elements.

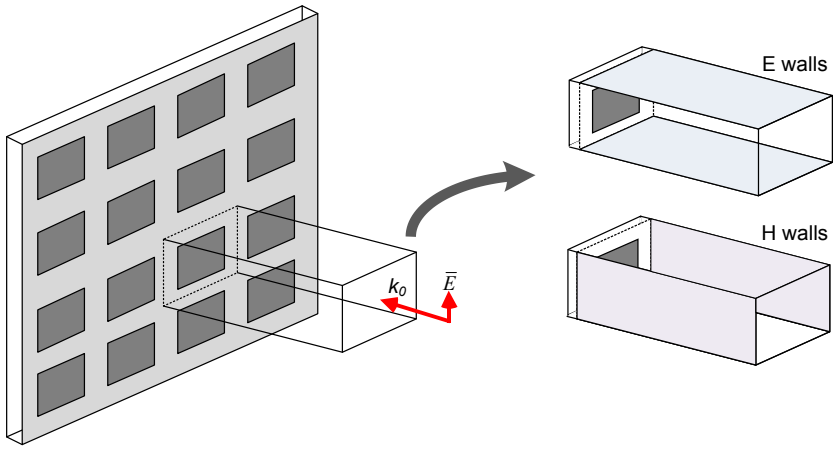

(a)

Fig. 4. Simulation setup for a unit cell in a waveguide with (a) boundary conditions equivalent to an infinite array and (b) duplicated currents from these boundaries

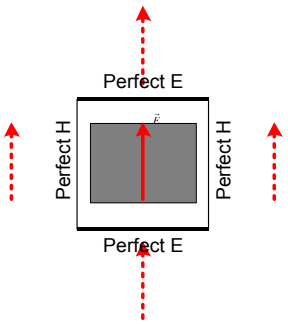

(b)

Fig. 4. continued.

The reflection coefficient resulted from the simulation using HFSS is

$$\Gamma = \frac{\bar{E}_{inc}}{\bar{E}_{refl}} \tag{13}$$

By setting the phase of the incident wave as reference, that is, $\bar{E}_{inc} = E_{0,i}$ and $\bar{E}_{refl} = E_{0,r} \cdot e^{j\varphi}$, the above equation becomes as [17]

$$\Gamma = \frac{E_{0,i}}{E_{0,r}} \cdot e^{j\varphi} = |\Gamma| \cdot e^{j\varphi} \tag{14}$$

The required phase in Eq. (7) can be obtained from the simulation results, even though the simulation was conducted for a normal incident field. However, the reflected phase does not differ for incidence angles smaller than 40 degrees [18]. Therefore, the simulation results at normal incidence can be used in reflectarray design.

2.5 Aperture efficiency of reflectarray

In the design of a reflectarray system, the aperture efficiency is one of the most important factors to predict the reflectarray system performance. Similar to the normal

parabolic reflector, the design of the reflectarray system usually begins with a specified gain. The gain of a reflectarray antenna can be obtained by the product of the aperture directivity and the aperture efficiency. The aperture directivity D_r is determined by the aperture area A as

$$D_r = \frac{4\pi A}{\lambda^2} \tag{15}$$

then, the gain of the reflectarray antenna is defined as

$$G = D_r \cdot \eta_a = \frac{4\pi A}{\lambda^2}\eta_a \tag{16}$$

If the aperture efficiency does not include the efficiency factors related with the feed loss, reflectarray element loss, polarization loss, and mismatch loss, the aperture loss is determined by two dominant efficiency terms in the reflectarray design: the spillover efficiency (η_s) and the illumination efficiency (η_i). So, the aperture efficiency can be defined as

$$\eta_a = \eta_s \eta_i \tag{17}$$

To calculate the efficiencies of the reflectarray, the radiation properties of the feed antenna should be modeled. Among various radiation models, $cos^q\ \theta$ pattern is used in this study due to its simplicity.

$$U_f = \cos^q \theta \left(0 \le \theta \le \frac{\pi}{2}\right) \tag{18}$$

The parameter q determines the pattern shape and the directivity of the feed antenna. Fig. 5 shows the directivity of the feed antenna versus the q value. The larger q value, the higher directivity is. Once the feed antenna is designed with a specific directivity, the

q value is obtained. To verify the cos^q pattern, Fig. 6 shows the real antenna pattern with 10 dBi of directivity and the cos^q pattern with 2 of q value. As seen from the graph, two patterns are matched well with each other.

The spillover is defined as the ratio of the power intercepted by the reflecting elements to the total power, which is usually considered in transmit mode. Fig. 7 shows the reflectarray configuration for spillover efficiency, which is the percentage of the radiated power from the feed that is intercepted by the reflecting aperture [19].

$$\eta_s = \frac{\int_\sigma \int \vec{P}(\vec{r})\vec{s}}{\int_{total} \int \vec{P}(\vec{r})\vec{s}} \tag{19}$$

where the denominator is the total power radiated by the feed, and the numerator is the portion σ of the power incident on the array aperture.

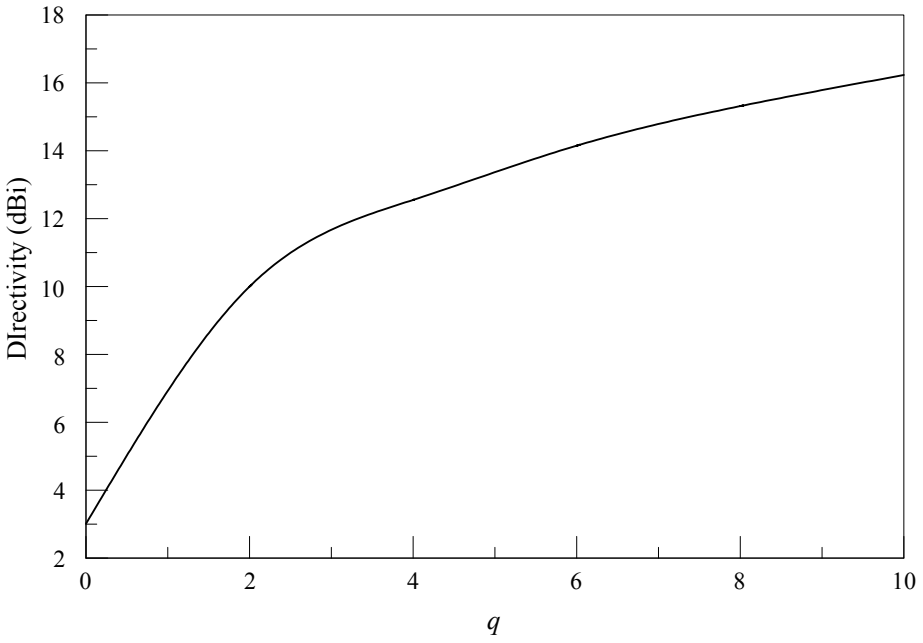

Fig. 5. Directivity vs. q factor of the feed

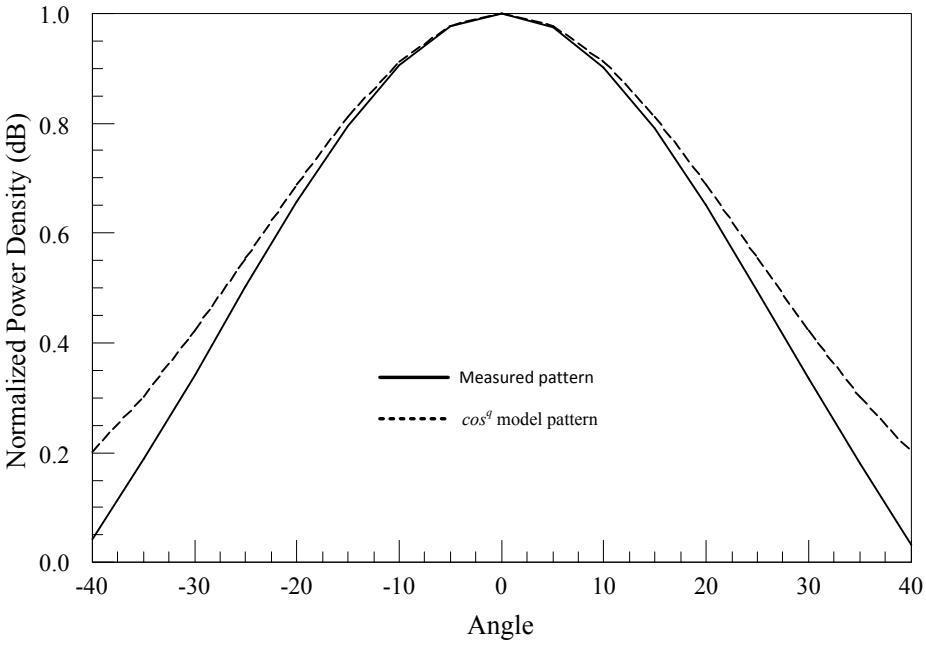

Fig. 6. The real antenna pattern vs. cos^q pattern

The spillover efficiency in equation (19) can be expressed in terms of the design parameters of the reflectarray system [19] as

$$\eta_s = \frac{2q+1}{2\pi} \int_0^{2\pi} \int_0^{D/2} \frac{H}{r^3} \left(\frac{r_0^2 + r^2 - s^2}{2 r_0 r} \right)^{2q} \rho d\rho \varphi \tag{20}$$

Thus, η_s is a function of six design parameters [19]:

$$\eta_s = \eta_s(D, \theta_0, H, q, x_0, y_0) \tag{21}$$

From the result, the spillover efficiency is free from the reflectarray element pattern among all the configuration parameters.

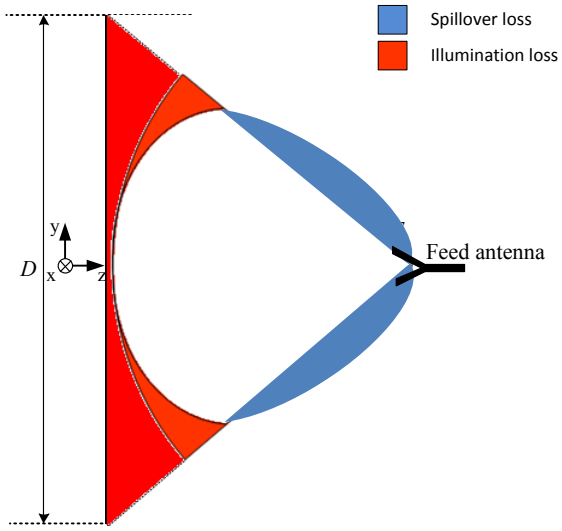

Fig. 7. Reflectarray configuration for spillover efficiency

The illumination efficiency is efficiency loss due to non-uniform amplitude and phase illumination of the aperture plane.

$$\eta_i = \frac{1}{A_a} \frac{\left| \iint_A I(x,y) dA \right|^2}{\iint_A |I(x,y)|^2 dA} \tag{22}$$

where *I(x, y)* is the amplitude distribution over the aperture. This can be also calculated [19] as

$$\eta_i = \frac{4}{\pi D^2} \frac{\left[\int_0^{2\pi} \int_0^{D/2} \frac{1}{r^1 + q_e} \left(\frac{r_0^2 + r^2 - s^2}{2 r_0 r} \right)^q \rho d\rho d\varphi \right]^2}{\int_0^{2\pi} \int_0^{D/2} \frac{1}{r^1 + q_e} \left(\frac{r_0^2 + r^2 - s^2}{2 r_0 r} \right)^q \rho d\rho d\varphi} \tag{23}$$

which means that η_i is a function of seven parameters:

$$\eta_i = \eta_i(D, \theta_0, F, q, x_0, y_0, q_e) \tag{24}$$

The aperture efficiency of the reflectarray can be calculated once the spillover efficiency and illumination efficiency are determined.

$$\eta_a = \eta_i \eta_s(D, \theta_0, F, q, x_0, y_0, q_e) \tag{25}$$

In the design of a reflectarray, it is desired to find the maximum aperture efficiency with the given design parameters. Especially, the feed location is an important parameter in a practical design. The feed location is described by the offset angle θ_0 and the height F.

CHAPTER III

MICROSTRIP REFLECTARRAYS USING LARGE PHASE CONTROLLABLE ELEMENT*

3.1 Introduction

Recently, reflectarray antennas have been studied to replace the conventional high gain parabolic reflectors because of their low profile structures and light weight. A microstrip reflectarray consists of many microstrip radiating elements which are designed to reradiate the incident field with proper phases [20]. The phase range is required up to 360° to compensate the spatial phase delay between the parabolic curvature and each radiating element location on the flat reflectarray. Due to the less metallization as compared to patches, microstrip rings are commonly used as reflectarray unit cells. The use of the ring element has several advantages such as compact size, broader circular polarization bandwidth, and little blockage of the incident field in multi-layer structures [21]. The reflectarray's phase correction for rings can be achieved by changing ring sizes [22] or rotating elements for circular polarization (CP) [21, 23], but the phase variation ranges are normally limited to less than 360°. To achieve the larger phase ranges, multi-layer stacking techniques have been used [24, 25], which result in design and fabrication complexity.

---

* Parts of this chapter are reprinted with permission from S.W. Oh, C.H. Ahn and K. Chang, "Reflectarray element using variable ring with slot on ground plane," *Electronics Letters*, vol. 45, pp.1206-1207, Nov. 2009, Copyright 2009 by IET.

The primary goal of the design for reflectarrays is to develop elements having wide phase variation range to achieve high gain performance. Different elements having a wide phase variation range are introduced and discussed. Some different prototype reflectarray are presented.

3.2 Variable microstrip ring and slot element

A. Introduction

In this section, a new design of a unit cell composed of a microstrip ring with a slot ring on the ground plane is proposed. The novel structure is used to overcome the limited phase range for the conventional ring element. The proposed unit cell achieves a smooth phase variation over 680° phase range on a single layer. The additional slot ring structures are only used for 10% of the elements on the reflectarray because using them for 100% of the elements would allow too much fields leakage through slots. The reflectarray is fabricated and measured at K-band.

B. Element design

The reflectarray structures composed of microstrip rings on the top surface and some slot rings on the bottom surface are shown in Fig. 8. The reflectarray are designed and fabricated on a RT/Duroid 5870 substrate with permittivity $\varepsilon_r = 2.3$ and $\tan \delta = 0.0005$ to operate at center frequency of 22 GHz. The phase responses of these structures are simulated using Ansoft HFSS simulation software with periodic boundary conditions. The thickness of the substrate is 0.81 mm.

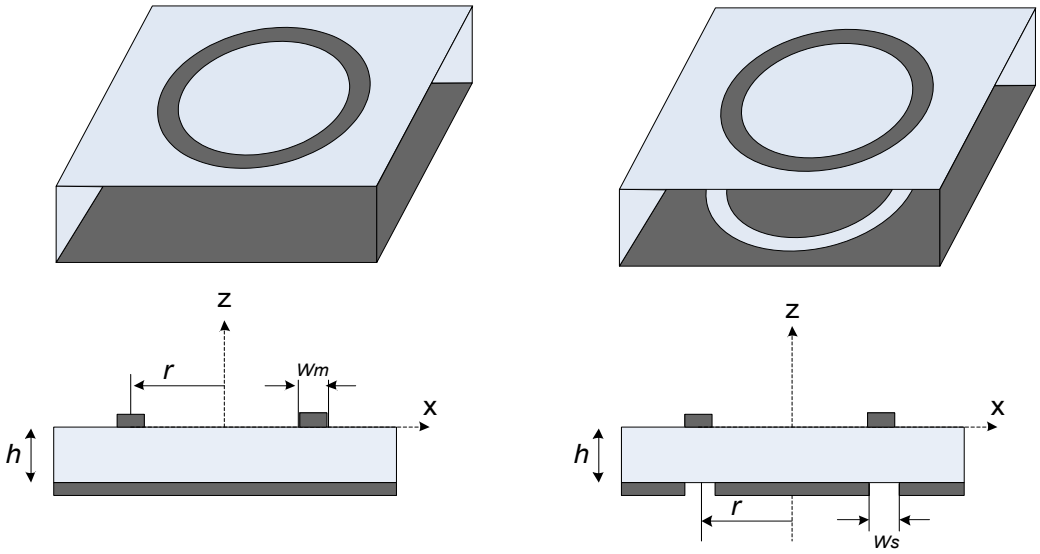

Fig. 8. Microstrip ring and slot element

The slot rings on the ground plane have the same dimensions as the upper microstrip ring. The progressive phase responses of elements are achieved by controlling the radius of rings. In Fig. 8, the width of the microstrip ring, w_m is set to 0.4 mm and the width of the slot ring, w_s is given as 0, 0.3, and 0.5 mm.

The reflection phase responses of the structures for a normal incident wave are shown in Fig. 9. The reflection phase range of a microstrip ring no slot ring with the ground plane (w_s = 0 mm) can reach up to 339°. However, the reflection phase range is substantially increased more and the curve is smoother when a slot ring is added on ground plane. Because the slot ring on the ground plane perturbs the electrical field and current paths, the phase range of the unit cell can reach up to 682°.

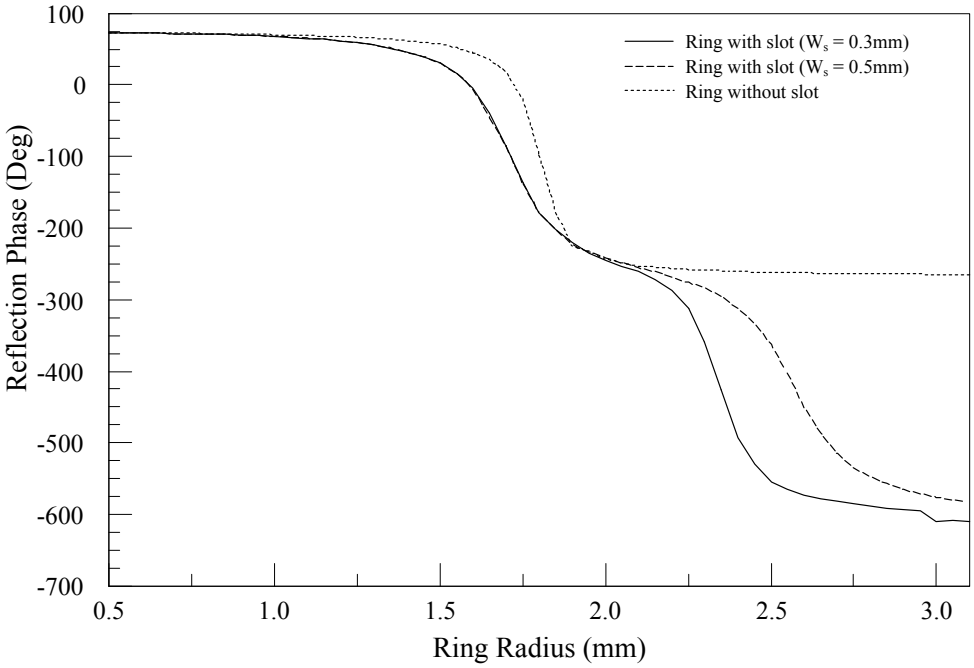

Fig. 9. Phase response as a function of the ring radius

Fig. 10 shows the required phase at each element on the surface of the reflectarray. The required phase was calculated by Matlab software according to each element location, feed location, and the main beam direction. Fig. 11 and Fig. 12 show the mask of the reflectarray composed of microstrip rings on top plane and some slot rings on ground plane, and the fabricated prototype reflectarray etched with the mask, respectfully. In Fig. 11, the microstrip rings are shown on the white background (top plane), and the slot rings are shown on the black background (bottom plane). On the top plane, the center to center spacing of elements is set to be 0.5 λ_0 in both x- and y-directions, that is, the unit cell size is 7 mm × 7 mm. There are 1,056 elements printed on a 24 cm × 23 cm size substrate. On the bottom plane, the slot rings are only required to cover 10% of the microstrip rings on the top.

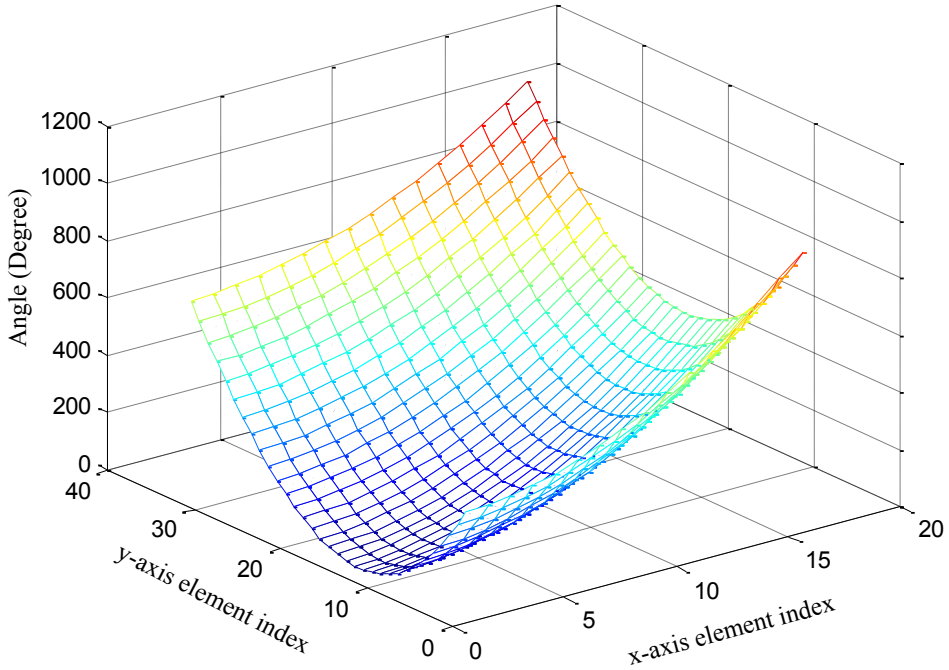

Fig. 10. Required phases calculated in Matlab

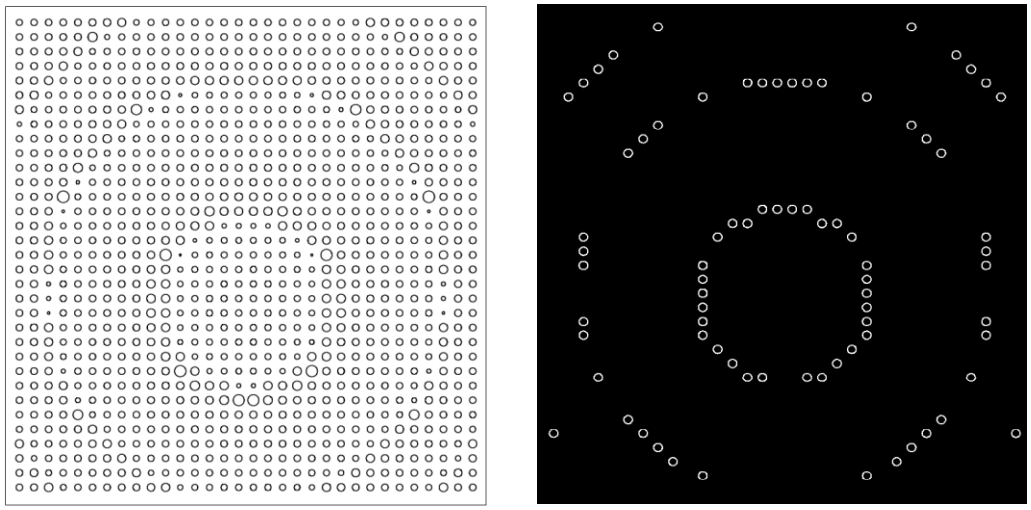

(a) (b)

Fig. 11. Reflectarray layout: (a) top surface, (b) bottom surface

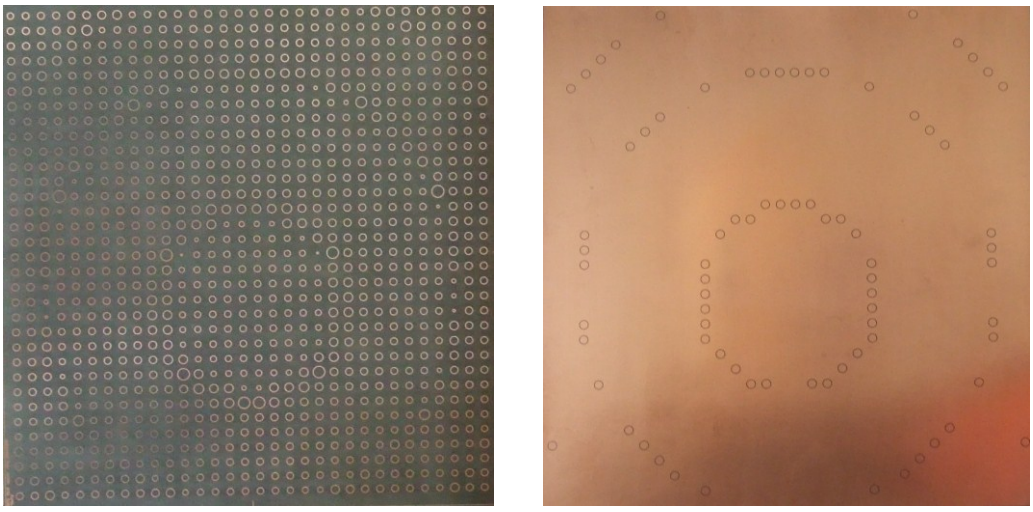

(a) (b)

Fig. 12. Fabricated reflectarray: (a) top surface, (b) bottom surface

C. Measured results

Fig. 13 shows the measurement setup for the prototype reflectarray. The feed horn antenna offset angle is 20° with reference to broadside to avoid the blockage from the horn antenna. An 18-26 GHz feed horn antenna was used as a primary source and it was located at 250 mm from the bottom edge of the reflectarray.

The normalized radiation patterns at 22 GHz for E and H-planes are shown in Fig. 14. The asymmetry of the radiation patterns is due to the metal supporting structure used for the feed and array. A half-power beam width is measured to be 3.4° in the E-plane and the first side lobe level (SLL) is -18.4 dB relative to the main beam. In the H-plane, a half-power beam width is 3.5° and SLL is –21.1 dB. Cross-polarization levels are below -30 dB in both planes. The maximum gain of the reflectarray is 33.4 dBi at 22 GHz. It is 0.3 dB higher than that of the reflectarray using only microstrip rings on the substrate.

Because of leaky waves generated from slots, the back scattering level of the reflectarray is 4 dB higher than the conventional reflectarray, but it still remains below -30 dB.

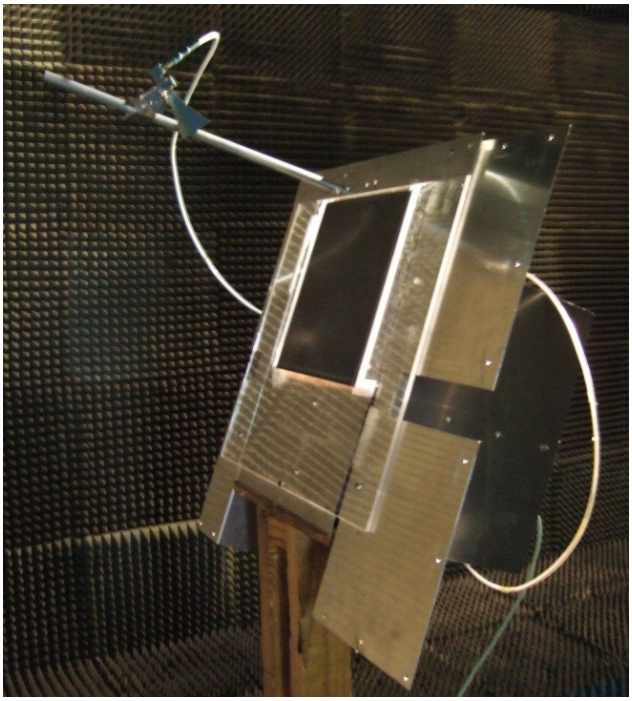

Fig. 13. Measurement setup

D. Conclusions

A novel unit cell based on a microstrip ring with a slot ring on ground plane has been presented. The phase response range of the unit cell is greater than 682° with a smooth phase variation. This is accomplished by adding slot rings on part of the ground plane. A reflectarray of 1,056 elements is designed and measured at 22 GHz to demonstrate this concept. The maximum gain and half-power beam width is 33.4 dBi and 3.4°, respectively, and this array gives better performance than the conventional reflectarray.

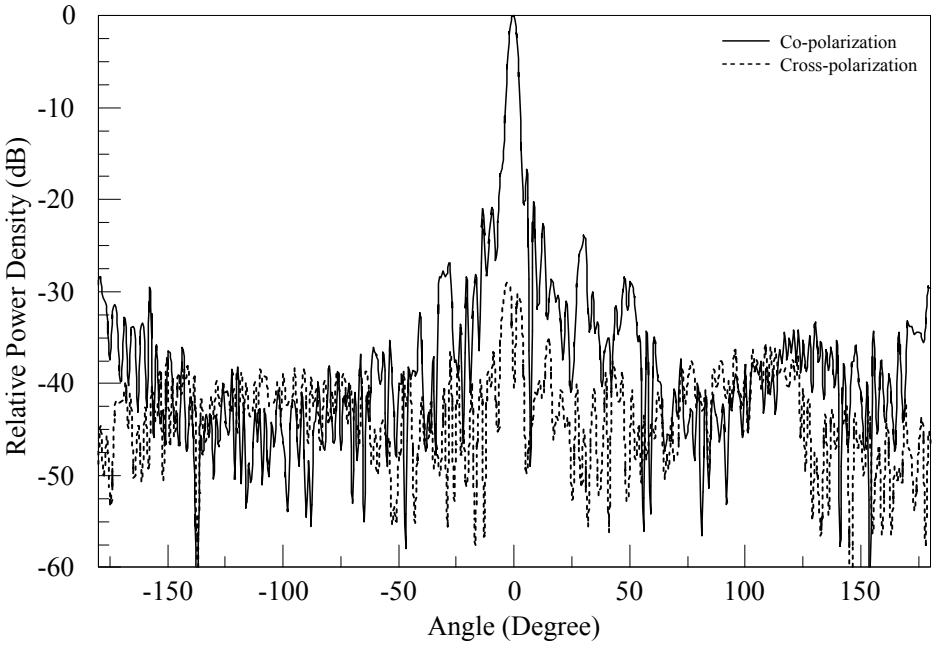

(a)

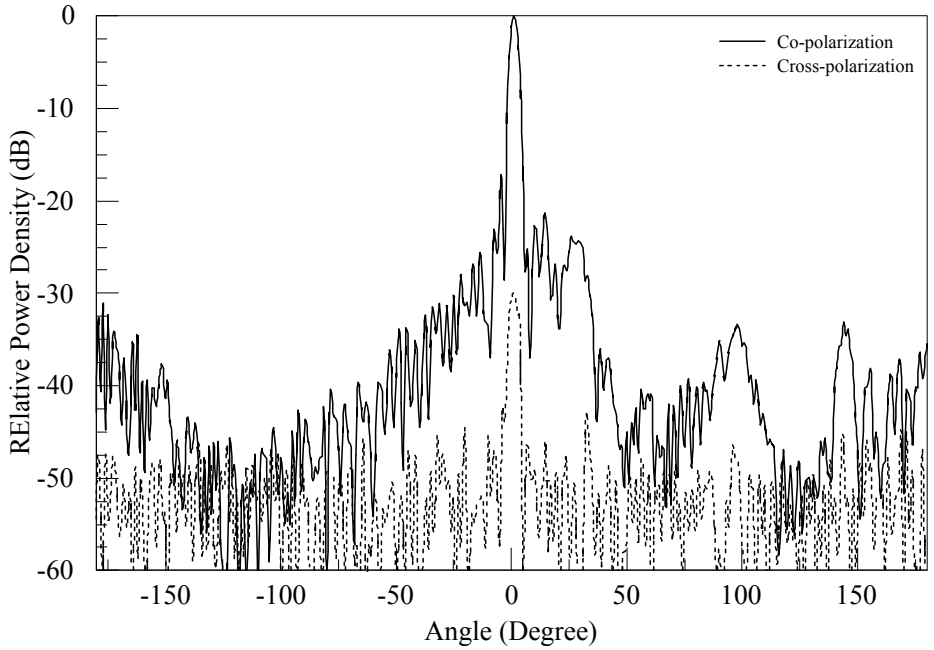

(b)

Fig. 14. Measured radiation pattern: (a) H plane (b) E plane

3.3 Modified microstrip ring and slot element

A. Introduction

In Section 3.2, a circular slot added on a ground plane increased the phase range of an element. However, since the phase variation of the element is not smooth the 3dB gain bandwidth was limited to 7.4 %.

In this section, an improved ring-plus-slot element is proposed for improving the phase slop as well as its range. The proposed element consists of a microstrip ring placed on top of a circular slot and an additional layer with a ground plane. A ground plane is added under the slot to increase the interaction between the slot and the ground plane, producing a smooth phase variation. A ground plane also eliminates undesirable relations with the surface material where a reflectarray will be installed, and prevents energy leakage through the slots.

A progressive phase shift can be achieved by varying the radii of both the ring and the slot. The linearity of the phase variation is also improved. The effects of the available several design parameters of the proposed unit cell are discussed below, and the results of a prototype reflectarray working at 20 GHz are presented.

B. Element design and characteristics

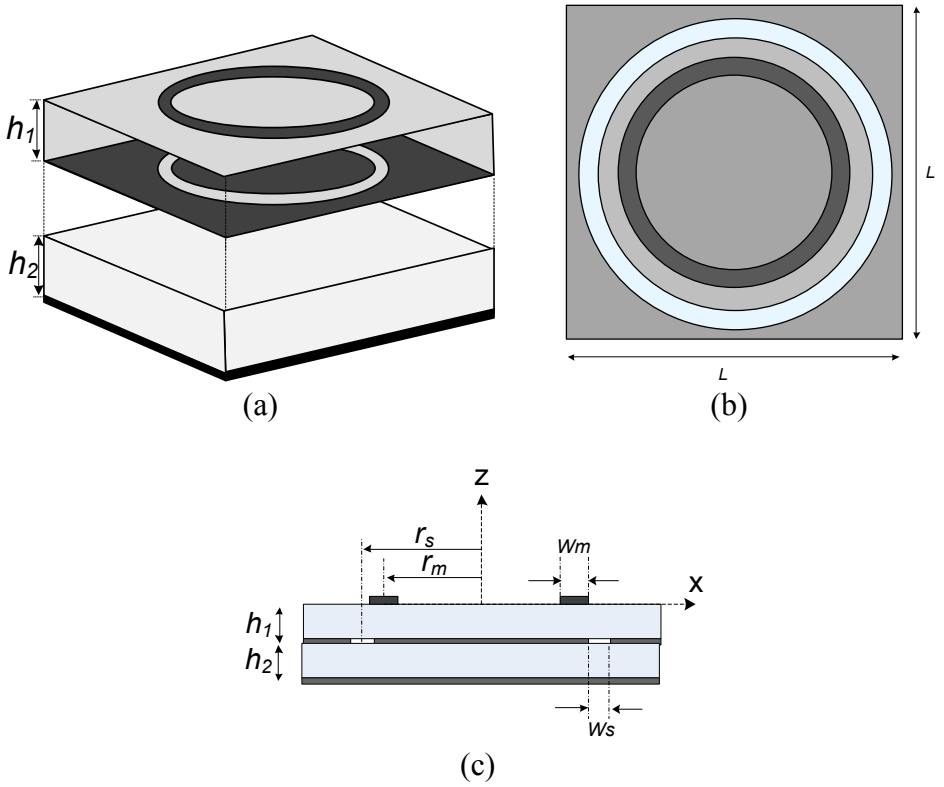

Fig. 15. Modified reflectarray unit cell using a ring and a slot on the ground plane: (a) perspective view, (b) top view and (c) side view

The configuration of the proposed reflectarray element is shown in Fig. 15. A microstrip ring is printed on the top conducting surface of a substrate of height h_1, and a circular slot is etched on the bottom surface of the substrate. A ground plane is placed on the bottom of another substrate with a height h_2. The unit cell is a square lattice with a side length (L) of 7mm, which is 0.47 λ_0 at 20 GHz, in both the x- and y- directions. The reflected phase of the unit cell has been calculated using Ansoft IS HFSS finite-element analysis software [16]. For this phase calculation, the cell was excited by a normal incident plane wave with a linearly polarized electric field. The equivalent unit cell

waveguide approach has been used to simulate a unit cell in an infinite periodic array, and taking into account all interactions with neighboring elements [26]. The substrate of the proposed element is Roger/Duroid 5880, with a relative permittivity $\varepsilon_r = 2.2$ and loss tangent $\tan \delta = 0.0004$ [27]. Fig. 16 shows the performance of the ring-plus-slot element. Three types of combinations are shown: a variable ring without a slot (i.e., $w_s = 0$); a variable ring with a fixed slot; and a variable ring with a variable slot. All three combinations have a substrate thickness $h_1 = 0.7874$ mm, a microstrip ring width $w_m = 0.4$ mm, and a slot ring width $w_s = 0.4$ mm. It can be concluded from Fig. 2 that a variable slot produces the most desirable the reflected phase. The variable ring without a slot and the three fixed slots provide an overall phase variation of less than 360°. The fixed slots just change and shift the phase range slightly. On the other hand, a variable ring with a variable slot achieves over 650° of phase variation. In the cases of a fixed slot, a microstrip ring just interacts with one of an outer copper and an inner circular patch in a slot, because the size of a ring and a slot are too different. However, in the case of a variable slot, a microstrip ring coupled with an inner circular patch, an outer copper and a ground plane, and the inner patch also interact with the ground plane; therefore, these additional coupling make wide and linear phase response.

The effect of the substrate thickness h_1 is shown in Fig. 17. The thinner substrates provide larger phase variation ranges, but their phase responses are less linear than the ones of the thicker substrates. The h_1 value can be adjusted for optimum trade-off between the phase range and linearity. A substrate thickness of 0.7874 mm has been

chosen for our prototype because it gives a better phase range and linear characteristics for the proposed element.

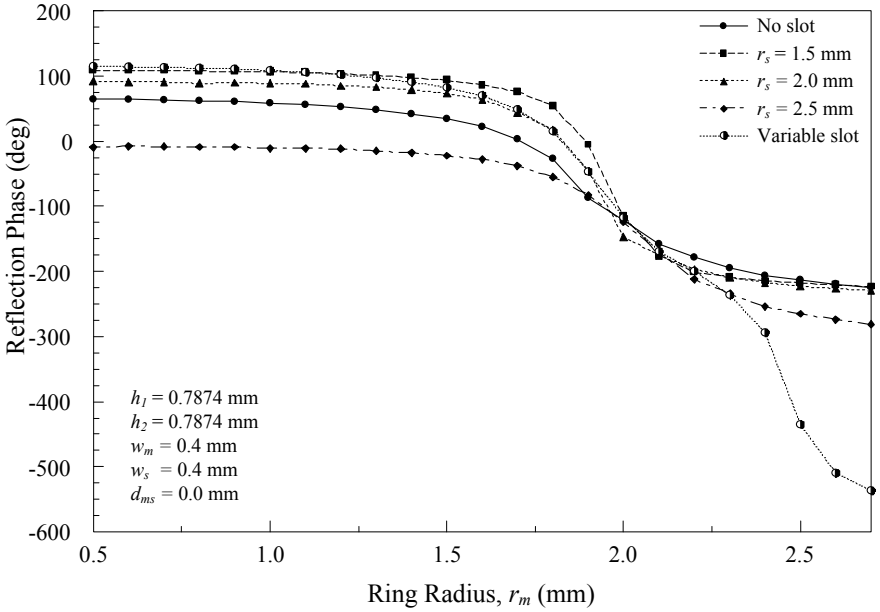

Fig. 16. Phase response as a function of the slot radius (r_s)

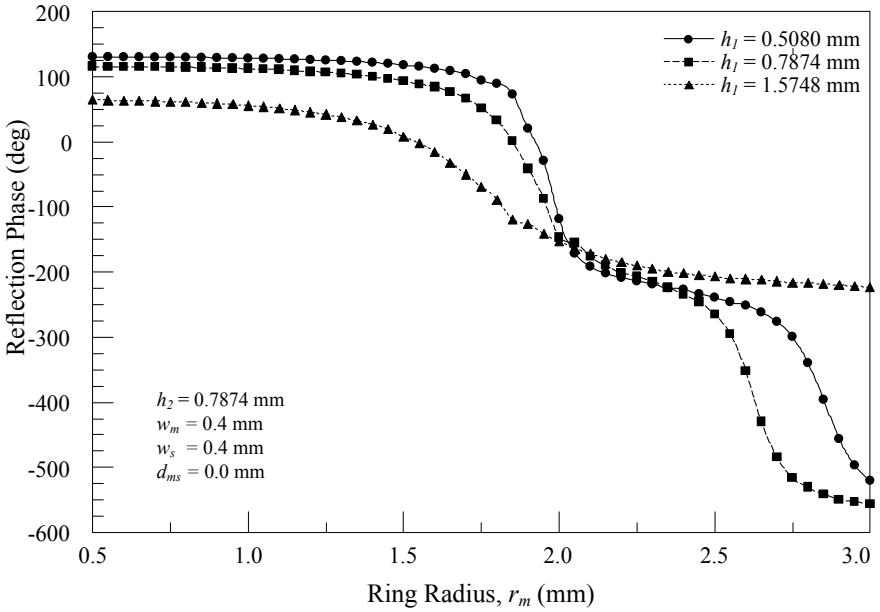

Fig. 17. Phase response as a function of the substrate thickness (h_1)

Fig. 18 and Fig. 19 show the effect of the microstrip ring width w_m and the slot width w_s, respectively, on the reflected phase. Smaller ring and slot widths produce a larger phase variation range, but also yield a steeper slope. Considering these responses, the ring and slot width of our prototype were chosen as 0.4 mm and 0.5 mm, respectively. Fig. 20 shows the effect of the difference d_{ms} between the ring and the slot radii. As shown in this figure, this difference impacts primarily the linearity of the phase. A slot radius that is 0.2 mm smaller than the ring radius gives a reasonable linear slope. Varying d_{ms} changes the inductance (the ring and the patch), and the capacitance (among the ring, the patch, the outer copper, and the ground plane), creating a smoother phase response [28]. In conclusion, the proposed unit cell structure with (h1 = h2 = 0.7874 mm, wm = 0.4 mm, ws = 0.5 mm, and dms = 0.2 mm) selected from the just discussed parametric studies, achieved an improved phase range of 707° with better linear characteristics than those discussed in Section 3.2.

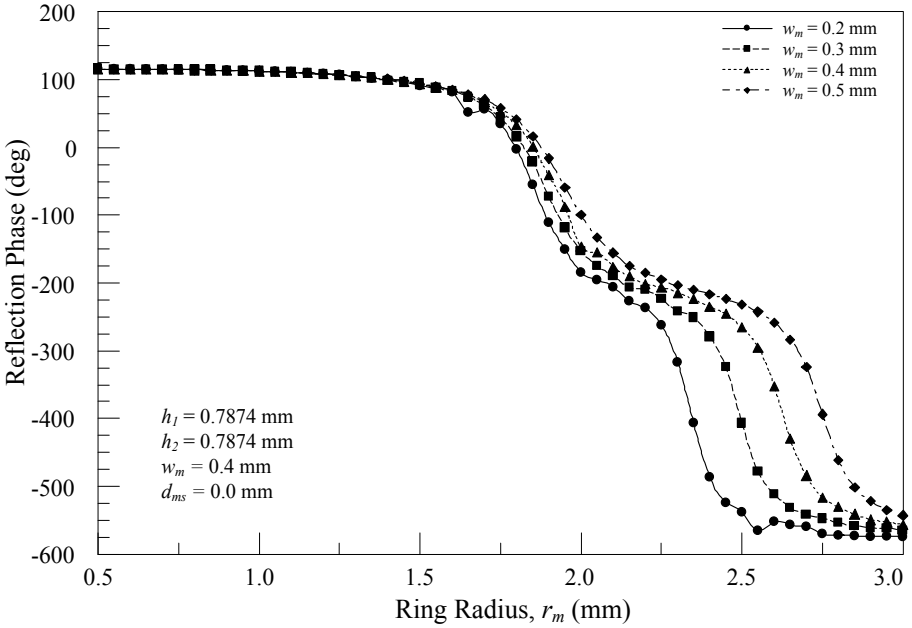

Fig. 18. Phase response as a function of the ring width (w_m)

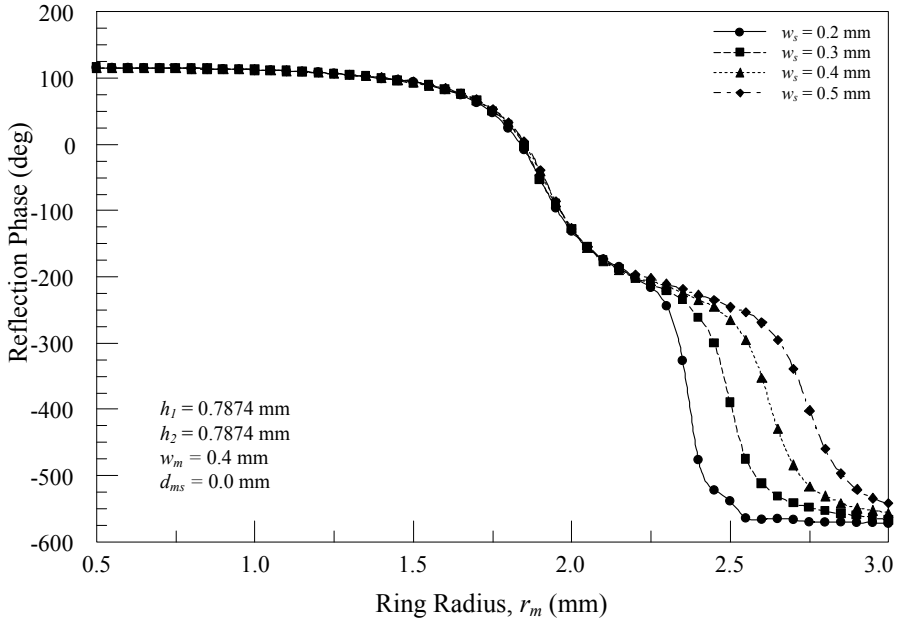

Fig. 19. Phase response as a function of the slot width (w_s)

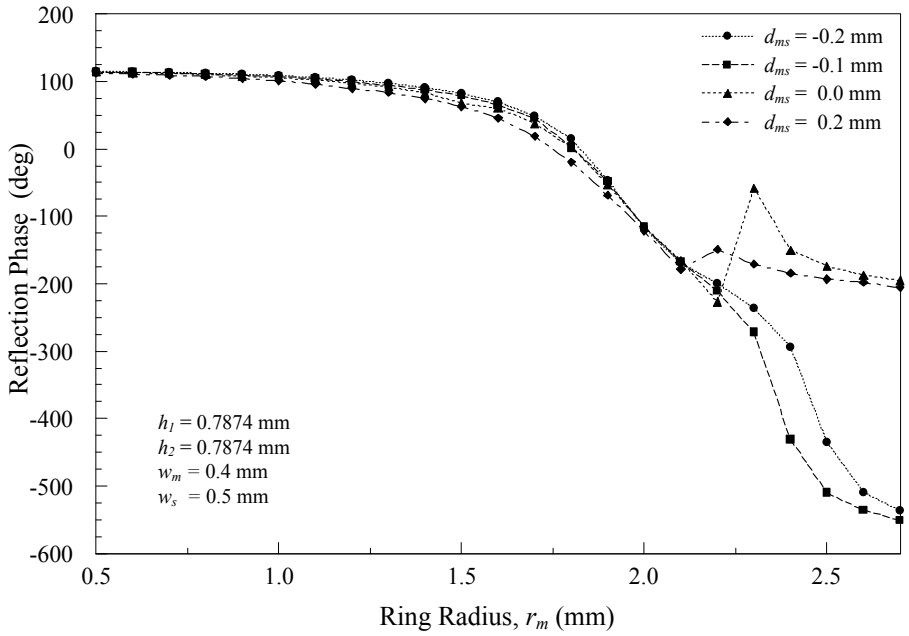

Fig. 20. Phase response as a function of the radius (d_{ms}), $d_{ms} = d_m - d_s$

C. Array realization and measurement

In order to verify the performance of a reflectarray using the proposed rings and slots on a ground plane, a prototype was fabricated and measured at the center frequency of 20 GHz. Fig. 21 and Fig. 22 shows required phase distribution on the surface of the prototype reflectarray and the fabricated reflectarray, respectively. The reflectarray is fabricated on a 22 × 24 cm^2 ($R_h \times R_v$) substrate, and has 31 × 33 (1,023) ring elements printed on a dielectric top surface, and etched on a dielectric bottom surface. Fig. 23 illustrate that the offset angle θ, between the feed horn boresight and the normal direction to the array surface was set to 20° to avoid field blockage due to the feed horn antenna. The f/D ratio of the parent parabolic reflector was set to 1. Therefore, the diameter D and the focal length f of the parabolic reflector are 226 and 235 mm,

respectively. According to the parent reflector configuration, the feed horn antenna was located at a distance of R_f = 250 mm from the array lower edge. The gain of this prototype reflectarray was measured by comparison with a standard gain horn antenna. Fig. 24 shows the measurement setup for the prototype reflectarray.

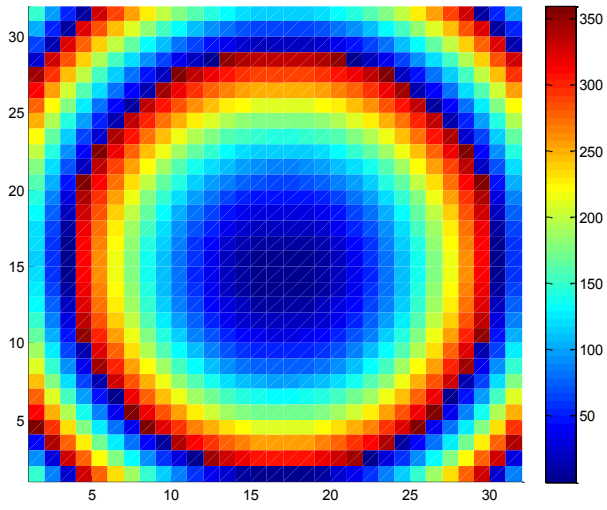

Fig. 21. Phase distribution on the reflectarray

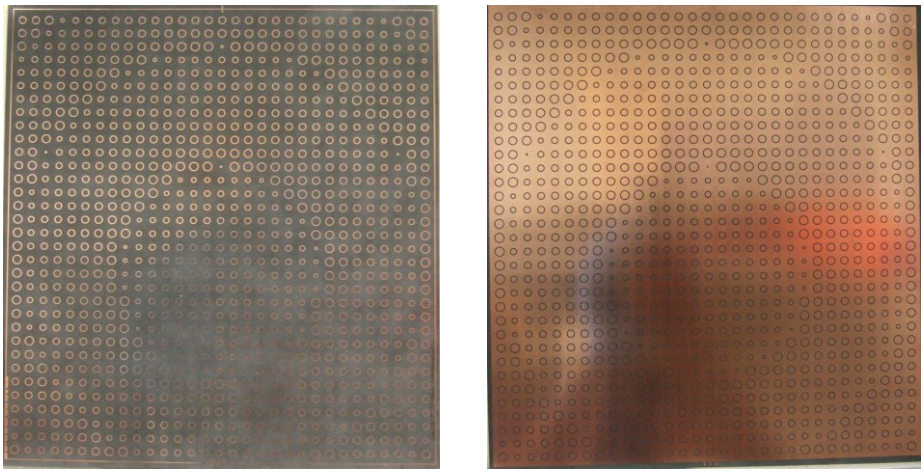

(a) (b)

Fig. 22. Fabricated reflectarray: (a) top substrate, (b) bottom substrate

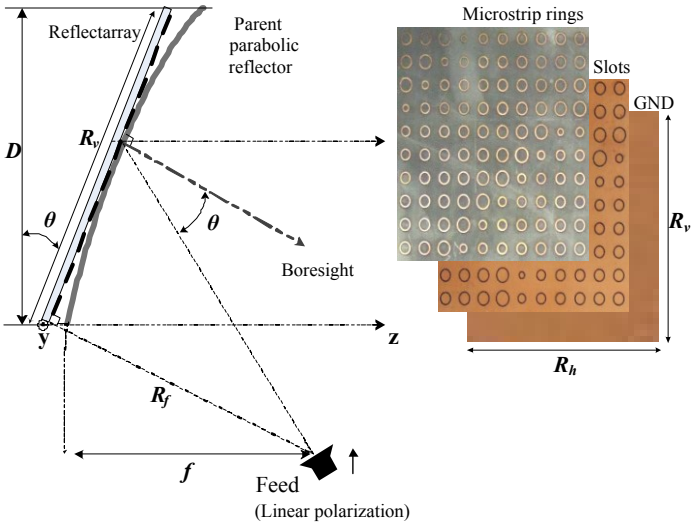

Fig. 23. Overall reflectarray antenna geometry

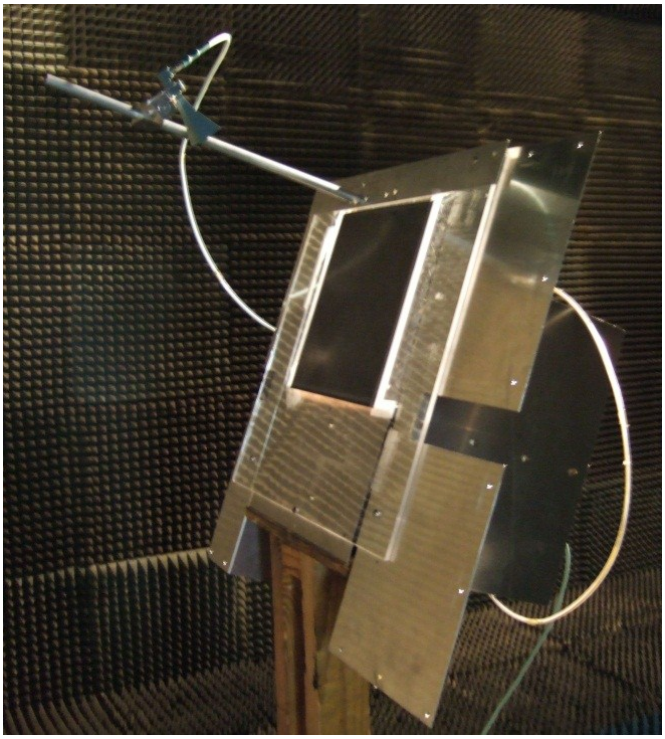

Fig. 24. Measurement setup

Fig. 25 shows the E- and H-plane co- and cross-polarized normalized radiation patterns, at 20 GHz. The maximum gain of the reflectarray is 32.5 dBi and its efficiency is 64.2%. The E-plane measured half-power beam width is 4.1°, and the relative first side lobe level (SLL) is –17.1 dB. The H-plane half-power beam width is 4.0°, and the SLL is –18.4 dB. The measured polarization purity in the boresight direction is about 30 dB in both planes. Fig. 26 shows the dependence of the reflectarray gain with frequency. The 3 dB gain bandwidth is 15.6%, which is more than twice the bandwidth obtained in Section 3.2. This improvement comes from the used array cell more than 360° phase range with a smoother phase response. A behavior that is achieved by the multi-coupling mechanism presented in the unit cell.

D. Conclusions

A novel reflectarray unit cell composing of a variable microstrip ring and a circular slot has been presented. Several design parameters were investigated with an eye on improved reflected phase responses. The proposed unit cell has the advantage of yielding a large phase variation range, and an almost linear phase slope. A reflectarray using about 1,000 elements was designed and measured at 20 GHz, to verify the performance of the proposed element. This reflectarray yielded a gain of 32.5 dBi with a broad 3dB gain bandwidth of 15.6%.

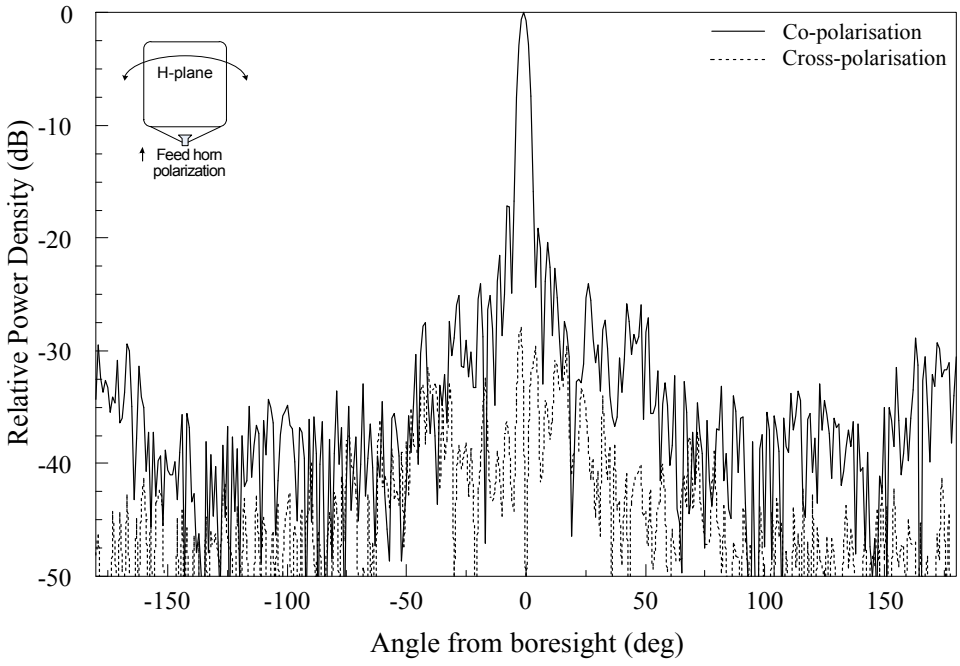

(a)

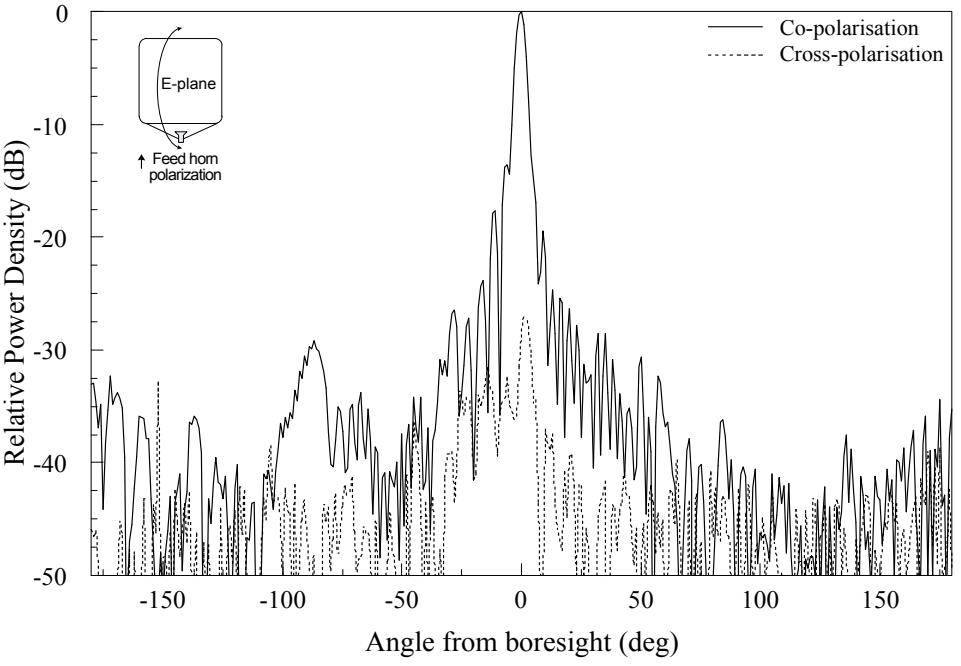

(b)

Fig. 25. Measured radiation patterns (a) E-plane (b) H-plane

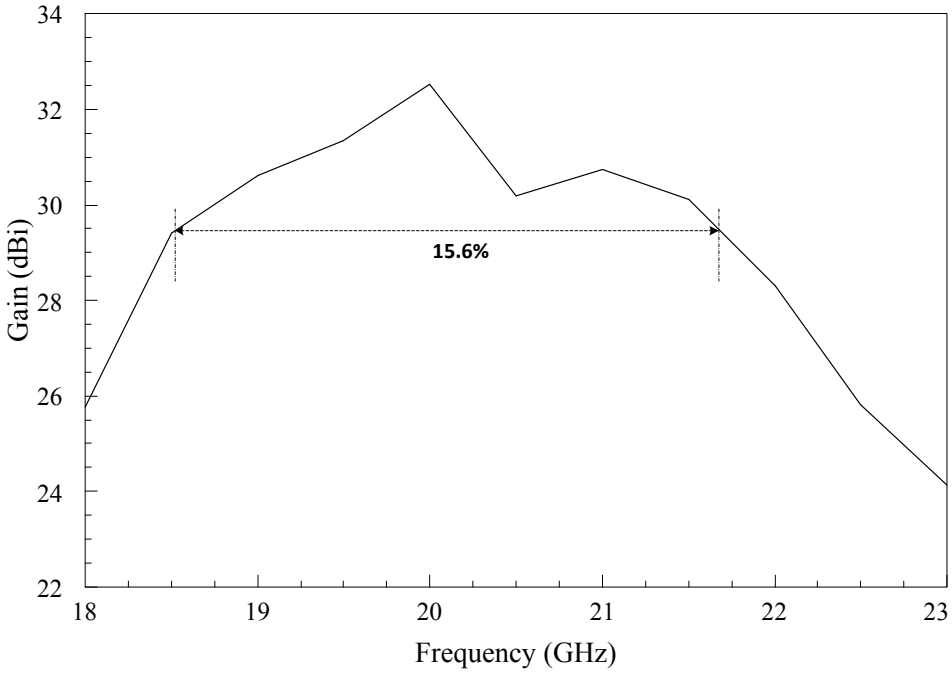

Fig. 26. Measured gain as a function of the frequency

CHAPTER IV

WIDEBAND REFLECTARRAY USING COUPLED ELEMENT WITH SMOOTH PHASE VARIATION

4.1 Introduction

Microstrip reflectarrays have been studied as an alternative to the parabolic reflector due to its advantages such as profile size reduction, large angle tilting ability, and lower manufacturing cost. However, its most critical drawback is a narrow bandwidth performance, compared to the parabolic reflector, caused by two factors: the narrow bandwidth of the radiating elements and the differential spatial phase delay [3]. To overcome the narrow bandwidth of the microstrip reflectarray, array elements with a linear phase response can be used. The linear phase responses can be achieved in several ways using thick substrates, multiple stacked patches [24] and aperture-coupled phase shifters [29]. However, these methods result in fabrication complexity and weight increase, because of their multiple layer structures or their thick substrates.

In this paper, a phi-shape element is proposed as a reflectarray unit cell to improve the linearity of a phase response as well as to increase a phase variation range using a simple structure. The proposed phi-shape element combines two components which are a microstrip split ring and a dipole on a substrate, and this element produces a large phase range more than 418° and a linear phase response with a low slope. A prototype reflectarray using these elements is designed and measured at 20 GHz.

4.2 Element design

The phi-shape element in Fig. 27 is simulated on a RT/Duroid 5880 substrate with permittivity ε_r = 2.2 and tan δ = 0.0004 to operate at center frequency of 20 GHz. The phase responses of this structure are calculated using Ansoft HFSS simulation software with periodic boundary conditions to take into account interactions with neighbor elements. The substrate thickness is 0.79 mm. The unit cell is a 0.47 λ_0 square lattice (a = 7 mm) in both the x- and y- directions, and it is excited by a linearly polarized electric filed in the y-direction.

The phi-shape element combines a uniform size split ring and a variable dipole. A progressive phase shift can be achieved by varying the dipole length d_l with a dipole width d_w of 0.3 mm. The split ring dimensions are set to be an outer radius r = 2.0 mm, a ring width r_w = 0.3 mm, and a split width s_w = 0.6 mm. The radius of the split ring was estimated by [30], and then it was modified by parametric studies through Ansoft HFSS software.

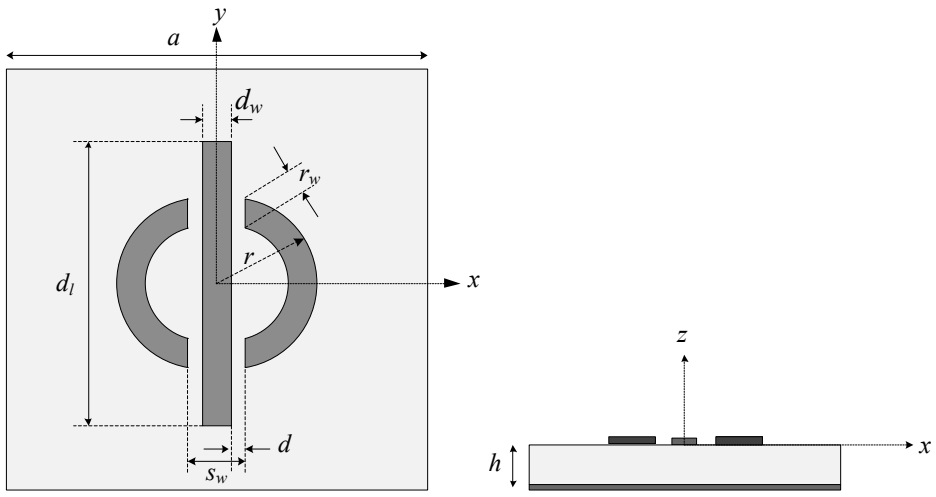

Fig. 27. Geometry of reflectarray elements

Fig. 28 shows the phase shift of the proposed element as a function of a dipole length. The phase response graphs which a variable split ring and a variable dipole can produce are added to compare the linearity of the responses. The phase variation range of 418° and the almost linear phase response with a slow slope are achieved. In the proposed element, the coupling gap *d*, the distance between the split ring and the dipole, affects the linearity of the phase variation curve. A large *d,* results in a smaller linear phase response. Therefore, the *d* is chosen to be the thinnest value of 0.15 mm, which is the accuracy of our etching facility.

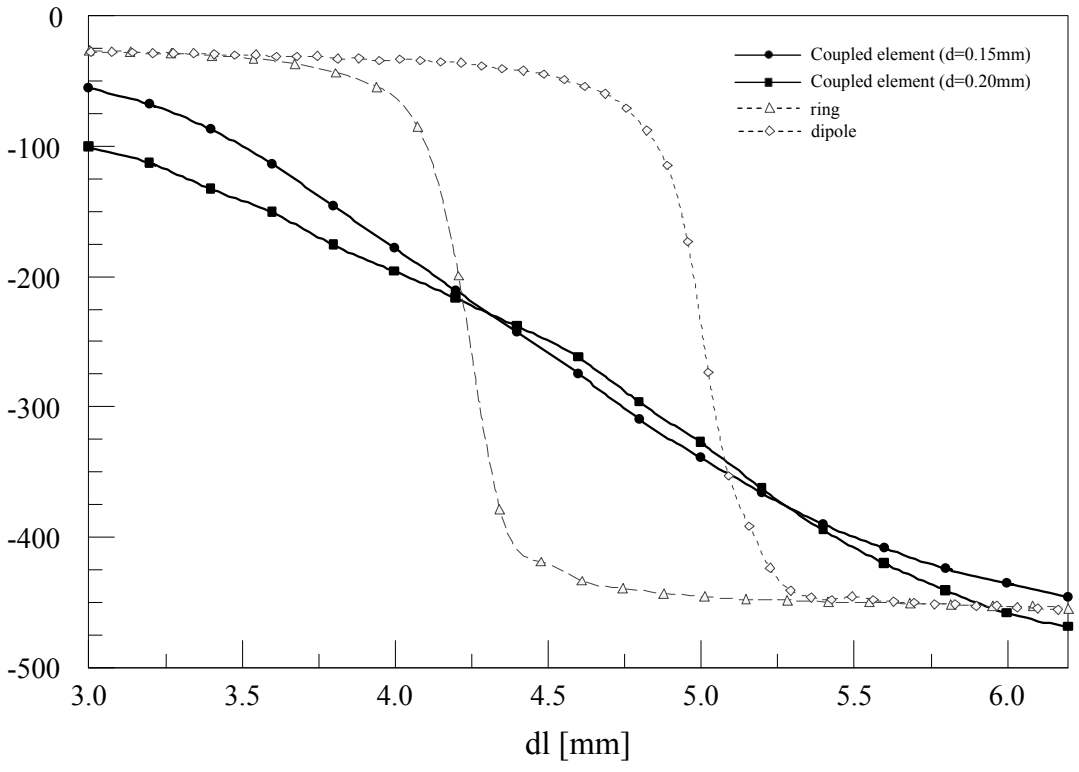

Fig. 28. Phase variation of proposed element

4.3 Array realization and measured results

Fig. 29 and Fig. 30 show the required phase distribution of the reflectarray and the fabricated reflectarray based on the distribution.

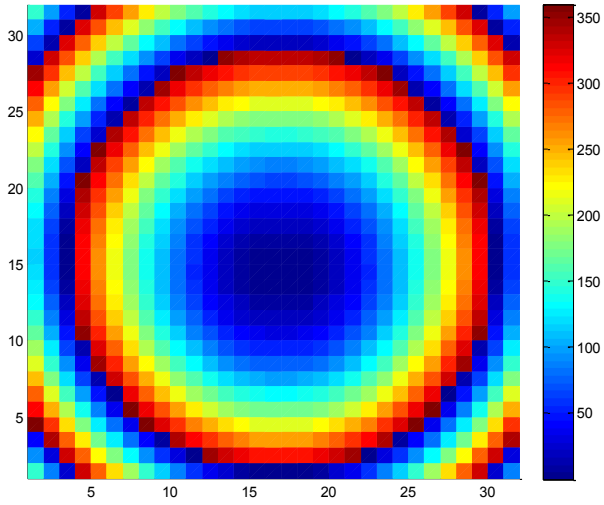

Fig. 29. Phase distribution of the reflectarray

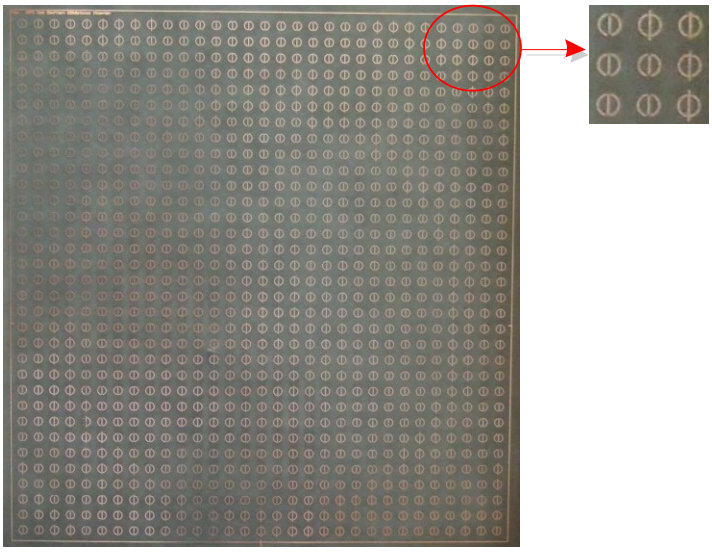

Fig. 30. Fabricated reflectarray using coupled element

Fig. 31 shows the prototype reflectarray configuration using 31 × 33 (1,023) phi-shape elements printed on a 22 × 24 (R_h × R_v) cm^2 size substrate. The offset angle θ between the source antenna and the normal direction of the array is set to be 20° to prevent blockage of the source horn antenna. The source horn antenna is installed at a distance of R_f (250 mm) from the array bottom edge, which results in the *f/D* ratio of 0.96. Fig. 32 shows the normalized radiation patterns at 20 GHz for both E- and H-planes. The maximum measured gain of the reflectarray is 33.0 dBi. The E-plane measured half-power beam width is 3.8° and the first side lobe level is -16.7 dB. The H-plane half-power beam width is 3.7° and the side lobe level is -18.2 dB. The measured cross polarization level in the boresight direction is more than 30 dB in both plane. The asymmetry of the E-plane patterns is due to the metal supporting structures used for the feed and the array. Fig. 33 shows the reflectarray gain against frequencies. A wide 3dB gain bandwidth of 19.0 % is achieved using these simple unit cells on a single layer.

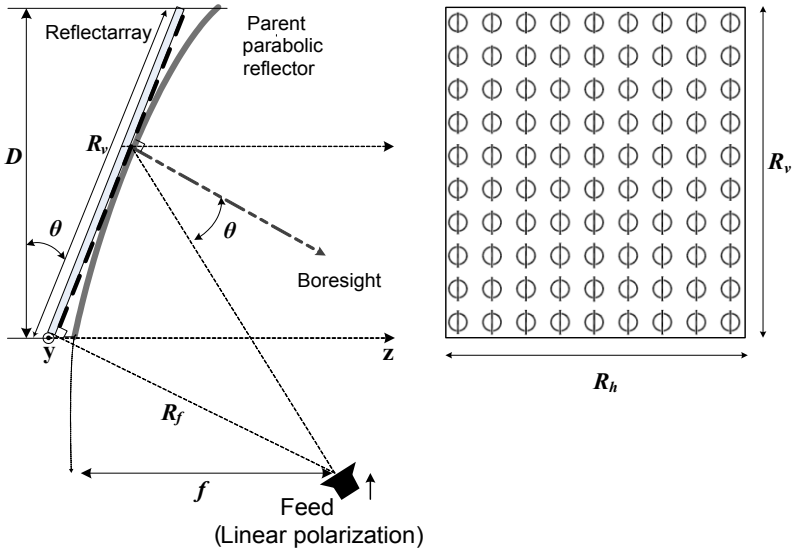

Fig. 31. Prototype reflectarray antenna geometry

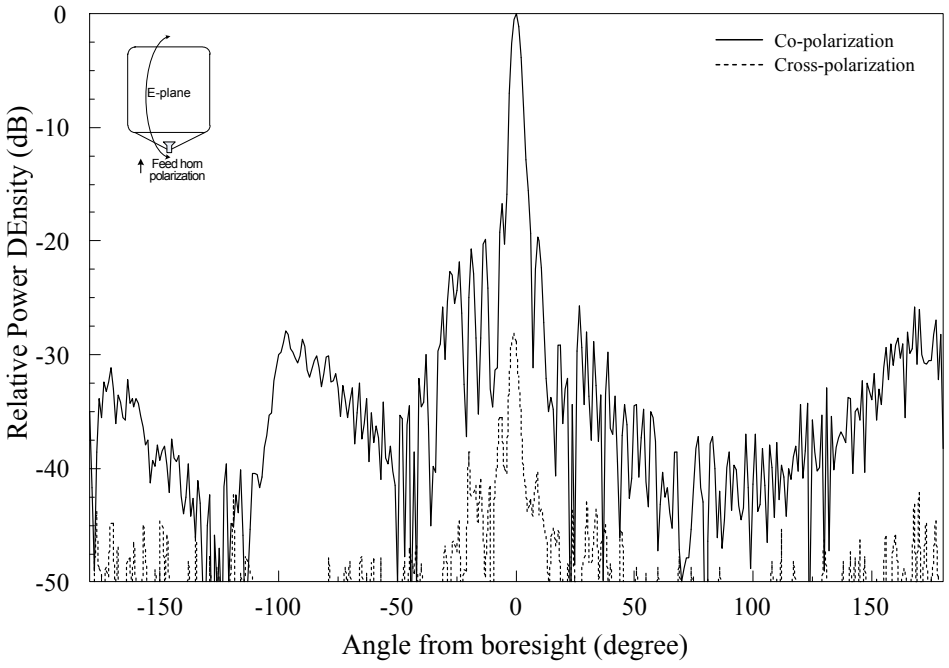

(a)

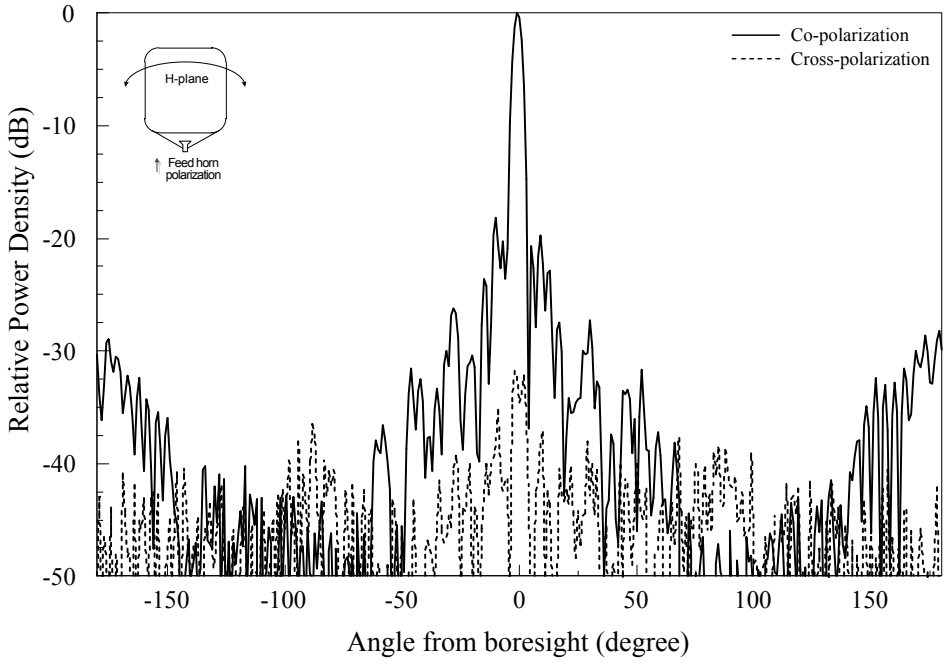

(b)

Fig. 32. Measured radiation patterns: (a) E plane, (b) H plane

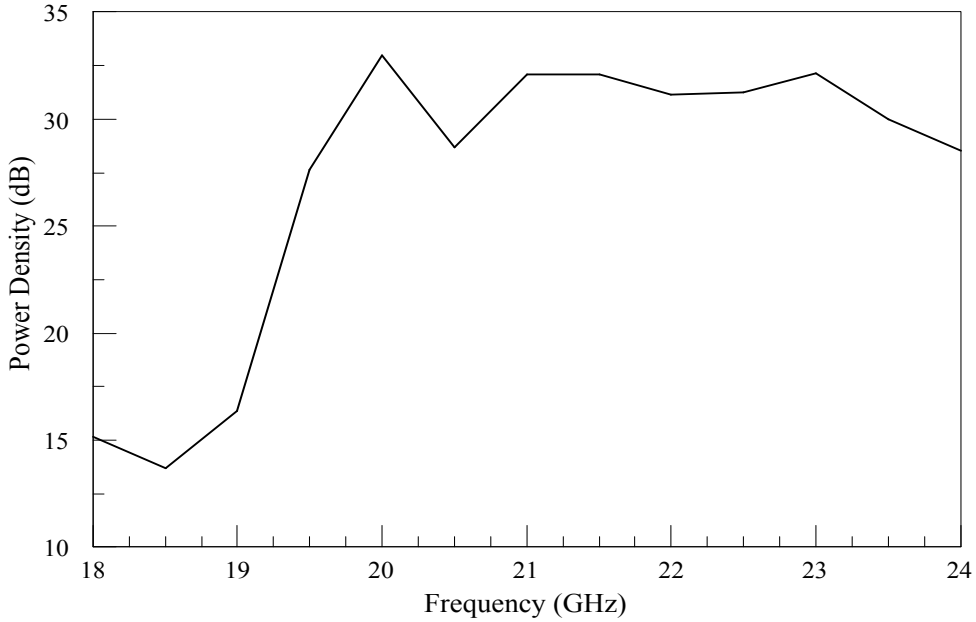

Fig. 33. Measured gain as a function of frequencies

4.4 Conclusions

A novel unit element composed of a resonant split ring and a phase control dipole has been presented for reflectarray applications. The proposed unit element achieves a wide phase variation range with a linear phase response on a thin substrate without using multi-layer structures. A tight coupling between these components yields a linear phase response which is similar to that achieved by the multi-layer stacked elements and aperture-coupled elements. The proposed element shows that different types of elements can be combined to increase the phase variation range or to improve the linearity of the phase response. The prototype reflectarray was fabricated and demonstrated with good results, such as a high gain of 33.0 dBi and a wide 3 dB gain bandwidth of 19.0 %.

CHAPTER V

WIDEBAND REFLECTARRAY USING OPTIMIZATION

5.1 Introduction

The main limitation of reflectarrays is the narrow bandwidth due to two factors, the narrow bandwidth of the radiating elements and the differential spatial phase delay [3]. The differential spatial phase delay is due to the different lengths from the feed to each point on the front of the radiated wave. The differential phase delay is exactly compensated at the center frequency. To overcome the bandwidth limitation from the second factor, several methods using optimization routines to adjust all elements in the array to compensate for the frequency dispersion were introduced in [8, 9].

In this chapter, Particle Swarm Optimization (PSO) is proposed to overcome the bandwidth limitation in reflectarrays due to the differential spatial phase delay. The phase delay of each element is compensated locally at different frequencies, by using PSO routine.

5.2 Basic theory of Particle Swarm Optimization

Particle Swarm Optimization (PSO) is an evolutionary computation method originally formulated by Eberhart and Kennedy in 1995 [31]. PSO as developed by the authors comprises a very simple concept, and can be implemented in a few line of computer code [31]. However, PSO has attracted a lot of attention from a variety of

engineering community, because it shows better performance than the popular Genetic Algorithm optimization method [32, 33].

PSO is based on the observation that a swarm of insects, a flock of birds, a school of fish, or a herd of four legged animals behaves in a distinctive manner when searching for food, protection, or something else [34]. When a group tries to find a desirable path to reach a specific destination, members in the group choose the proper path based on their individual experience, and the members are also learning from neighbors' decision. Hence the members in the group can reach their destination faster. The mathematical model for the above mentioned behavior of the swarm is being used in the optimization technique as the Particle Swarm Optimization Algorithm (PSO) [35]. The concept of PSO is well described using the vector representation in [35], and this will be explained in more detail in Fig. 34.

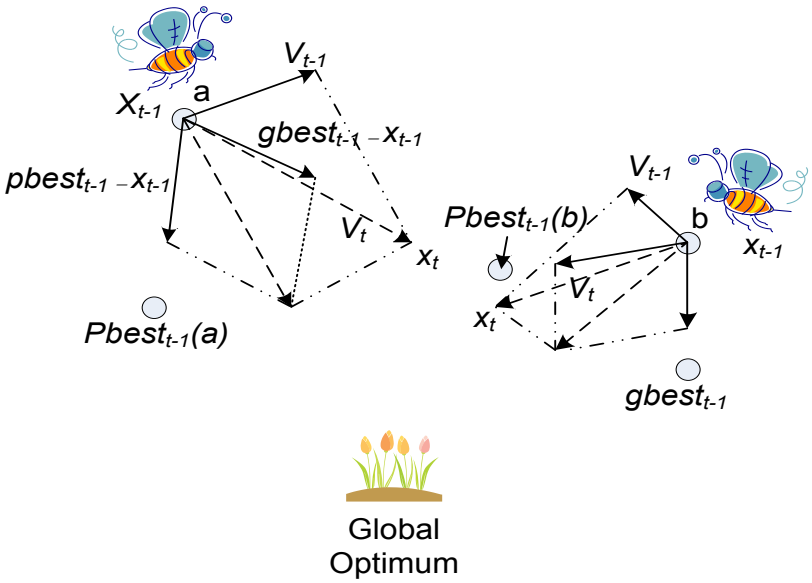

Fig. 34. Concept of PSO algorithm

Each member or particle of the group or swarm has a position and velocity in multi-dimensional space. This multidimensional space represents the solution space that is being searched. Each dimension represents one variable in the problem to be solved, so N-dimensional particle's position $X = \{x_1, x_2, \ldots$ is a solution of the problem. Particles are randomly or specifically initialized within the solution space, and moved by the swarm intelligence to achieve the goal of optimizing a specific fitness function, which designates the desired system performance. Every particle remembers the best position they have visited, communicated with each other, adjust their position and velocity based on the good position they found. The personal best location, *pbest,* is updated by the latest calculated fitness value of each particle, and then the global best location, *gbest,* is updated according by comparing the previous *gbest* with current *pbest.* Then the velocity and position of each particle for the next iteration are updated by [31]

$$\bar{v}_{t,n} = w\bar{v}_{t-1,n} + c_1 r_1(\bar{x}_{pbest_{t-1,n}} - \bar{x}_{t-1,n}) + c_2 r_2(\bar{x}_{gbest_{t-1}} - \bar{x}_{t-1,n}) \tag{26}$$

$$\bar{x}_{t,n} = \bar{x}_{t-1,n} + \bar{v}_{t,n} \tag{27}$$

where $v_{t,n}$ and $x_{t,n}$ is the velocity of the particle and the position of the particle in the nth dimension at t iteration, respectively. c_1 is a factor determining how much the particle is influenced by the memory of his best location, c_2 is a factor determining how much the particle is influenced by the rest of the swarm [33]. The constant c_1 and c_2 have normally same value of 2. r_1 and r_2 are random numbers between 0 and 1, and give a unpredictability to particle's movements. w is inertial weight, and this number (chosen to be between 0.0 and 1.0) determines to what extent the particle remains along its original course unaffected by the pull of *gbest* and *pbest* [33].

5.3 Element design

The radiating element which will be used in the proposed reflectarray is designed and shown in Fig. 35. The unit cell consists of two multi-resonant elements using a ring and a circular patch on two substrate layers. In this design, the radius of each ring and circular patch (r_1, cr_1, r_2, cr_2), and the gap between the ring and the circular patch on the bottom layer (g_2) are variable, and the gap on top layer (g_1) is fixed at 0.2mm. The relative size of the rings and the circular patches are fixed in the design ($r_2 = 1.1 \times r_1$, $cr_2 = 1.2 \times cr_1$). The unit cell is a square lattice with a side length of 7mm, which is 0.51 λ_0 at 22 GHz, in both the x- and y- directions, and it is simulated using RT/Duroid 5870 substrate with $\varepsilon_r = 2.33$ and $h = 0.79$mm.

Fig. 36 shows the simulated phase and amplitude values of the reflection coefficient, as a function of the radius of the ring and different frequencies. The phase range obtained is around 1300º under normal incidence.

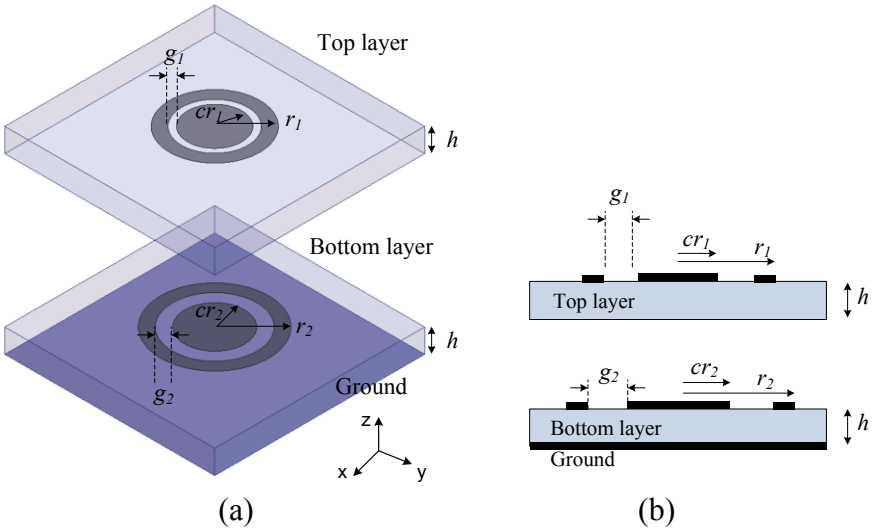

Fig. 35. Stacked multi-resonant element: (a) prospective view, (b) side view

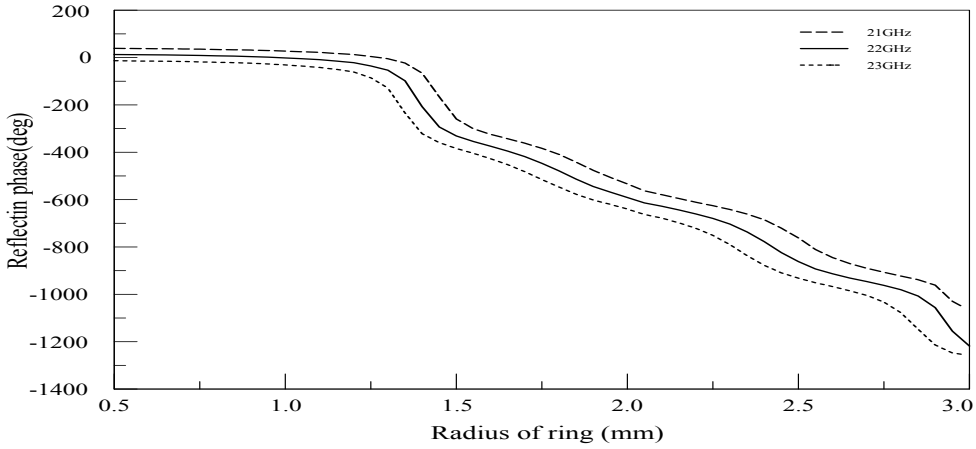

(a)

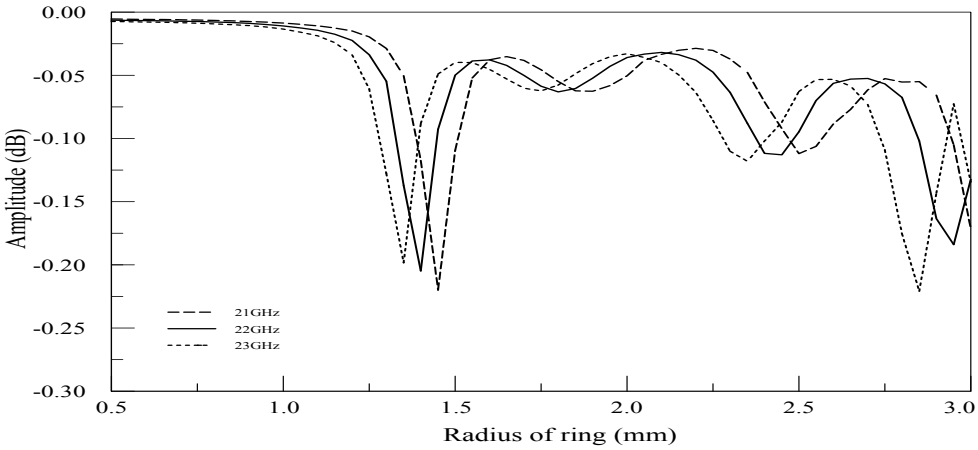

(b)

Fig. 36. Reflection coefficient as a function of different frequencies: (a) phase, (b) amplitude

5.4 Optimization process

Fig. 37 shows the design process of the reflectarray using a PSO routine. First, using Equation(7), the required phase of the reflection coefficient, φ_n, for nth element is determined at three different frequencies of f_c, f_l, and f_u, where f_c, f_l, and f_u are center, lower and upper band edge frequencies, respectively, in order to achieve a re-radiated

field with the proper phase in a predetermined frequency band from f_l (21GHz) to f_u (23GHz). Next, the optimized phase of each element is obtained with PSO routine to minimize a cost function defined as

$$e(m,n) = \sum_{i=l,c,u} \left(\phi^r(f_i)(m,n) - \phi^a(f_i)(m,n) \right)^2 \tag{28}$$

where *e(m, n)* is a cost function for each element located on *m*th and *n*th array grid. ϕ^r and ϕ^a are the required phase based on the antenna geometry and the calculated phase response of the unit cell, respectively. For center frequency, the cost function is obviously zero.

Fig. 38 and Fig. 39 show the difference of the phase distribution of the original and PSO optimized reflectarray surface.

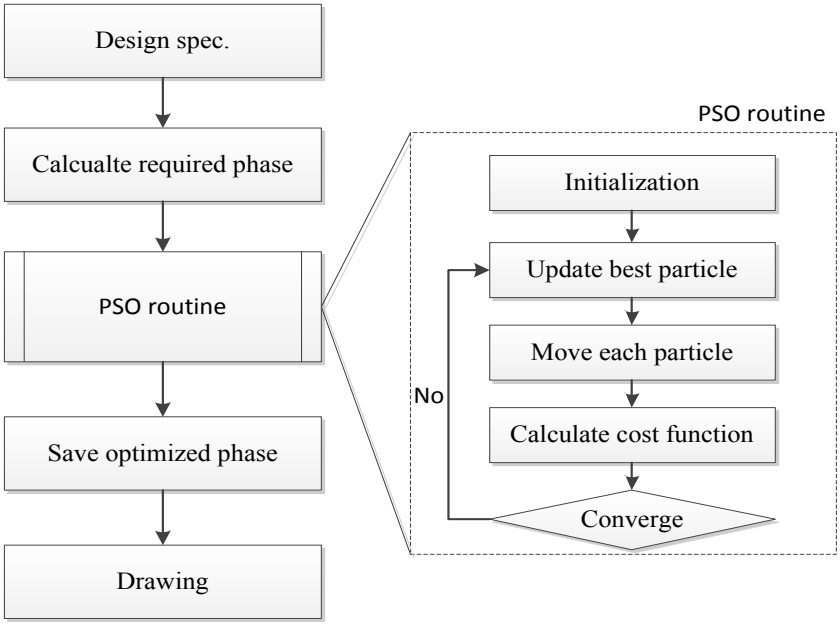

Fig. 37. Design process using PSO optimization

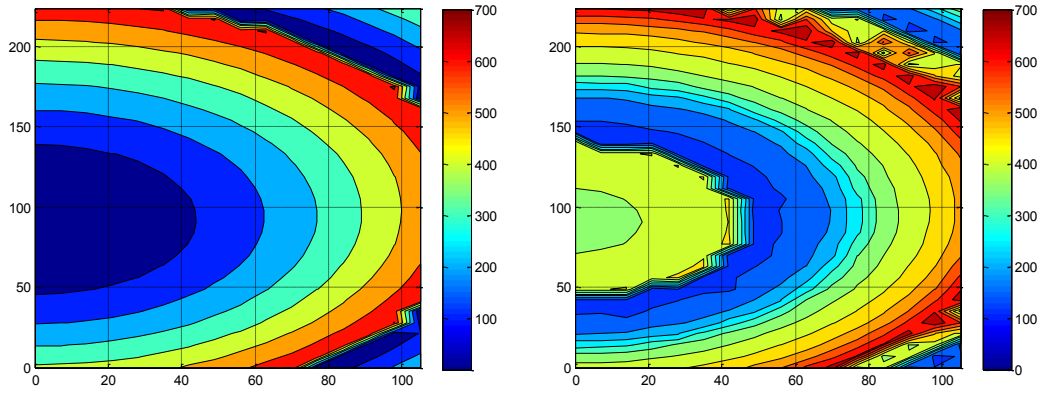

(a) (b)

Fig. 38. Comparison phase distributions between (a) non-optimized and (b) optimized process

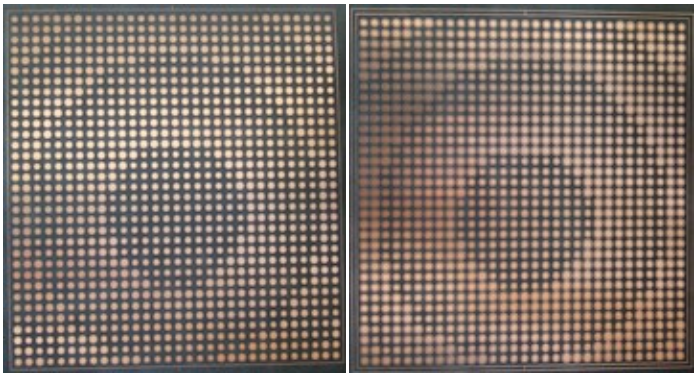

(a) (b)

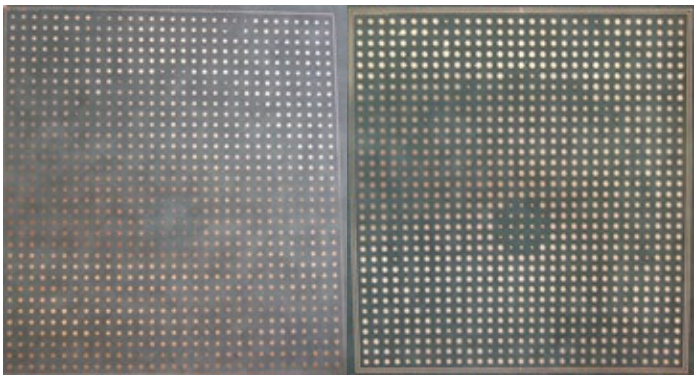

(c) (d)

Fig. 39. Fabricated reflectarrays: (a) top and (b) bottom layer of the PSO optimized array, (c) top and (d) bottom layer of the non-optimized array

5.5 Measurement results

Two 220 mm × 230 mm offset-fed reflectarrays were fabricated and measured. Fig. 39 shows the fabricated prototype reflectarrays using 31 × 33 (1,023) stacked multi-resonant elements printed on two substrates. The offset angle θ, between the feed horn boresight and the normal direction to the array surface was set to 20° to avoid field blockage due to the feed horn antenna. The f/D ratio of the parent parabolic reflector was set to 1. According to the parent reflector configuration, the feed horn antenna was located at a distance of R_f = 250 mm from the array lower edge. The gain of these prototype reflectarray was measured by comparison with a standard gain horn antenna.

Fig. 40 shows the radiation pattern at center and edge frequencies of non-optimized and optimized reflectarray. As shown in the figure, a very stable gain was achieved for the optimized reflectarray in the band. Fig. 41 shows 1dB gain bandwidth of 9.7% for the optimized reflectarray.

5.6 Conclusions

A 1,000 double-layer reflectarray with stacked multi-resonant ring and circular patch was designed for broadband bandwidth performance using Particle Swarm Optimization method. It shows a 1dB gain bandwidth is equal to 10% and gain stability.

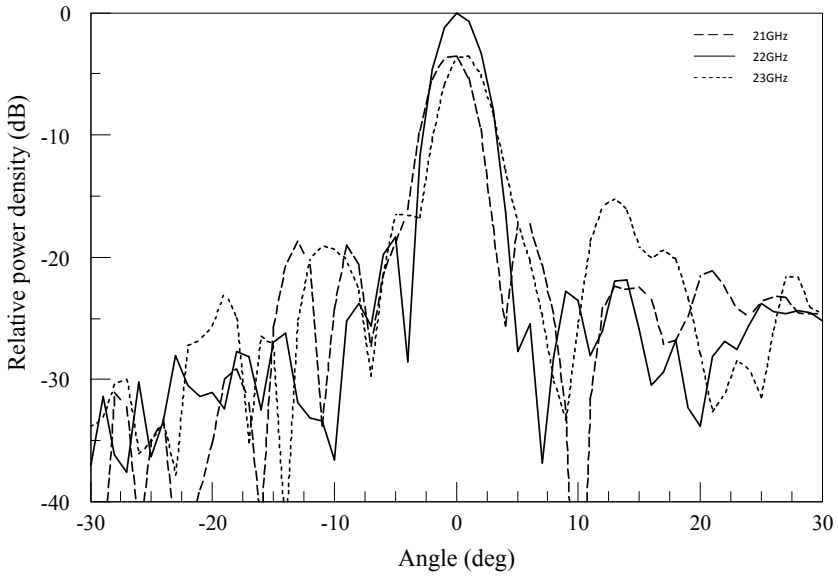

(a)

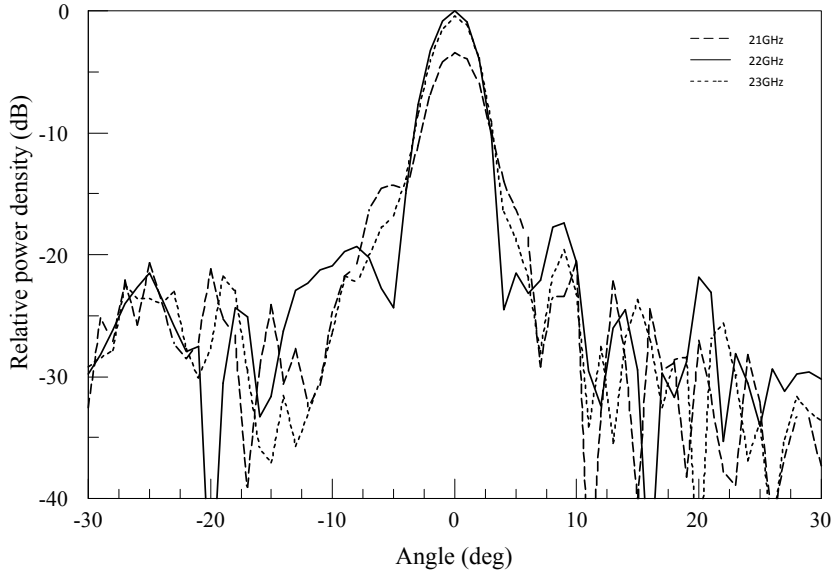

(b)

Fig. 40. Radiation patterns in 21-23GHz band. (a) Non-optimized reflectarray, (b) Optimized reflectarray

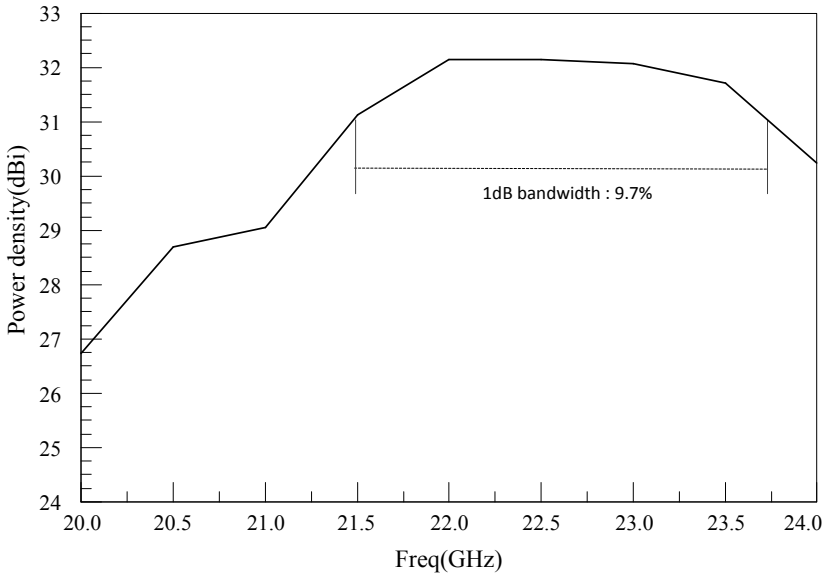

Fig. 41. Measured gain as a function of frequencies

CHAPTER VI

SIX-BAND REFLECTARRAY ON TWO LAYER

6.1 Introduction to multiband reflectarray

The objective of this project is to study, analysis and design for the development of a multi-frequency shared-aperture reflectarray antenna for the National Oceanic and Atmosphere Administration's (NOAA) future large-aperture radiometer and imaging antenna at Medium Earth Orbit (MEO). Table 1 shows the performance goals of the multiband reflectarray. This reflectarray should support at least 6 frequency bands and no more than 10 frequency bands. The specifications given by JPL are as follows.

Table 1. Performance goals

Parameter	
No. of frequency bands	Minimum of 6 to maximum of 10
Aperture size	0.75 meter (scalable to larger size)
Bandwidth	Not available (generally narrow)
Efficiency	40 %
Polarization	See Table I - 2
Peak side lobe level	-30 dB

6.2 Configuration of reflectarray

Six more important frequency bands selected for this reflectarray are 6.625, 18.7 52.5, 57.5, 166, and 183.31 GHz. The polarization required for each frequency band is listed in Table 2.

Table 2. Frequency plan and polarization

Frequency (GHz)	Polarization
6.625	Dual linear polarization (V and H)
18.7	Dual linear (V and H) and Dual CP (RHCP and LHCP)
52.5	Single linear (V)
57.5	Single linear (H)
166	Single linear (V)
183.31	Single linear (V)

The types of the elements selected at different frequency will have significant effects on the amount of coupling among elements and arrangements of each layer. Possible element types at each frequency band are listed in Table 3. The dual ring configuration can be used for achieving a wider phase range.

Table 3. Element types at different frequency bands

Frequency (GHz)	Element type
6.625	Ring or cross dipole
18.7	Cross dipole
52.5	Ring with gap, dipole
57.5	Ring with gap
166	Dipole
183.31	Dipole

The reflectarray will consist of 2 thin substrate layers and 2 foam spacers. The substrate selected for the proposed design is Roger/flex 3850 circuit material with the thickness of 0.0508mm. The thicknesses of the foam layers are pre-determined to be 0.6mm and 1mm for the top and bottom layer respectively after optimized simulations. Each substrate layer will accommodate three frequency bands as shown in Fig. 42. Element spacing for each frequency band will be determined later with considerations of the coupling effects, grating lobes, and limited real estate of the array.

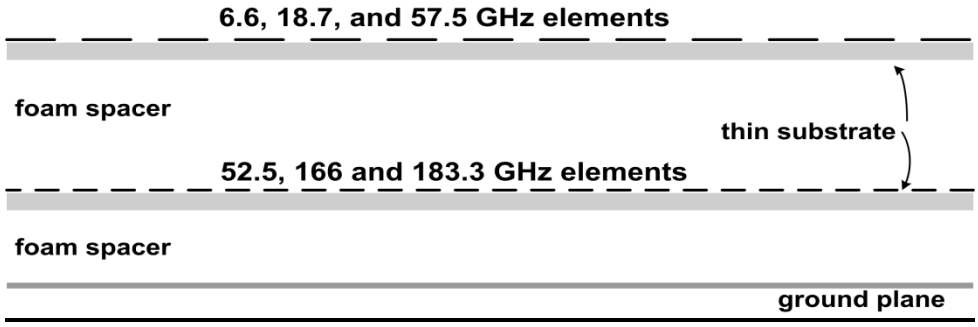

Fig. 42. A configuration of layer of the reflectarray

6.3 Top layer element design

In order to minimize the blockage produced by the elements at the top layer, the elements at the top layer was designed to reduce the thickness and to increase the element spacing. Fig. 43 shows the arrangement of elements on the top layer. The 18.7 GHz element, the element of middle frequency band at the top layer, will be designed first and then other elements will be designed afterward.

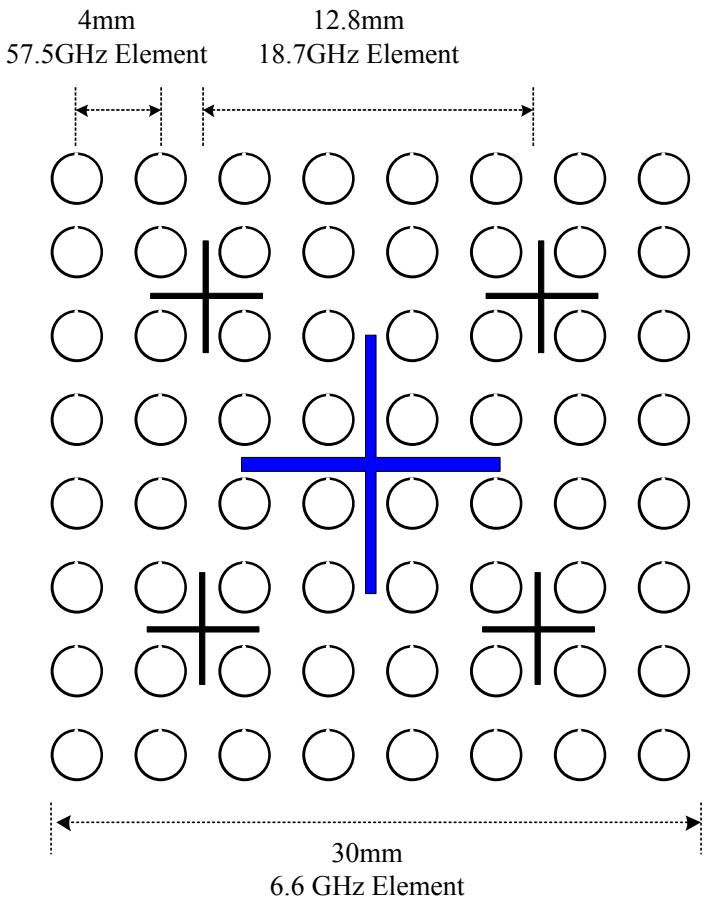

Fig. 43. Arrangement of the top layer

A. 18.7 GHz element

Fig. 44 shows the simulation setup of the unit cell at 18.7GHz. The dimensions of the unit cell are chosen to be 12.8mm (0.8 λ_o) x 12.8mm (0.8 λ_o) and the arm length of the cross dipole are varied for different phases of the reflected wave. Results of reflected phases versus lengths with different widths of arms are shown in Fig. 45. As can be seen from the results, a phase variation range for 0.2mm to 1.6mm of width can be from 327º to 286º. 0.2mm element arm width is chosen for 18.7 GHz for reducing the blocking the bottom layer elements.

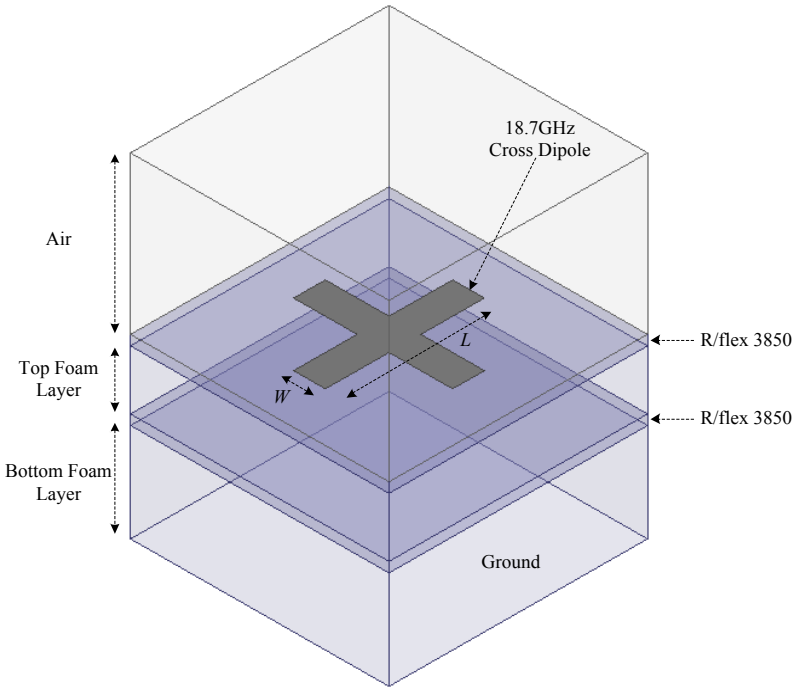

Fig. 44. Simulation setup of a unit cell of the 18.7GHz element

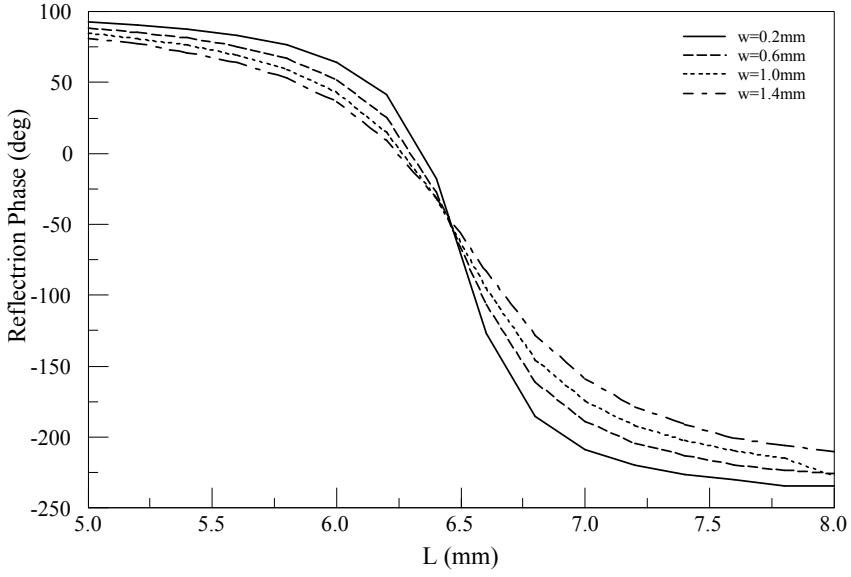

Fig. 45. Phase response as a function of the dipole width (*w*)

B. 57.5 GHz element

The simulation setup of the 57.5 GHz is shown in Fig. 46. The dimensions of the unit cell are chosen to be 4mm (0.77 λ_o) × 4mm (0.77 λ_o). According to Fig. 47, the total phase variation ranges of the circular loop for different loop width(2) vary from 294º to 118º. Therefore loop width is chosen to 0.1mm for large phase variation range and less blockage. Gap width(Gw) also is selected to 0.1mm.

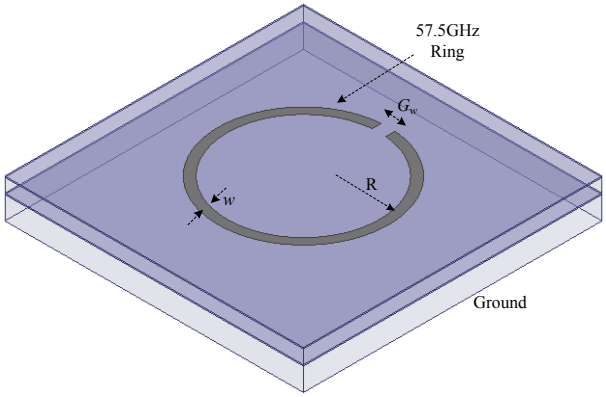

Fig. 46. Simulation setup of unit cell of the 57.5GHz element

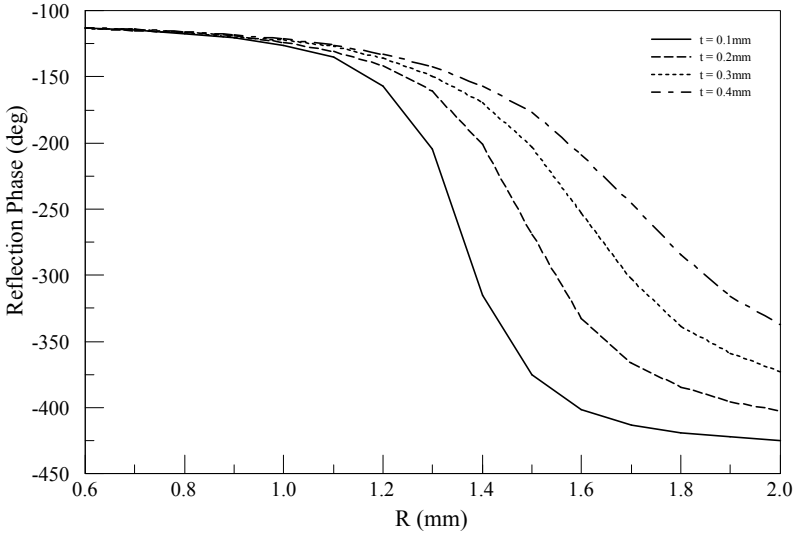

Fig. 47. Phase response as a function of the ring width (*w*)

C. 6.6 GHz element

The dimensions of the unit cell are chosen to be 26 mm (0.79 λ_o) × 26 mm (0.79 λ_o) and the arm length of the cross dipole are varied for different phases of the reflected wave. Fig. 48 and Fig. 49 show the simulation setup of a unit cell working at 6.6 GHz and the reflected phase responses, respectively. The result indicate the width of the cross dipole does not effect on the total reflected phase range significantly, but the dipole width is chosen to 0.4mm for fewer blockages.

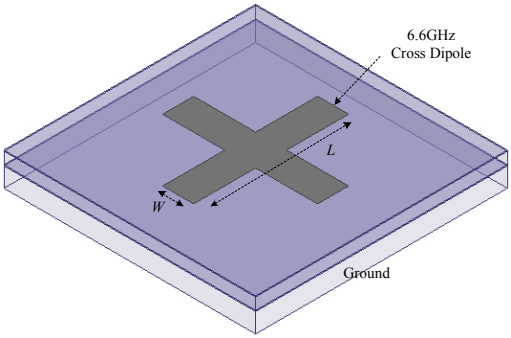

Fig. 48. Simulation setup of a unit cell of the 6.6 GHz element

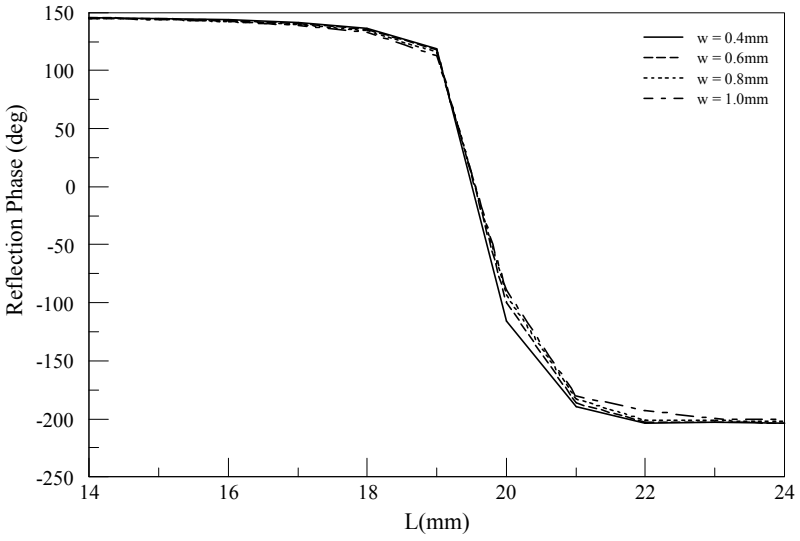

Fig. 49. Phase response as a function of the arm width (*w*)

6.4 Bottom layer element design

The focus of the bottom layer design is on the elements of 52.5, 166, and 183 GHz. At such high frequencies, the element selection and design could be very critical. Simple element shapes, i.e. rectangular patches and dipoles, are chosen as the reflectarray elements at the high frequencies. Fig. 50 shows the arrangement of the bottom layer.

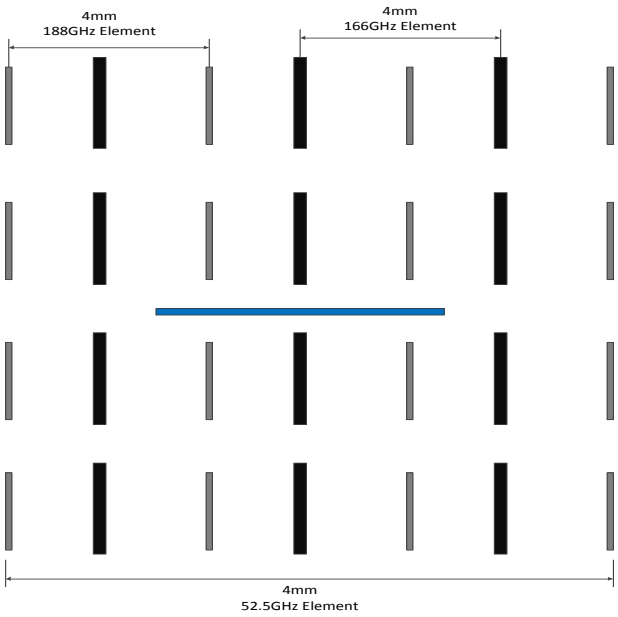

Fig. 50. Arrangement of the bottom layer

A. 166 GHz element

The geometry of 166 GHz elements is shown in Fig. 51, which show the simulation setup of a unit cell. The dimensions of the unit cell are chosen to be 1.3mm (0.72 λ_0) x 1.3mm (0.72 λ_0) to take into account coupling with adjacent unit cell. Both the 166 and 183 GHz elements are placed in the unit cell so that the effects of one element on the other could be taken into considerations. The thickness of the copper cladding is also considered in the simulations for better accuracy. The width of the rectangular patch is

fixed at 0.22 mm and the length is varied for different phases of the reflected waves. The height of top and bottom foam layer is 0.6mm and 1.1mm, respectively. The phase variation range is about 315^{o} as shown in Fig. 52.

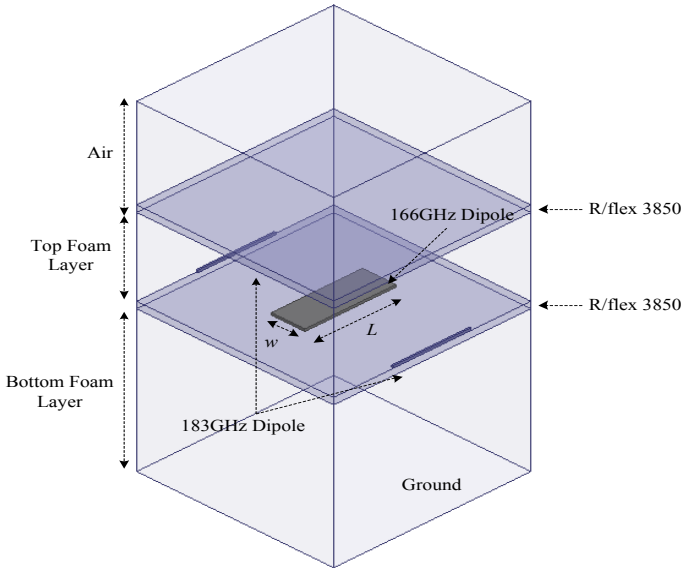

Fig. 51. Simulation setup of unit cell of the 166 GHz element

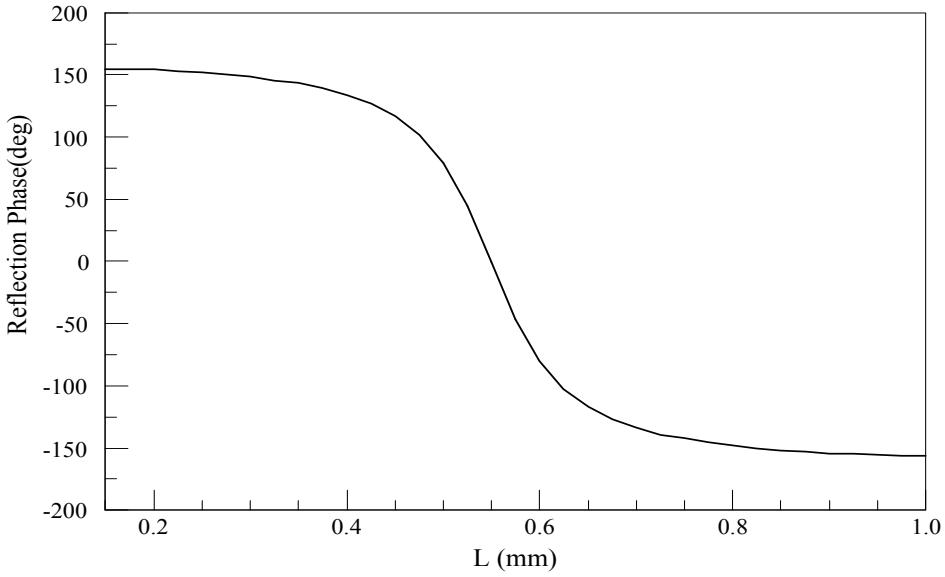

Fig. 52. Phase response as a function of the dipole length

B. 183 GHz element

As what have been done in the previous simulations, the unit cell also includes the 166 GHz elements to take into account the possible mutual coupling effects in Fig. 53. The unit cell size is the same as the size at 166 GHz and the width of the dipole is 0.1 mm. As shown in Fig. 54, the phase variation range is about 320 ^{o}.

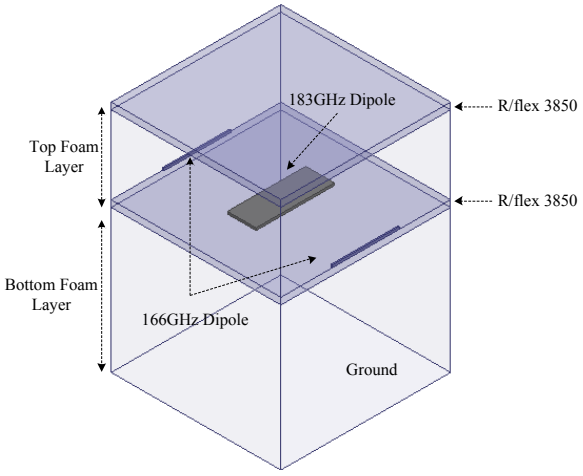

Fig. 53. Simulation setup of unit cell of the 183GHz element

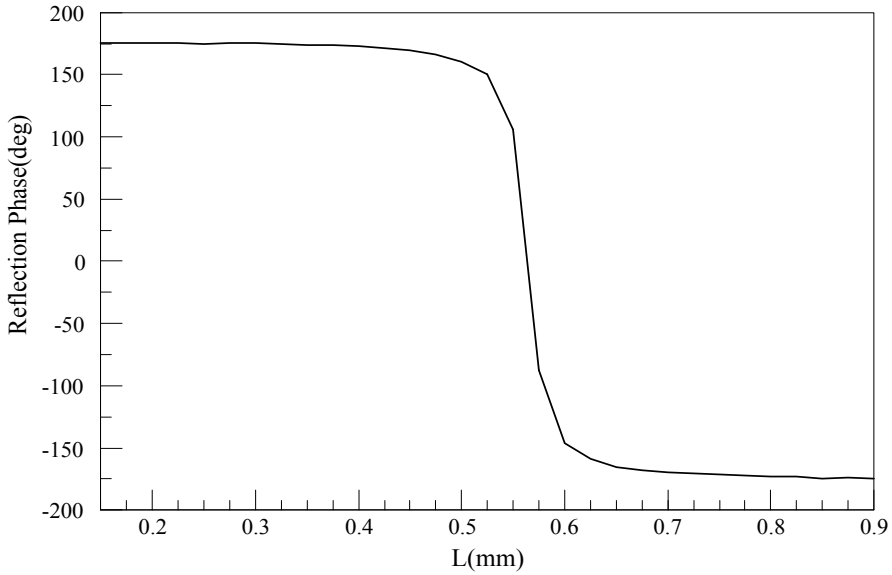

Fig. 54. Phase response as a function of the arm length

C. 52.5 GHz element

Dipoles with variable lengths are used for the 166 and 183 GHz bands. The choices of the element type at the 52.5 GHz are limited by the 166 and 183 GHz elements which are located at the same layer. Dipole elements are used again for the 52.5 GHz as shown in Fig. 55, but they are oriented vertically in perpendicular to the 166 and 183 GHz elements. Fig. 56 shows the phase variation range of 290° which is achieved by changing the dipole length.

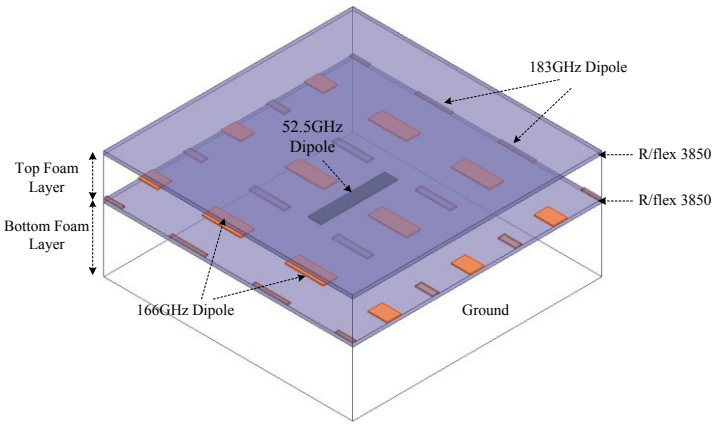

Fig. 55. Simulation setup of unit cell of the 52.5 GHz element

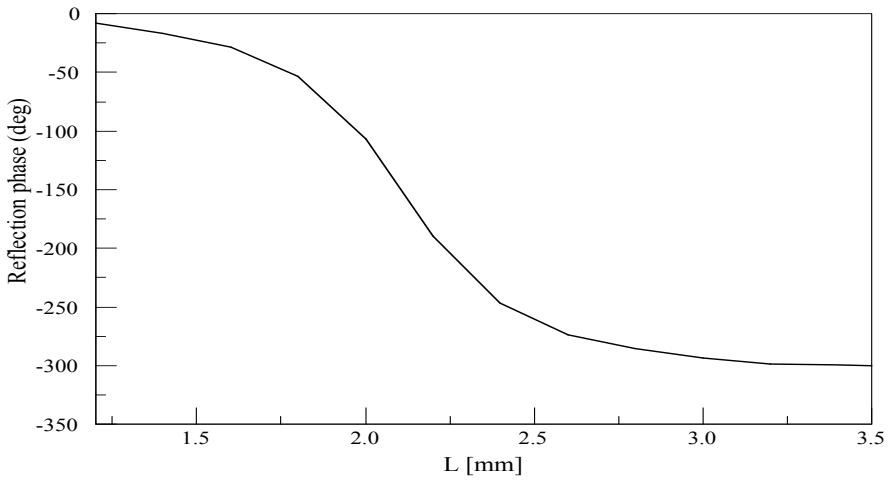

Fig. 56. Phase response as a function of the dipole length

6.5 Coupling effects with neighborhood elements

In this chapter, various cases of intersections are investigated, for example, cases between elements at different frequencies band on top layer, cases between elements on bottom layer, and cases between elements on top layer and ones on bottom layer. As shown in Fig. 57 and Fig. 58, though the top and bottom elements are placed together in a unit cell of radiating elements, each element can obtain the necessary reflection phase. The reflection phases are shifted but the phase variation ranges are similar.

6.6 Conclusions

This chapter presents a reflectarray configuration which supports the operation of six frequency bands. The proposed reflectarray has two substrate layers and each layer accommodates array elements of three frequency bands. The reflection phase curves of the array elements of different frequency bands are simulated and summarized in Table 4. Interactions among the elements are also explored. Detailed results of the reflection phase curves in different situations have been presented in this chapter. Based on the high accuracy of the simulation software, these results are believed to be reliable and are ready for real implementation of the reflectarray.

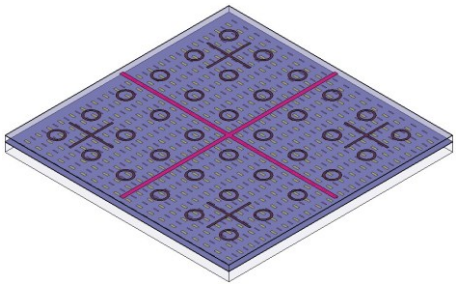

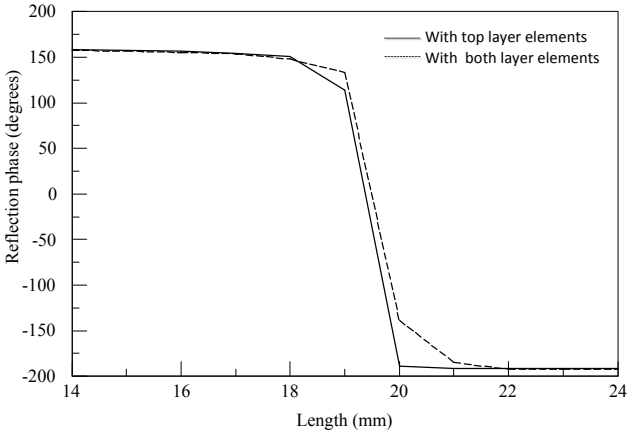

(a)

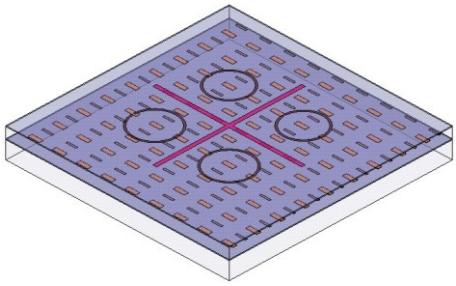

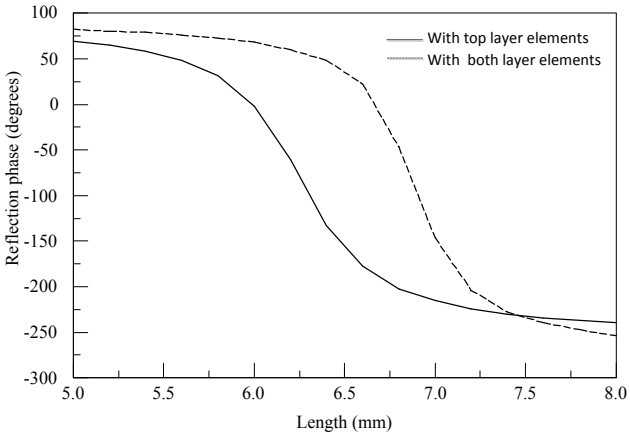

(b)

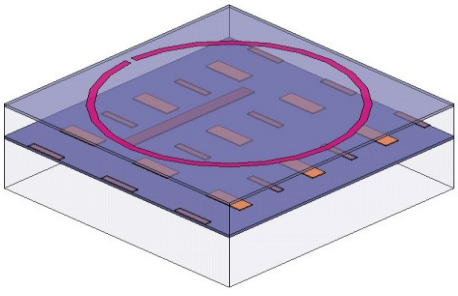

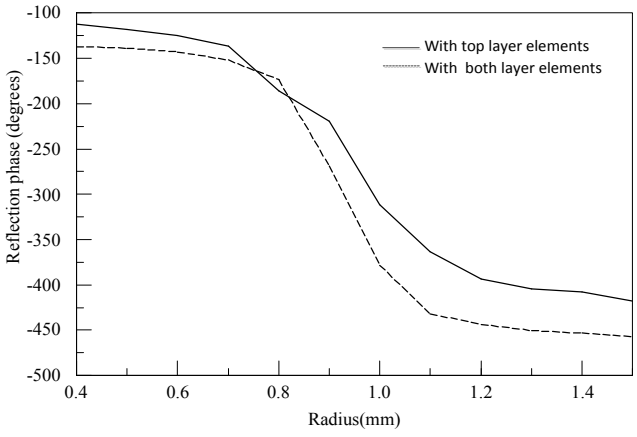

(c)

Fig. 57. Coupling effects on the elements on top layer: (a) 6.6GHz, (b) 18.7GHz, and (c) 57.5GHz

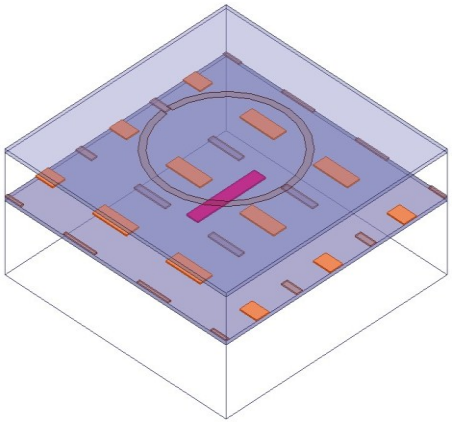

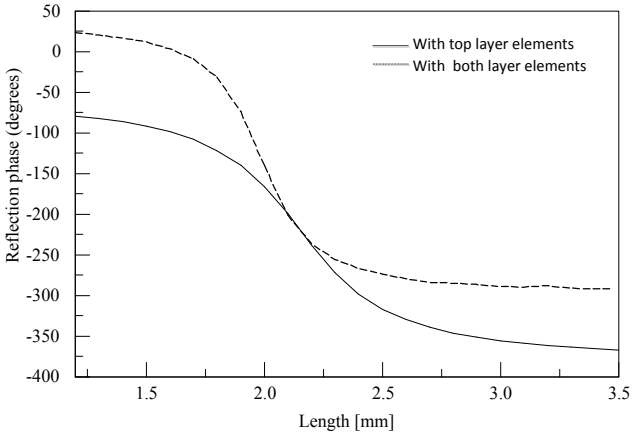

(a)

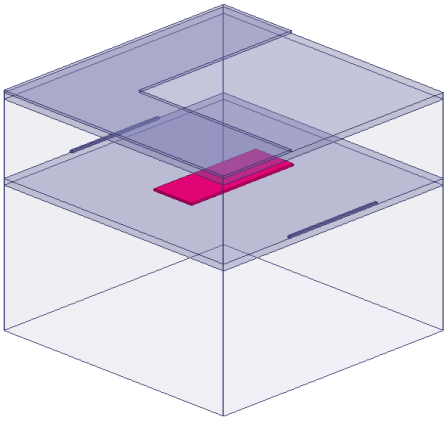

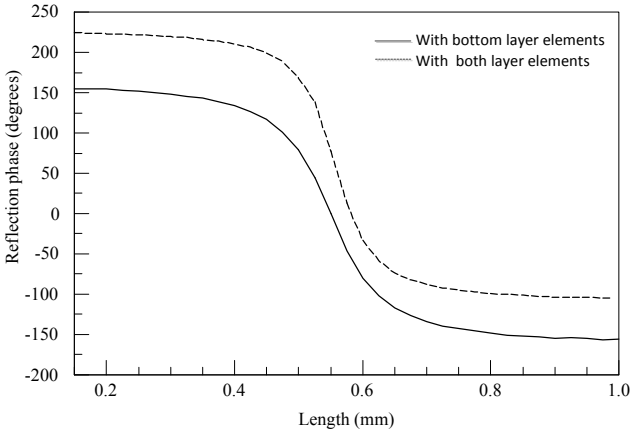

(b)

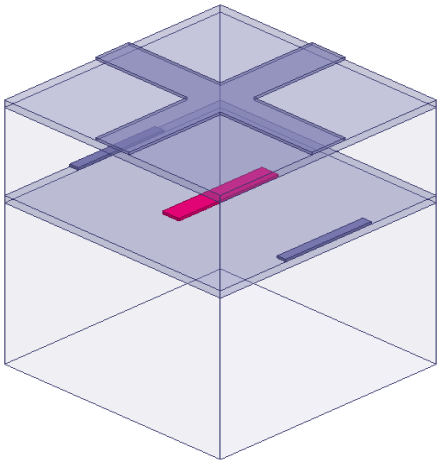

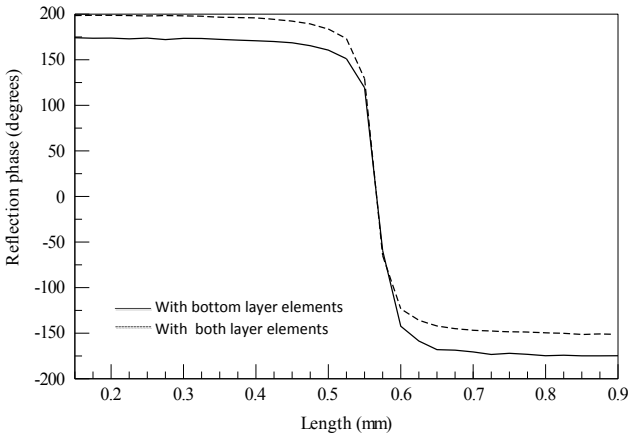

(c)

Fig. 58. Coupling effects on the elements on bottom layer: (a) 52.5GHz, (b) 166GHz, and (c) 183GHz

Table 4. Design parameters of the reflectarray elements

Top layer				
Freq.	Shape	Element description	Element spacing	Single element achievable reflection phase range
6.6 GHz	Cross dipole	Equal arm length Width: .0.4mm	0.79 λo	355°
18.3 GHz	Cross dipole	Equal arm length Width: 0.2mm	0.80 λo	327°
57.5 GHz	Circular ring with gap	Width: 0.1mm Gap: 0.1mm	0.77 λo	295°
Bottom layer				
Freq.	Shape	Element description	Element spacing	Single element achievable reflection phase range
52.5 GHz	Horizontal Dipole	Width: 0.2mm	0.68 λo	290°
166 GHz	Vertical Dipole	Width: 0.22mm	0.72 λo	315°
183 GHz	Vertical dipole	Width: 0.1mm	0.79 λo	320°

CHAPTER VII

RECTIFYING ANTENNA USING REFLECTARRAY

7.1 Introduction to rectenna

Space solar power transmission (SPT) and microwave wireless power transmission (WPT) have been attracted not only for an alternative solution to world energy problems in the future, but also for modern commercialized uses such as radio frequency identification charger, or battery or power line free devices. The rectifying antenna called rectenna is one of the most key components in the SPT and WPT system. Among many technical developments in WPT history, the rectenna technologies have been dominantly improved for the system performance and efficiency improvement [36-38].

Traditionally, dipoles or dipole-like antennas are used in rectenna design [39]. The coplanar stripline (CPS) is normally used to feed the antenna in a rectenna system due to easy fabrication and high characteristic impedance [40-42]. In recent years, several different types of rectenna with different performances have been reported. A harmonic-rejecting circular sector rectenna for avoiding filter sections in rectenna circuits was reported [43]. A circularly polarized dual band rectenna was developed for portable wireless device applications [44]. Another circular polarized rectenna with two slot patch antennas was built for dual band performances: one resonant band is for data communication and the other is for wireless power transmission [45]. To prevent the output voltage variations due to improper main beam alignment, a non-uniform rectenna

array was proposed [46]. Another solution to have constant output power is to use a retrodirective array [47-49]. The automatic beam steering features have been widely used in many wireless communication systems [50, 51]. Retrodirective rectennas also have been developed using bow-tie antenna and microstrip ring elements [52, 53].

To provide high DC output power, the rectenna system needs to receive a large amount of incoming RF power. To achieve this, high gain antenna element or a large antenna array for high gain performance are necessary. In this chapter, the WPT system and the rectenna operation theory are reviewed, and then an efficient high gain rectenna with pentagon rings is presented.

7.2 Wireless power transmission system

The main difference between the WPT system and communication systems is transferred power efficiency. Normally, the communication systems receive signals from all directions when the transmitters diffuses the signals while the WPT systems focus on a point receiver or pointed receivers for efficient wireless power transfer. So, even though the received signals have enough power for communications, the efficiency of the communication system is very low comparing with the WPT system. Therefore, efficiency is critical factor in the design of the WPT system. A WPT system consists of three main functional blocks as shown in Fig. 59. The first block is DC-to-RF transmitter. The original DC energy is converted to RF energy and the converted RF is radiated in the first block. The original DC source is collected by either photovoltaic cells or solar thermal turbines.

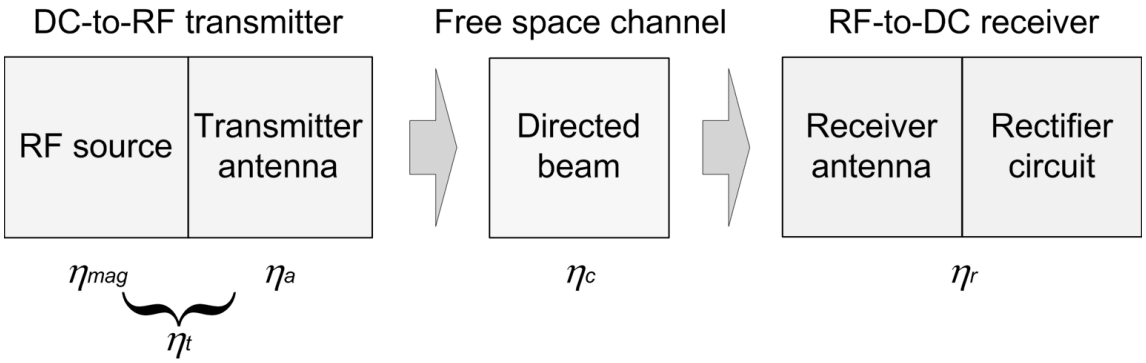

Fig. 59. Wireless power transmission system schematic

The DC to microwave convertor is either microwave tube (magnetron) system or semi-conductor systems. The antenna element or array antennas are used to radiate the RF energy. The efficiency (η_t) of the first block, the electric to microwave conversion efficiency, is equal to the product of magnetron efficiency (η_{mag}) and the array antenna efficiency (η_a). The magnetron efficiency is used to express how efficient the RF source works. The antenna efficiency at the transmitter represents the ability of the antenna to radiate the distributed RF power fed from the RF source and radiated into free-space.

The second block is free space channel. The radiated RF power from the array antenna is transferred across free space within a specific focused beam towards a receiver. The efficiency (η_c) is this block, collection efficiency, is the ratio of the received power over the transmitted power. For maximum collection efficiency, an optimum power density distribution must be selected for the transmitting antenna aperture. A non-uniformly illuminated aperture increases the collection efficiency and it has been seen that the optimal taper is of Gaussian type. The collection efficiency is proportional to a design parameter, which is expressed as Goubau's relation [54, 55].

$$\tau = \frac{\sqrt{A_r A_t}}{\lambda_0 D} \tag{29}$$

where A_r and A_t are the aperture areas of the receiver and the transmitter antennas. As can be seen from this equation, Goubau's relation can be used to determine the size of the apertures involved. The collection efficiency is given by

$$\eta_c = (1 - \mathrm{e}^{-\tau^2}) \times 100\% \tag{30}$$

which is proportional to the power density and the incremental area of the antenna. For example, as A_t becomes larger, the incident power density also increases leading to a higher collection efficiency as seen through. This translates into a tradeoff between the efficiency and the size.

The last block is RF-to-DC receiver, where rectennas rectify the incoming RF signals to generate DC output power. Fig. 60 shows the basic components of the rectenna element. An antenna element attaches to a RF filter (bandpass or lowpass filter) that transforms the impedance of the antenna to the rectifier impedance and prevents the high-order harmonics resulted from the rectifier reradiating.

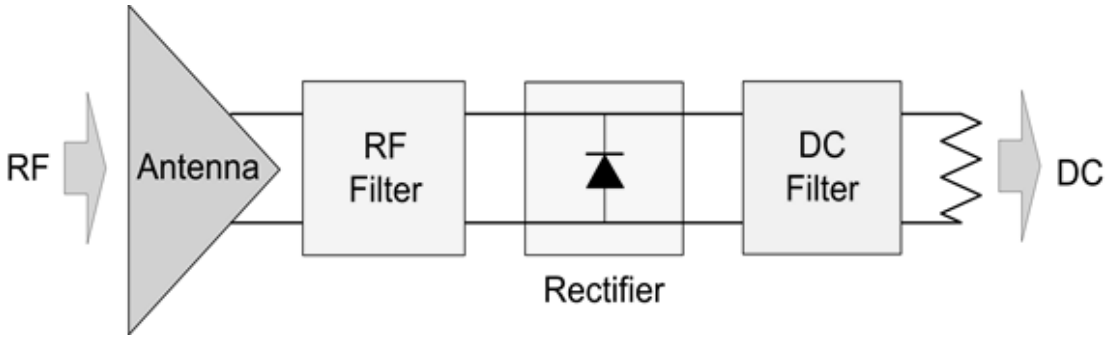

Fig. 60. Rectenna block diagram

The rectifying diode is the core element of the rectifier. The output DC filter of a large capacitor effectively shorts the RF energy and passes the DC power. A load resistor is placed at the output terminal to measure the DC output voltage. The efficiency of this block is called rectenna efficiency.

The overall efficiency (η_{all}) of a WPT system is the ratio of the DC output power at the receiver end over the DC (or RF) input power at the transmitter end, which is given by

$$\eta_{all} = \eta_t \cdot \eta_c \cdot \eta_r \tag{31}$$

which means that the end-to-end efficiency includes all the sub-efficiencies starting from the DC supply feeding the RF source in the transmitter to the DC power interface at the receiver output.

7.3 Rectenna operation theory

It is important to understand how a half-wave rectifier with shunt capacitor works, which is the fundamental theory used for a microwave rectenna design. The basic theory of the half-wave rectifier can be found in [56]. The rectenna operation theory has been studied in [40, 41]. In this chapter, several important concepts are reviewed.

A. Rectifying circuit theory

The rectenna circuit consists of the half-wave rectifier circuit and the DC-pass capacitor where the capacitor is in shunt with the diode as shown in Fig. 61 (a). The voltage across the load as a function of time is

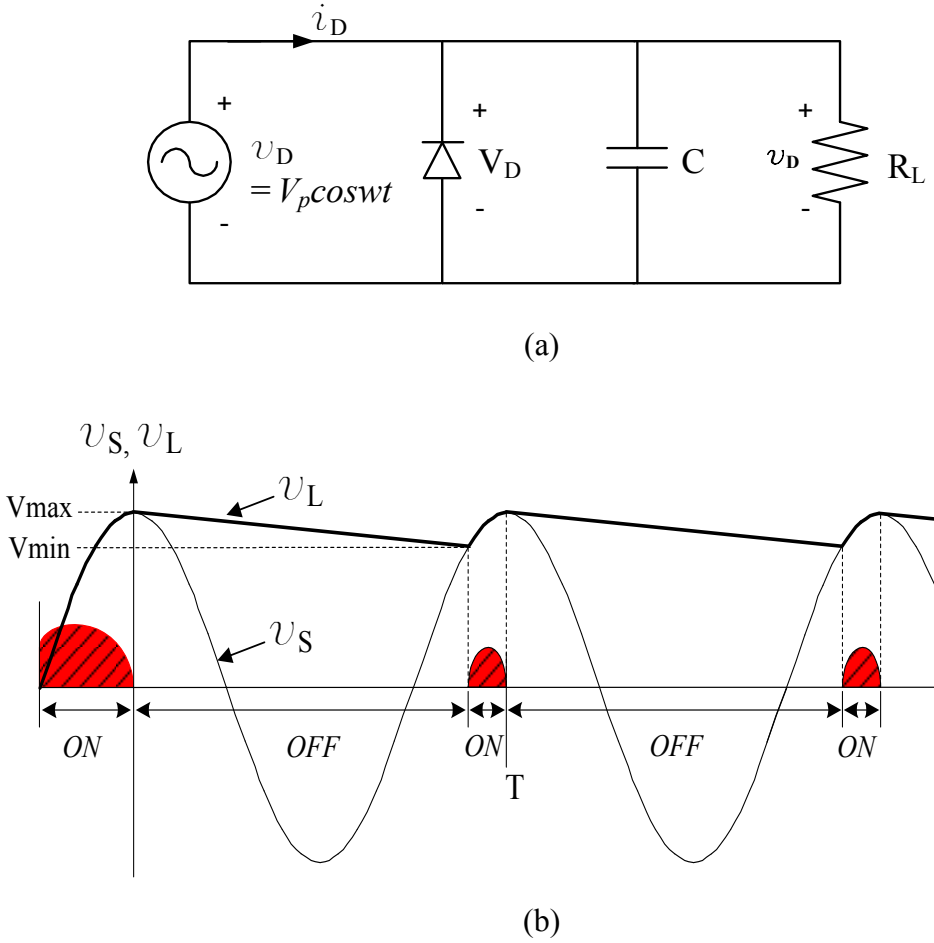

Fig. 61. (a) Half-wave rectifier with capacitor and (b) its waveforms

$$\upsilon_L(t) = 0 + (V_P - 0)e^{-\frac{t}{R_L C}} = V_P e^{-\frac{t}{R_L C}} \tag{32}$$

where $R_L C$ is the time constant, V_P is the initial value and 0 is the final voltage if the capacitor completely discharges. The time t is measured from the peak where the voltage is equal to V_P. When the rectenna's operating frequency has such a short period in comparison with the $R_L C$ time constant, the exponential decrease in the voltage can be approximated by a straight line as shown in Fig. 61 (b).

By series expanding, equation (32) becomes

$$\upsilon_L(t) = V_P e^{-\frac{t}{R_L C}} = V_P \left(1 - \frac{t}{R_L C} + \frac{\left(\frac{t}{R_L C} \right)^2}{2} - \ldots \right) \tag{33}$$

Since the decreasing voltage has been approximated as a straight line, the linear terms of the equation (33) are kept and the minimum voltage at $t = T$ becomes

$$V_{\min} \approx V_P \left(1 - \frac{T}{R_L C} \right) = V_P \left(1 - \frac{1}{f R_L C} \right) \tag{34}$$

Once the diode voltage drops to V_{min}, the diode turns on and the voltage again approaches $V_{max} = V_P$. The peak-to-peak ripple of the voltage waveform is

$$V_r = V_{\max} - V_{\min} = \frac{V_P}{f R_L C} \tag{35}$$

and the average DC diode voltage present across the load resistor is

$$V_D = \frac{V_{\max} - V_{\min}}{2} = V_P \left(1 - \frac{1}{2 f R_L C} \right) \approx V_P \tag{36}$$

The period of the incoming 5.8 GHz energy is 172.4 ps. The capacitance of the DC-pass filter is approximately 2400 pF. This translates to $R_L C >> T$. Therefore, the ripple voltage V_r is very small, and the average diode DC voltage is $V_D \approx V_P$. This average DC diode voltage is also known as the self-bias voltage used in further analysis.

B. Diode modeling

Fig. 62 shows a RF voltage waveform operating across the diode and the diode junction voltage. This model assumes the harmonic impedances seen by the diode are either zero of infinite that avoids the power loss by the harmonics. The fundamental

voltage wave will not be corrupted by the higher order harmonic components. Then the rectenna conversion efficiency only depends on the diode electrical parameters and the circuit losses at DC and the fundamental frequency. The voltage waveform can be expressed as

$$V_I = -V_D + V_P \cos(\omega t) \tag{37}$$

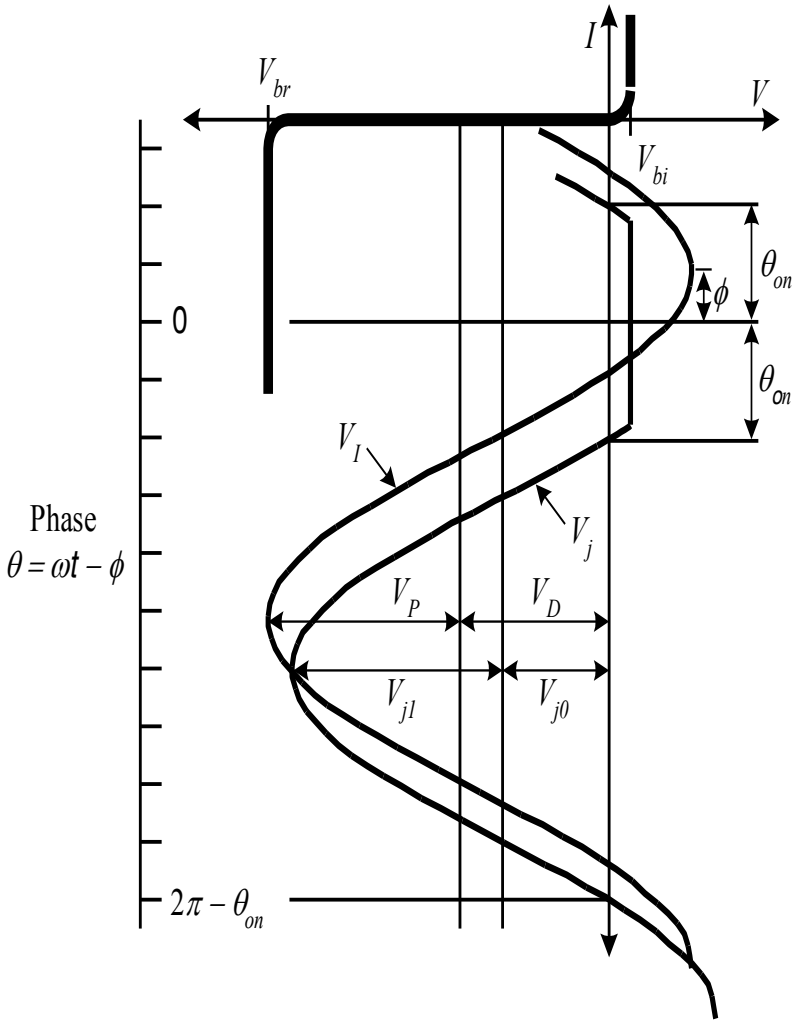

Fig. 62. Diode current-voltage characteristic curves with the incident fundamental and diode junction voltage waveforms

where V_D is the self-bias DC output voltage across the resistive load R_L, and V_P is the peak voltage amplitude of the incident RF power. The rectifying diode acts as a mixer that produces a self-bias voltage. As the incident power is increased, the rectified self-biasing will become more reversed biased. The diode junction voltage is

$$V_j = \begin{cases} -V_{j0} + V_{j1}\cos(\omega t - \phi), & V_j < V_{bi} \\ V_{bi}, & V_j \geq V_{bi} \end{cases} \tag{38}$$

where V_{j0} and V_{j1} are the DC and fundamental frequency components of the diode junction voltage, respectively; V_{bi} is the diode's built-in turn-on voltage; θ_{on} is the forward bias turn-on angle. When the junction voltage exceeds V_{bi}, the diode will operate in forward conduction. Fig. 62 also shows that the diode's junction waveform slightly lags the incident power by a phase difference ϕ.

The equivalent circuit used to determine the diode's efficiency is shown in Fig. 63. The diode parasitic reactive elements are excluded from the circuit. The diode model consists of a series resistance R_S, a nonlinear junction resistance R_j, a non-linear junction capacitance C_j, and a load resistor R_L. The junction resistance R_j is assumed to be zero for forward bias and infinite for reverse bias. Applying Kirchoff's voltage law in the equivalent circuit, we have

$$V_D + I_D R_S + V_{j,dc} = 0 \tag{39}$$

With $V_D = I_D R_L$, the DC output voltage is given by

$$V_D = -V_{j,dc}\frac{R_L}{R_S + R_L} \tag{40}$$

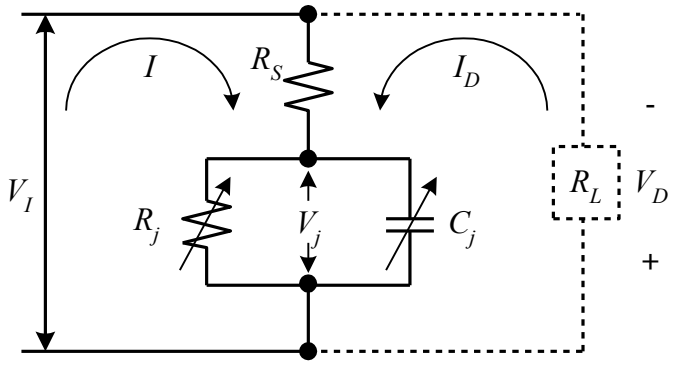

Fig. 63. Equivalent circuit model of the half-wave rectifier

The DC output voltage is determined from the rectified voltage across the diode junction V_j. In each cycle, the average value of V_j is

$$V_{j,dc} = \frac{1}{2\pi}\int_{-\theta_{on}}^{\theta_{on}} V_{bi}\ \mathrm{d}\theta + \frac{1}{2\pi}\int_{\theta_{on}}^{2\pi-\theta_{on}} \left(-V_{j0} + V_{j1}\cos\theta\right)\mathrm{d}\theta \tag{41}$$

The first term and the second term represent the forward-biased and the reverse-biased cases. Integrate the equation gives

$$V_{j,dc} = \frac{\theta_{on}}{\pi}V_{bi} - V_{j0}\left(1-\frac{\theta_{on}}{\pi}\right) - \frac{V_{j1}}{\pi}\sin\theta_{on} \tag{42}$$

When the diode switches from off to on, $V_j = V_{bi}$. Then we have

$$-V_{j0} + V_{j1}\cos\theta_{on} = V_{bi} \tag{43}$$

When the diode is off, R_j is infinite. Applying Kirchoff's voltage to the other loop gives

$$-V_I + IR_S + V_j = 0 \tag{44}$$

with

$$I = \frac{dC_jV_j}{dt} \tag{45}$$

These two equations can be rewritten by

$$\frac{d\left(C_j V_j\right)}{dt} = \frac{(V_I - V_j)}{R_S} \tag{46}$$

where C_j can be expressed as a harmonic function of V_D

$$C_j = C_0 + C_1 \cos\left(\omega t - \phi\right) + C_2 \cos\left(2\omega t - 2\phi\right) + \ldots \tag{47}$$

Using above two equations yields

$$\omega R_S \left(C_1 V_{j0} - C_0 V_{j1}\right)\sin\theta = V_{j0} - V_D + \left(V_P \cos\phi - V_{j1}\right)\cos\theta - V_P \sin\phi \sin\theta \tag{48}$$

where $\theta = \omega t - \phi$. Because this equation also holds for the off period, each sinusoidal term can be collected as

$$V_{j0} = V_D \tag{49}$$

$$V_{j1} = V_P \cos\phi \tag{50}$$

$$V_P \sin\phi = \omega R_S \left(C_1 V_{j0} - C_0 V_{j1}\right) \tag{51}$$

Substituting (49) to (42) and inserting (39) into (42) obtains

$$\frac{R_S}{R_L} = \frac{V_{j1}}{V_D}\frac{1}{\pi}\sin\theta_{on} - \frac{\theta_{on}}{\pi}\left(1 + \frac{V_{bi}}{V_D}\right) \tag{52}$$

It can be shown that the phase difference ϕ can be approximated to be zero, which results in $V_P = V_{j1}$. Inserting this and (49) into (43) and (52) to obtain

$$\tan\theta_{on} - \theta_{on} = \frac{\pi R_S}{R_L\left(1 + \dfrac{V_{bi}}{V_D}\right)} \tag{53}$$

This transcendental expression allows obtaining θ_{on} iteratively, which is dependent on the diode input power that determines both V_{bi} and V_D.

The diode efficiency can be expressed as

$$\eta_D = \frac{P_{dc}}{P_L + P_{dc}} \tag{54}$$

where P_L is the power dissipated by the diode and P_{dc} is the DC output power across R_L. They are given by

$$P_L = L_{on,R_S} + L_{off,R_S} + L_{on,diode} \tag{55}$$

$$P_{dc} = \frac{{V_o}^2}{R_L} \tag{56}$$

The three terms of the diode loss P_L can be expressed by

$$L_{on,R_S} = \frac{1}{2\pi} \int_{-\theta_{on}}^{\theta_{on}} \frac{\left(V_I - V_{bi}\right)^2}{R_S} d\theta \tag{57}$$

$$L_{off,R_S} = \frac{1}{2\pi} \int_{\theta_{on}}^{2\pi-\theta_{on}} \frac{\left(V_I - V_d\right)^2}{R_S} d\theta \tag{58}$$

$$L_{on,diode} = \frac{1}{2\pi} \int_{-\theta_{on}}^{\theta_{on}} \frac{\left(V_I - V_{bi}\right)V_{bi}}{R_S} d\theta \tag{59}$$

Since it is assumed the junction resistance is infinite during the off cycle, the loss through the diode junction has been neglected. These power losses are the time-average products of the current flowing through an element and the voltage across the element. The total power dissipated on the series resistance can be solve by integrating

$$L_{R_S} = \frac{1}{2\pi R_S}\left[\int_{-\theta_{on}}^{\theta_{on}} \left(-V_D - V_{bi} + V_P \cos\theta\right)^2 d\theta + \left(\omega R_S C_j V_P\right)^2 \int_{\theta_{on}}^{2\pi-\theta_{on}} \sin^2\theta d\theta\right] \quad (60)$$

Using the RF current instead of voltage in the second integral, (58) can be rewritten as

$$L_{off,R_S} = \frac{1}{2\pi}\int_{\theta_{on}}^{2\pi-\theta_{on}} \frac{\left(V_I - V_j\right)^2}{R_S} d\theta = \frac{1}{2\pi}\int_{\theta_{on}}^{2\pi-\theta_{on}} \frac{\left(IR_S\right)^2}{R_S} d\theta \quad (61)$$

where I is the RF current flowing through the diode in reverse bias. It is assumed that no current flows through R_j in reverse bias and all of the current flowing through R_S flows through C_j. Then (45) can be expressed as

$$I = C_j \frac{dV_j}{dt} \quad (62)$$

The voltage drop across R_S is so small in the off cycle that the phase difference ϕ is set zero. Apply this in (52) to obtain $V_{j1} = V_P$. Then

$$I = C_j \frac{d}{dt}\left[-V_{j0} + V_P \cos\left(\omega t\right)\right] = -\omega C_j V_P \sin\theta \quad (63)$$

The power dissipated by the diode junction is rewritten as

$$L_{diode} = \frac{1}{2\pi R_S}\int_{-\theta_{on}}^{\theta_{on}} V_{bi}\left(-V_D - V_{bi} + V_P \cos\theta\right) d\theta \quad (64)$$

where V_P is determined, while the diode is off, by

$$V_P = \frac{V_D + V_{bi}}{\cos\theta_{on}} \quad (65)$$

Use the results from (63) and (68) and insert them into (57), we have

$$\eta_D = \frac{1}{1+A+B+C} \quad (66)$$

where

$$A = \frac{R_L}{\pi R_S}\left(1+\frac{V_{bi}}{V_D}\right)^2\left[\theta_{on}\left(1+\frac{1}{2\cos^2\theta_{on}}\right)-\frac{3}{2}\tan\theta_{on}\right] \tag{67}$$

$$B = \frac{R_S R_L C_j{}^2\omega^2}{2\pi}\left(1+\frac{V_{bi}}{V_D}\right)\left(\frac{\pi-\theta_{on}}{\cos^2\theta_{on}}+\tan\theta_{on}\right) \tag{68}$$

$$C = \frac{R_L}{\pi R_S}\left(1+\frac{V_{bi}}{V_D}\right)\frac{V_{bi}}{V_D}\left(\tan\theta_{on}-\theta_{on}\right) \tag{69}$$

with $\omega = 2\pi f$. The diode junction capacitance is given by

$$C_j = C_{j0}\sqrt{\frac{V_{bi}}{V_{bi}+\left|V_D\right|}} \tag{70}$$

where C_{jo} is the zero bias junction capacitance of the diode.

The input impedance of the diode can be decided from the current I flowing through R_S in one cycle, that is

$$I = I_0 + I_{1r}\cos(\omega t) + I_{1i}\sin(\omega t) \tag{71}$$

where I_0 is the DC component; I_{1r} and I_{1i} are the real and imaginary parts of the fundamental frequency component, respectively. These current components are

$$I_0 = \frac{1}{2\pi R_S}\left\{\int_{-\theta_{on}}^{\theta_{on}}\left(V_I - V_{bi}\right)d\theta + \int_{\theta_{on}}^{2\pi-\theta_{on}}\left(V_I - V_j\right)d\theta\right\} \tag{72}$$

$$I_{1r} = \frac{1}{\pi R_S}\left\{\int_{-\theta_{on}}^{\theta_{on}}\left(V_I - V_{bi}\right)\cos(\theta+\phi)\,d\theta + \int_{\theta_{on}}^{2\pi-\theta_{on}}\left(V_I - V_j\right)\cos(\theta+\phi)\,d\theta\right\} \tag{73}$$

$$I_{1i} = -\frac{1}{\pi R_S}\left\{\int_{-\theta_{on}}^{\theta_{on}} \left(V_I - V_{bi}\right)\sin\left(\theta+\phi\right)d\theta + \int_{\theta_{on}}^{2\pi-\theta_{on}} \left(V_I - V_j\right)\sin\left(\theta+\phi\right)d\theta\right\} \quad (74)$$

The diode input impedance at the fundamental frequency is

$$Z_D = \frac{V_P}{I_{1r} - jI_{1i}} \quad (75)$$

Assume that there is no current flow through C_j during forward bias and that all current flow through during reverse bias, the diode current in one cycle can be found by integrating

$$I_{1r} - jI_{1i} = \frac{1}{\pi R_S}\int_{-\theta_{on}}^{\theta_{on}} \left(-V_D - V_{bi} + V_P\cos\theta\right)\cos\theta d\theta + j\frac{\omega C_j V_P}{\pi}\int_{\theta_{on}}^{2\pi-\theta_{on}} \sin^2\theta d\theta \quad (76)$$

The second integral is solved similar to that in (60). Then the diode input impedance can be written as

$$Z_D = \frac{\pi R_S}{\cos\theta_{on}\left(\frac{\theta_{on}}{\cos\theta_{on}} - \sin\theta_{on}\right) + j\omega R_S C_j\left(\frac{\pi-\theta_{on}}{\cos\theta_{on}} + \sin\theta_{on}\right)} \quad (77)$$

If the reactance of the diode impedance is tuned out by using the impedance matching, the diode input impedance can be rewritten as

$$R_D = \frac{\pi R_S}{\cos\theta_{on}\left(\frac{\theta_{on}}{\cos\theta_{on}} - \sin\theta_{on}\right)} \quad (78)$$

The input resistance is a dynamic variable dependent on the input power, as the same as the diode efficiency.

7.4 High gain rectenna element design

The rectenna is comprised of two pair of pentagonal loop antennas, a detector diode in shunt, a capacitor in shunt, and a load at the end of the rectenna system. The coplanar stripline-fed pentagonal loop antennas are designed to achieve high gain and high radiation efficiency. The main role of the antenna is to receive the RF signals effectively from free space. Unlike normal rectenna designs, this rectenna element does not include a band-reject filter which is for suppression of harmonics generated from a rectifying diode, because the reflectarray just reradiate the operating frequency The RF signals passed the diode are converted into DC power. The capacitor next located to the diode works as DC pass filter. It does not only block RF signals traveling toward the resistive load, but also tune out the reactance of the diode. Finally, the proper value of the resistive load is selected to maximize output DC power. To optimize the rectenna performance, proper placement of the diode and the DC pass filter should be carefully considered.

A. Pentagonal loop antenna

The proposed antenna shown in Fig. 64 has a linearly polarized high gain characteristic which is demanded for rectenna systems. The four pentagonal loops with the same size are based on coplanar stripline feed. The antennas printed on the substrate RT/Duroid 5880 with ε_r = 2.2, and h_1 = 0.508mm. A reflecting conducing plane is placed 11.2 mm (h_2) below the substrate to achieve a higher gain by directing the beam broadside in one direction, and reduce the back-radiation.

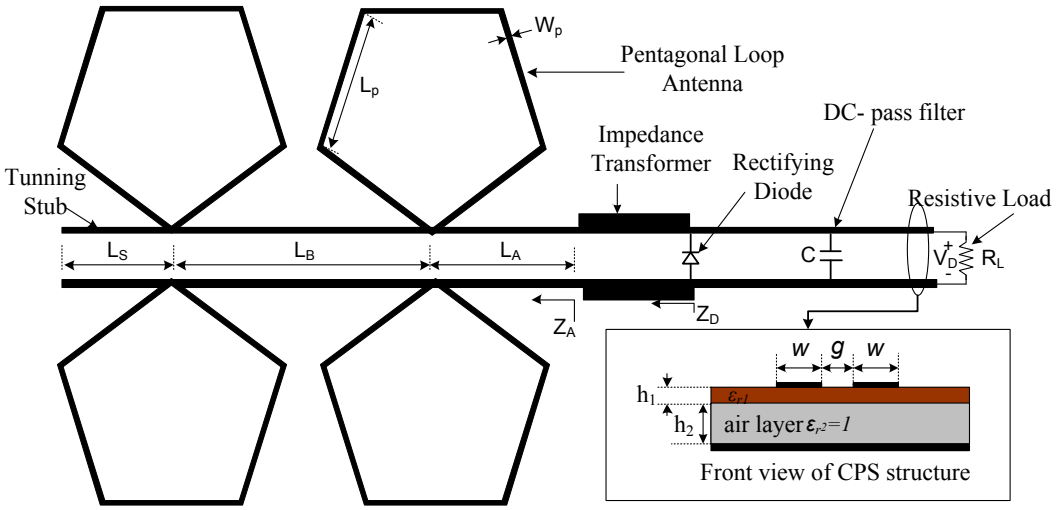

Fig. 64. Configuration of the proposed high gain rectenna with pentagonal loops

The antenna parameters are optimized for 5.8 GHz frequency operation by using the IE3D simulator, electromagnetic full-wave analysis software based on Method of Moment. The optimized dimensions are L_p = 12.7 mm, L_S = 14.76 mm, L_A = 11. 41 mm, L_B = 43. 65 mm, and W_p = 0.85 mm. With these values, the antenna achieves high gain of 13.0 dBi at 5.8 GHz. Fig. 65 and Fig. 66 show the simulated input impedance and gain of the antenna. The antenna input impedance Z_A is equal to 112 Ω. For antenna design in a rectenna system, the input impedance of the antenna should be matched with input impedance of rectifying diode circuit.

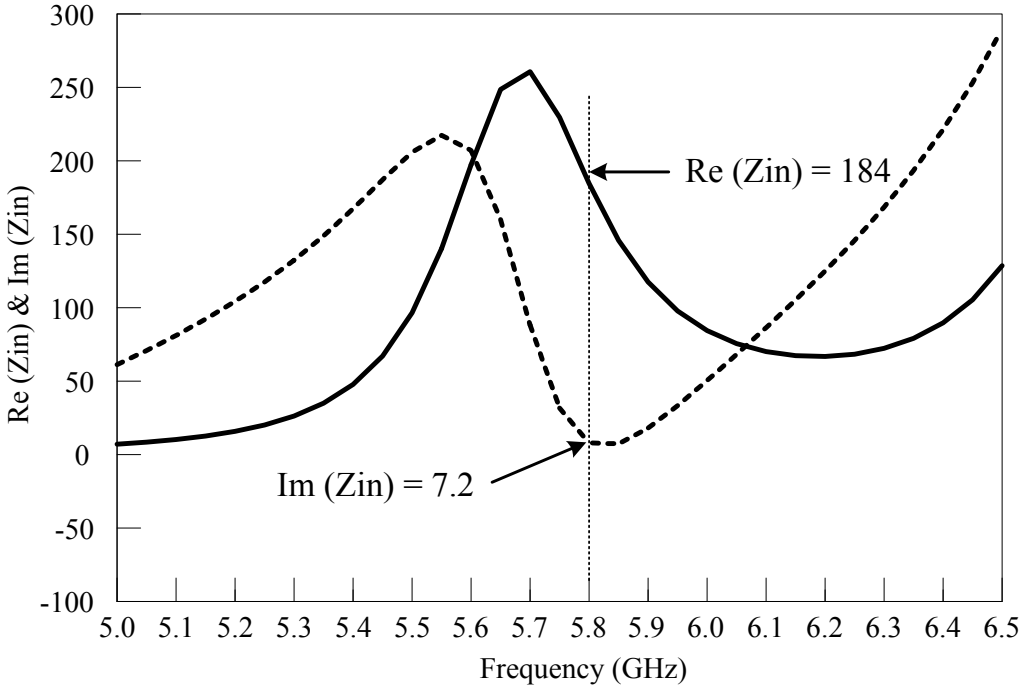

Fig. 65. Simulated input impedance of the antenna

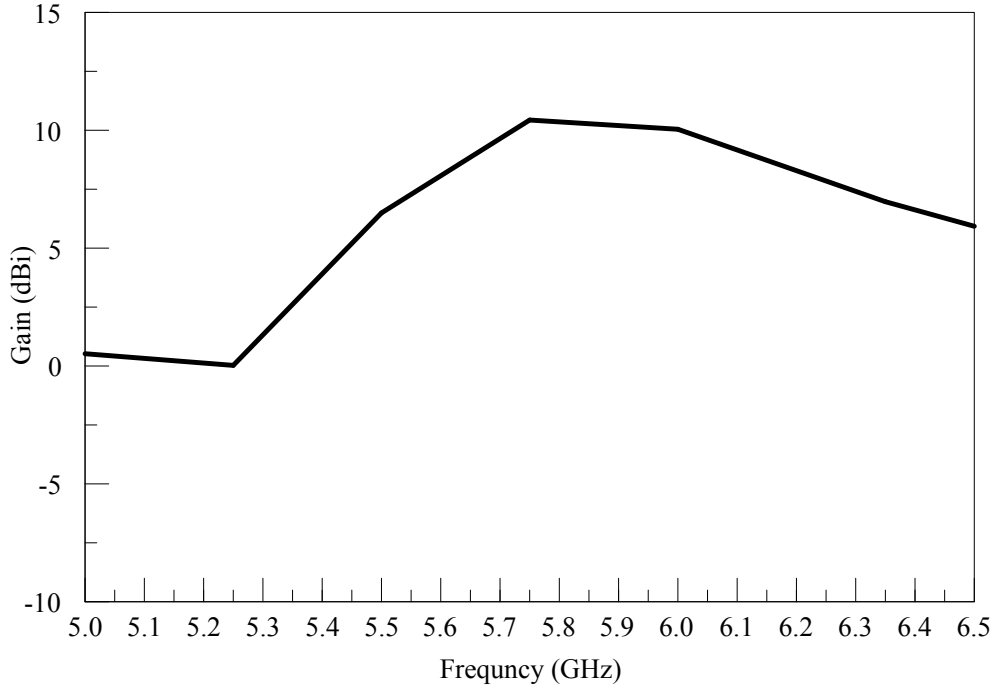

Fig. 66. Simulated antenna gain

B. Coplanar stripline structure

The proposed rectenna is based on coplanar stripline structures as shown in Fig. 64. The dimensions of the CPS in both antenna feed and the rectifying circuit are w = 0.9 mm and g = 0.4 mm. The characteristics impedance of the CPS is 184 Ω. Another CPS structure is located between the antenna and the diode as an impedance transformer. To obtain optimizing matching network, the CPS is designed with w = 1.92 mm and g = 0.4 mm for 143.5 Ω of characteristic impedance. Therefore, the input impedance Z_D before the diode becomes 184 Ω. In rectenna design, the characteristic impedance of the based transmission line is chosen to match the impedances of the antenna with the diode to reduce the signal reflections between these components.

C. Detector diode and dc pass filter

The diodes used in this dissertation are the GaAs flip chip Schottky barrier diodes (Model MA4E1317) from M/A COM. It has a series resistance R_S = 4 Ω, zero-bias junction capacitance C_{j0} = 0.02 pF, forward-bias turn-on voltage V_{bi} = 0.7 V, and breakdown voltage V_B = 7 V. The junction capacitance (C_j) of the diode, described in (70), significantly affects the diode efficiency, which is a function of the diode output voltage. Equation (70) is rewritten here for convenience

$$C_j = C_{j0}\sqrt{\frac{V_{bi}}{V_{bi}+|V_D|}} \tag{79}$$

V_D is the output self-bias voltage of the diode. Higher V_D results in a smaller junction capacitance, which also gives better conversion efficiency. The maximum efficiency occurs when C_j approaches to zero. Furthermore, the diode should operate as close to its

voltage limit as possible to minimize its reactance. This reduces the reflection of the RF power at the diode terminal and hence increases the rectenna efficiency.

A broadband DC-blocking chip capacitor by Dielectric Laboratories (Model C08BLBB1X5UX) is chosen as the DC pass filter. The DC pass filter not only tunes out the reactance of the diode but also blocks the unwanted RF signals from reaching the load resistance. The detector diode and the DC-blocking capacitor are mounted across the coplanar stripline by using silver epoxy.

D. Rectenna measurements and conversion efficiency

The free space measurement of the rectenna has been studied in [42]. The equipment setup is shown in Fig. 67. The RF-to-DC conversion efficiency of the rectenna (η) can be defined as

$$\eta = \frac{P_{DC}}{P_r} \tag{80}$$

P_{DC} is the DC output power. Friis transmission equation is used to calculate the power propagating to the CP antenna (P_r). A NARDA standard horn antenna with a 15 dB gain (G_t) is used to transmit the RF power (P_t), and the rectenna gain (G_r) is set equal to 10.1 dB. By changing the distance between the horn antenna and the rectenna, the efficiencies for different power densities are determined. The power density (P_d) is given by

$$P_d = \frac{P_t G_t}{4\pi D^2} \tag{81}$$

where D is the distance between the horn antenna and the center of the rectenna.

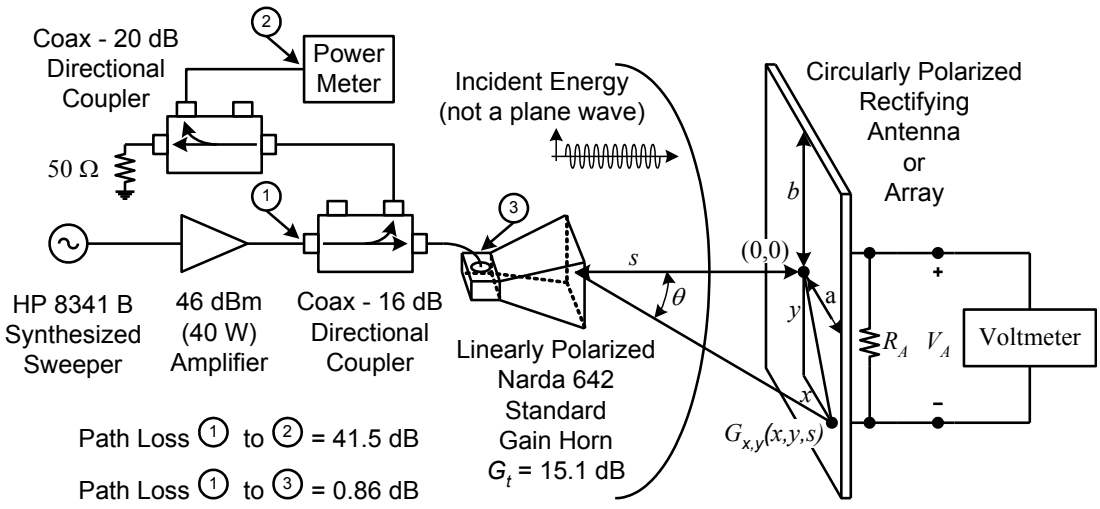

Fig. 67. Free space measurement setup of the rectenna

The conversion efficiency curves of the single high gain rectenna at 5.8 GHz are shown in Fig. 68. The best RF-to-DC conversion efficiency of the rectenna is 75 % when the load and the DC output voltage are 100 Ω and 5.4 V, respectively. It is obviously seen that the efficiency gradually decreases as the load resistance increases.

E. Summary

In this chapter, WPT system and rectenna operation theory have been reviewed. A pentagonal loop antenna has been developed at 5.8 GHz. The pentagonal loop provides linear polarization and achieves high gain of 12.5 dBi. The CPS feed line is designed with characteristic impedance of 184 Ω. An impedance transformer is used to match the antenna input impedance to the diode input impedance. The proposed rectenna achieves a maximum conversion efficiency of 75% with the resistive load of 100 Ω.

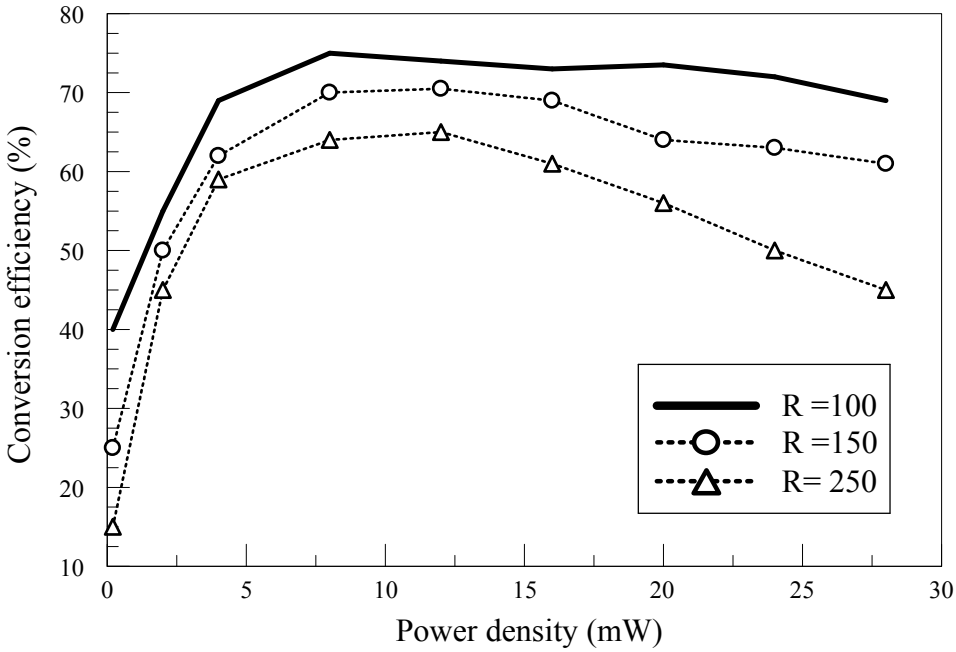

Fig. 68. Measured rectenna efficiency at 5.8 GHz

7.5 Reflectarray design

In this chapter, a compact reflectarray element is designed for a rectifying reflectarray system. The configuration of the proposed reflectarray is shown in Fig. 69. The 182 (14×13) reflectarray elements are printed on the substrate Rogers RT Duroid 5880 with thickness of 0.508 mm. The spacing form layer (ε_r = 1.06) of 3.2 mm is inserted between the substrate and the ground plane. The reflectarray and unit cell element in the close-up picture of the reflectarray elements are shown in Fig. 70. The proposed element is a combination of an inner circular patch and an outer ring with ring radius and width of R and W_r, respectively. In the element design, outer ring width W_r and gap width W_g is fixed as 1 mm and 0.5 mm, respectively. The important design parameter is radius of the outer ring R which is varied to obtain the element reflection phase variation curve.

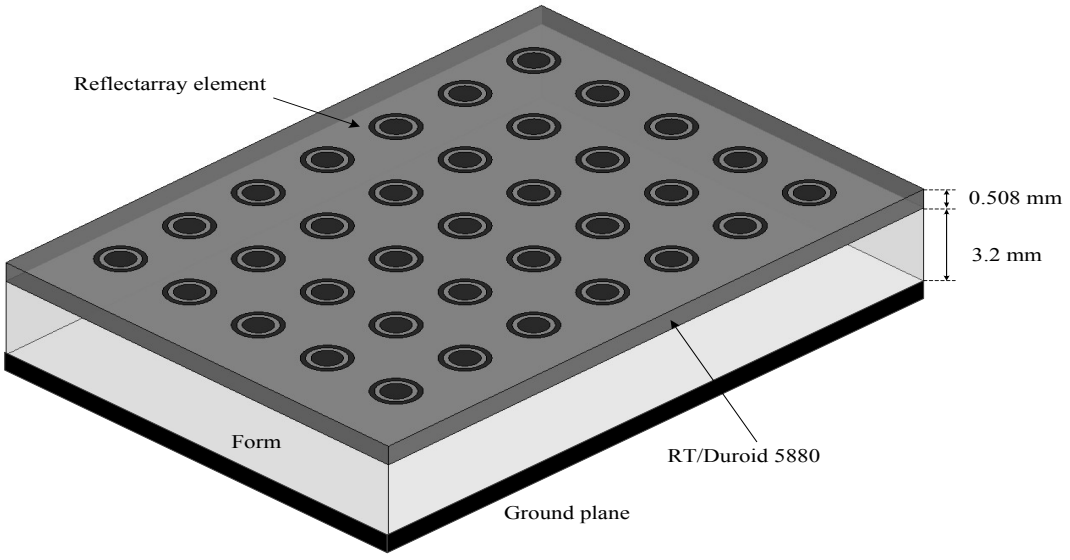

Fig. 69. Perspective view of reflectarray

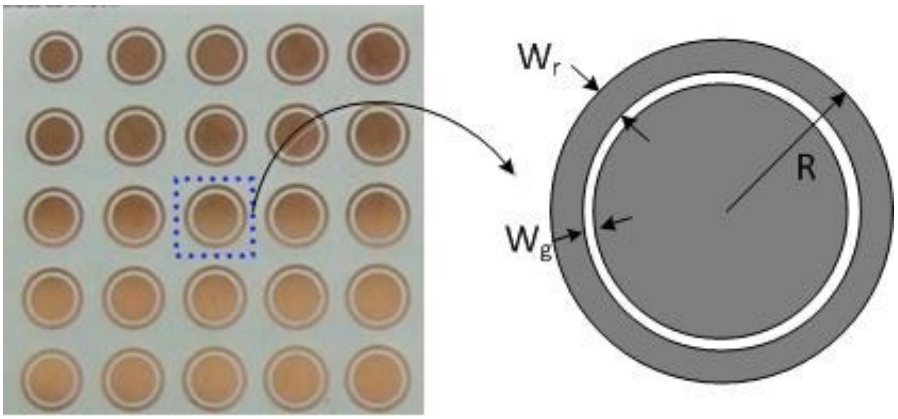

Fig. 70. Reflectarray unit cell and its pictures

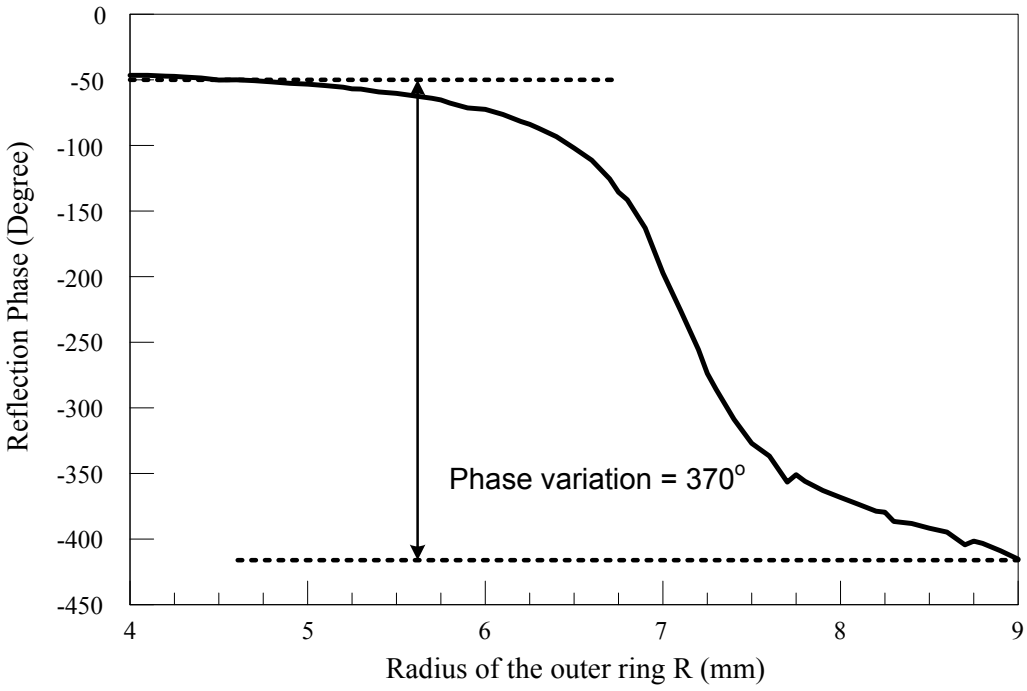

Fig. 71. Phase variation of the unit cell element

The unit cell is located in a square lattice with the size of 18 mm × 18 mm, which is 0.35 λ_0 × 0.35 λ_0 at 5.8 GHz. This compact size unit cell allows more elements to be added in the limited area, which leads to have higher gain. Fig. 71 shows the simulated reflection phases against the unit cell element by controlling the outer ring radius *R* at the operation frequency of 5.8 GHz. Neither the ring nor the circular patch alone can provide a sufficient phase variation range for a practical reflectarray design. With the proposed ring-patch combination, it is found that the compact reflectarray element provides a sufficient phase range of 370^o.

In the design of a reflectarray, it is desired to find the maximum aperture efficiency with the given design parameters. Fig. 72 shows the aperture efficiency versus the ratio of the feed height *F* to reflectarray diameter *D*. In this study, the offset angle θ_0 is set at 25^o to prevent the blockage of the incident wave from the rectenna structure. As F/D grows, the maximum aperture efficiency appears at the higher q factor value. For example, if the gain of the feed antenna is set 10 dBi, which means the q factor value is about 2, from the graph, the aperture efficiency of the reflectarray is expected as 60 % with F/D of 0.6. Fig. 72 shows efficiencies versus *q* value with F/D of 0.6. It is seen from the results that as the value q increase, the spillover efficiency increases and the illumination efficiency decreases in Fig. 73. The aperture efficiency reaches a maximum when *q* is equal to 0.66 in this study.

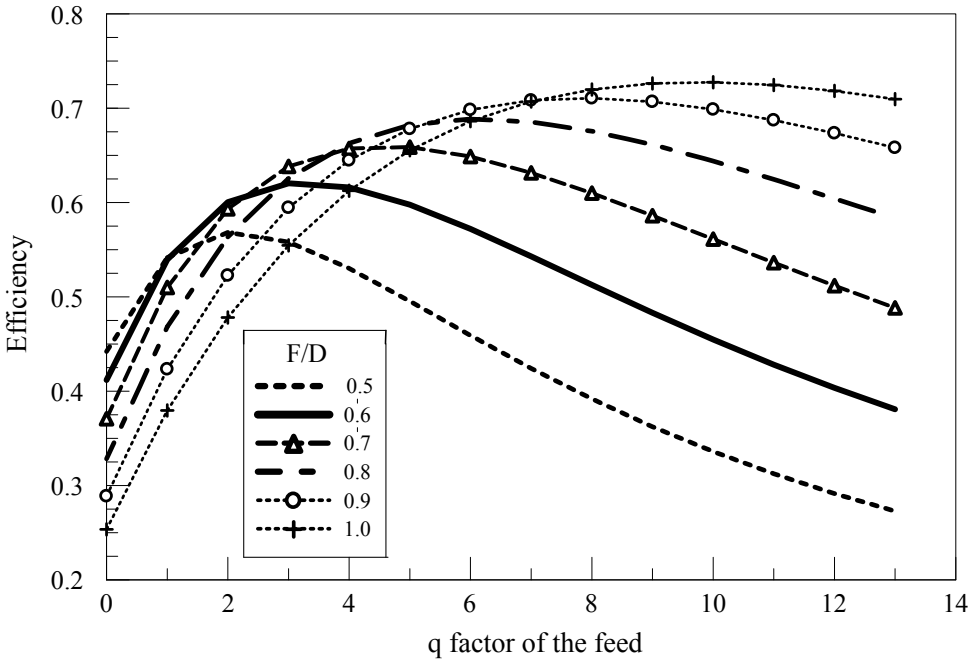

Fig. 72. Aperture efficiency vs. F/D

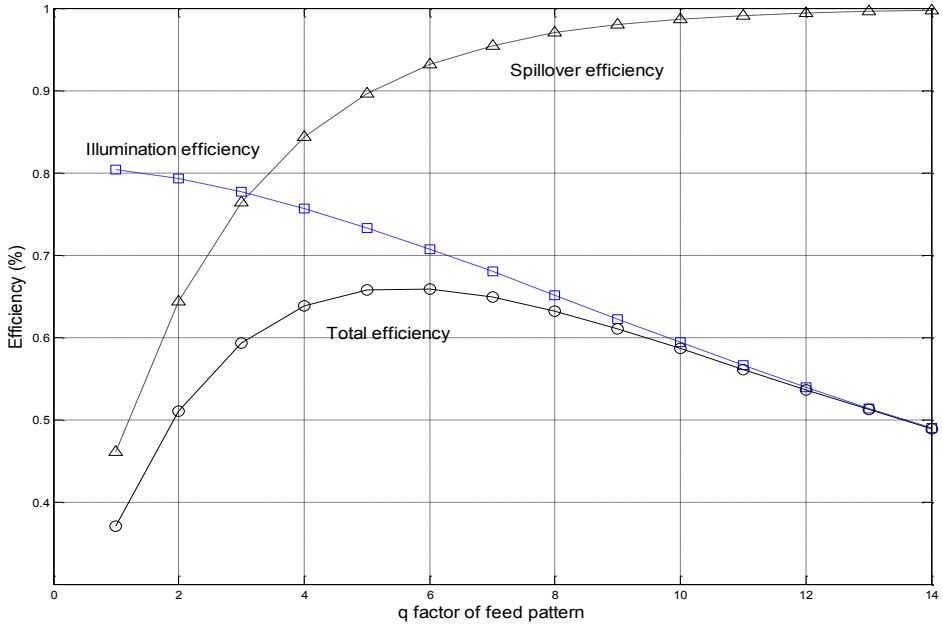

Fig. 73. Efficiency vs. F/D

7.6 Combining reflectarray and rectenna

A novel rectenna array using a reflectarray which is called “rectifying reflectarray” here is presented in this chapter. The difference from the conventional reflectarrays is that the feed antenna of a reflectarray is replaced with a rectifying antenna to generate DC energy. The rectenna with high gain property in previous chapter and the reflectarray proposed with compact unit cell in this chapter are combined into a novel rectifying reflectarray. This rectifying reflectarray can illuminate complicated feed network from rectenna arrays with same aperture sizes.

Fig. 74 shows the feed antenna designed to measure the gain of the reflectarray. The antenna component is the same with the antenna in the high gain rectenna circuits except the connected balun, instead of a rectifying circuit. The foam layer inserted between substrate and ground plane is not filled by foam, but is supported by four plastic screws, which make thickness of the layer controllable. The measured radiation patterns of the feed antenna are shown in Fig. 75. Maximum gain of the antenna in elevation plane is 12.5 dBi.

The reflectarray is measured with the pentagonal loop antenna located at focal point as shown in Fig. 76. In the reflectarray design, q factor is 2 for the feed gain of 13 dBi and F/D is set by 0.6. So, almost 60 % maximum aperture efficiency is expected from the reflectarray theory. To avoid incident field blockage, the reflectarray has the offset feed with $\theta_0 = 25^{o}$.

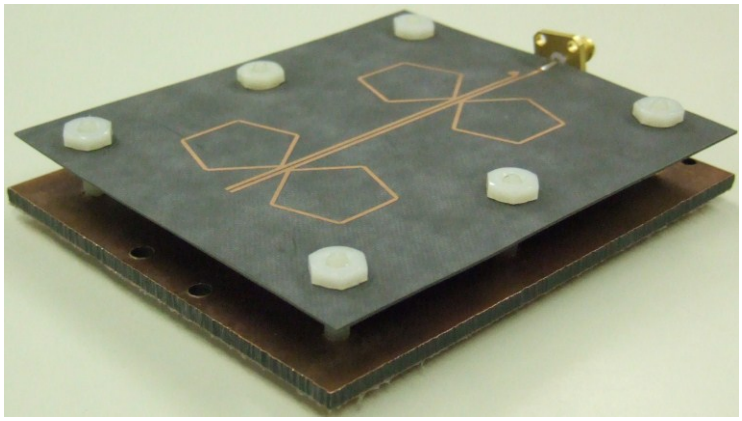

(a)

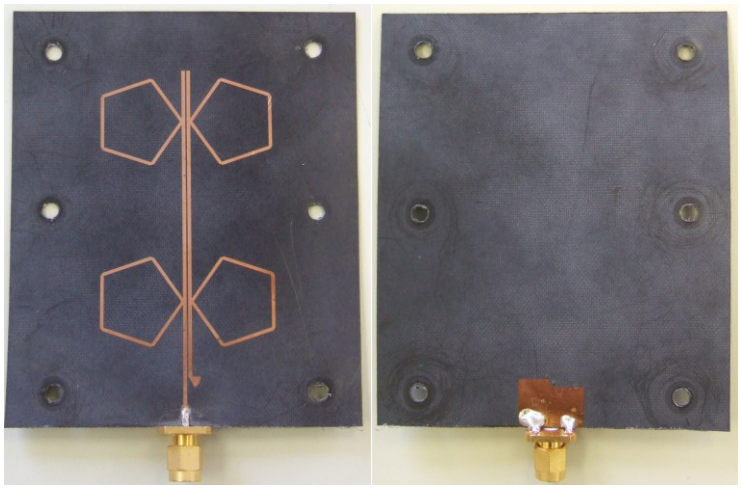

(b) (c)

Fig. 74. Feed antenna to verify the gain: (a) perspective view, (b) top surface, and (c) bottom surface

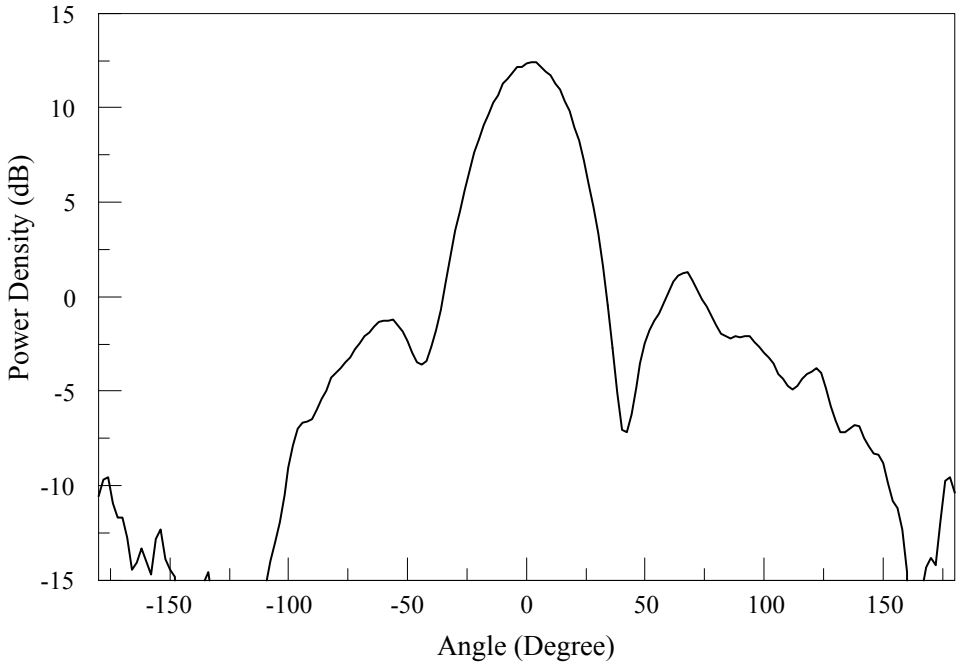

Fig. 75. Measured radiation patterns of the feed antenna in azimuth plane

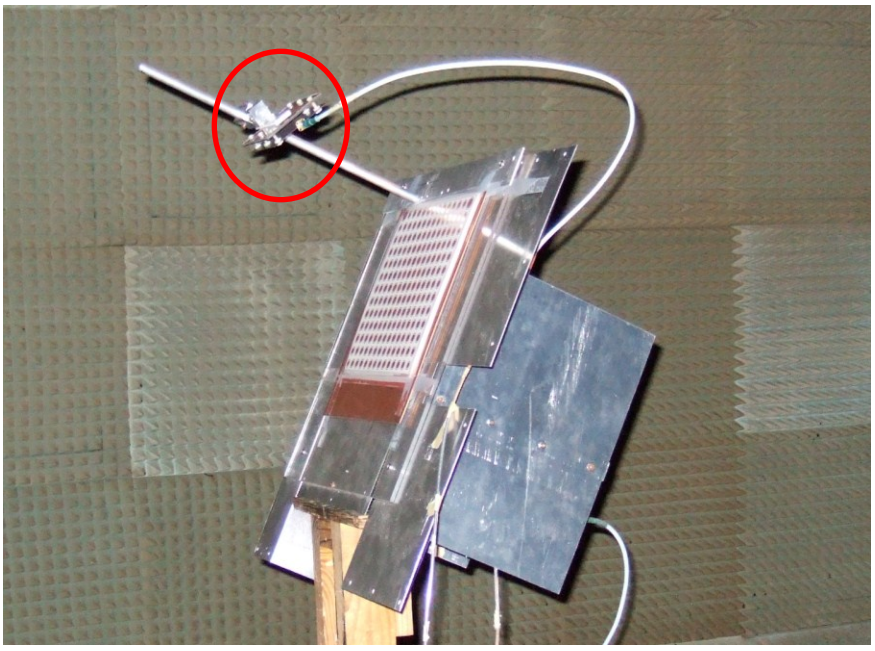

Fig. 76. Reflectarray with the feed antenna

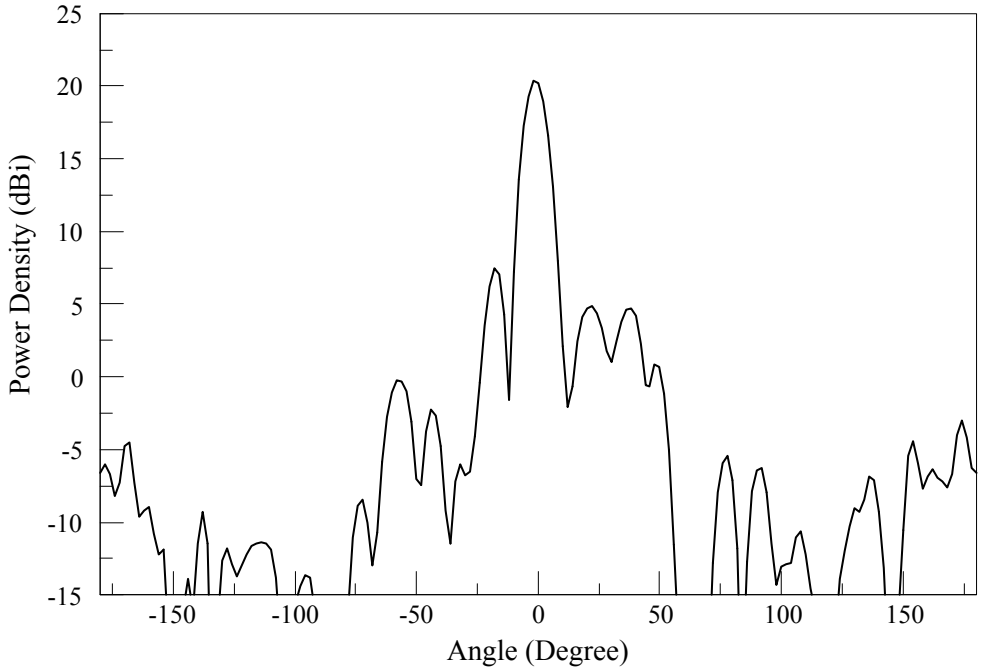

Fig. 77. Measured radiation pattern of the reflectarray at 5.8 GHz

The measured radiation pattern of the reflectarray at 5.8 GHz is shown in Fig. 77. The main beam is at boresight and the 3 dB beam width is about 11°. The peak side lobe level relative to the main beam is 16.2 dB. The maximum gain of the reflectarray is 21.5 dBi, which is expected value from the reflectarray space configuration information.

The measured conversion efficiency curves of the rectifying reflectarray are shown in Fig. 78. Like the single antenna case, the reflectarray rectenna achieves the maximum conversion efficiency of 71° when the resistive load is 100 Ω. The conversion efficiency of 150 Ω load shows similar efficiency results with the 100 Ω case. As the load resistance value increase, the efficiency gradually decreases.

7.7 Summary

Basic operation theory of the reflectarray is reviewed. Several efficiency terms are proposed, analyzed and derived to obtain the aperture efficiency of the reflectarray. Based on the design theory, a reflectarray with compact unit cell elements has been developed. The antenna component is measured with a balun and achieves 12.5 dBi maximum gain. The reflectarray is measured with the feed antenna to check the gain of the reflectarray. The maximum gain is 21.4 dBi. The proposed rectifying reflectarray with the rectenna located at the focal point is measured with several load resisters and achieved 71 % maximum conversion efficiency.

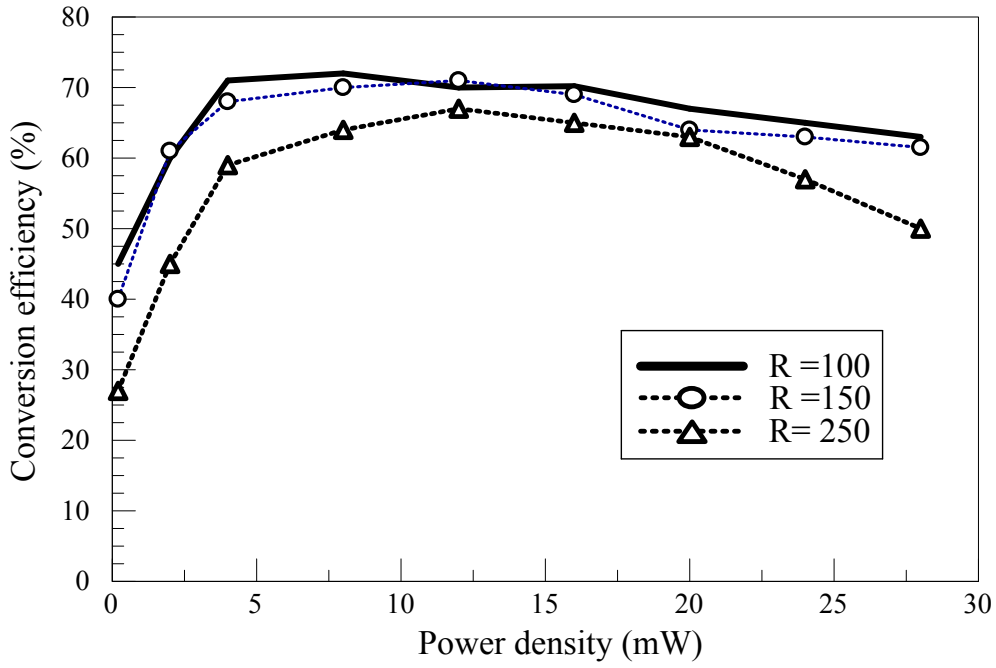

Fig. 78. Measured conversion efficiency of the rectifying reflectarray

CHAPTER VIII

MICROWAVE APPLICATION: SPIRAL ANTENNA FED BY DSPSL

8.1 Introduction

The most important advantage of circularly polarized (CP) antenna is: no need for precise alignment between transmit and receive antennas, resulting in better immunity over multipath fading environment. Spiral antennas have been a popular choice for wideband radiating systems in communication and other systems because of wide band CP characteristics [57]. Since the spiral antenna is a balance structure, its feed structure needs a balun to transform unbalanced line (microstrip line or coplanar waveguide) into balanced line. Although the spiral antenna itself is a very wideband component, the whole antenna performance could be degraded due to the limits of balun [58]. In this chapter, an electromagnetic coupled balun formed microstrip line to Double Sided Parallel Strip Line (DSPSL) is proposed to feed an Archimedean spiral antenna.

8.2 Introduction to Double Sided Parallel Strip Line

Double Sided Parallel Strip Line (DSPSL) has been analyzed first by Wheeler using conformal transformation mapping method. The analyses show the closed-form equations derived for symmetrical DSPSL separated by an air [59] and a dielectric layer [60]. However, by comparing with conventional microstrip lines, the characteristics of the symmetrical DSPSL can be found with less complexity using the symmetry. Fig. 79 shows the configurations and their electric field distribution of the DSPSL (a) and the

conventional microstrip line (b). The horizontal electric fields of symmetry in Fig. 79 (a) generates zero potential plane located at Z = h/2 since the two conductors on top and bottom are identical in magnitude and opposite in phase by image theory. A zero potential plane can be considered as a virtual ground plane, which relates the symmetrical DSPSL to the conventional microstrip lines. In Fig. 79, the conductor width of the DSPSL and the microstrip is the same as W. The substrate height of the DSPSL, and the microstrip line is 2h and h, respectively.

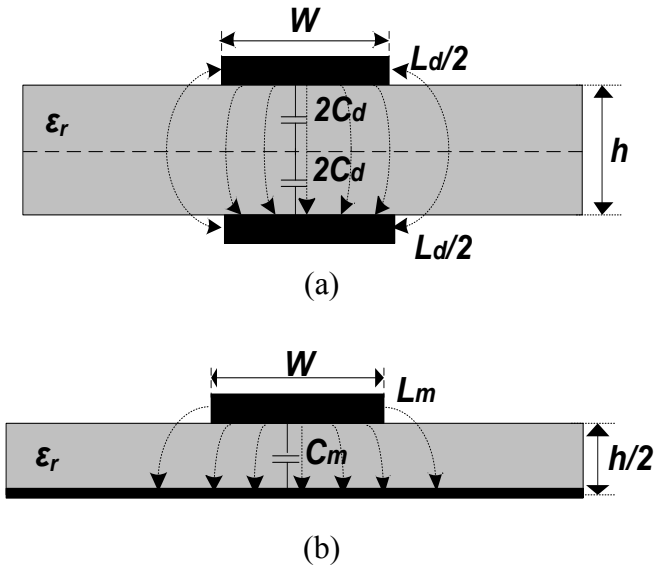

Fig. 79. Configurations of (a) symmetrical double-sided parallel-strip line and (b) conventional microstrip line

According to the image theory, it can be seen that the inductance per unit length of the DSPSL L_d is twice of that of the microstrip line L_m, and the capacitance per unit length of the DSPSL C_d is one half of that of the microstrip line C_m. Therefore, the characteristic impedance of the two cases can be given by

$$Z_{cd} = \sqrt{\frac{L_d}{C_d}} = \sqrt{\frac{2L_m}{C_m / 2}} = 2\sqrt{\frac{L_m}{C_m}} = 2Z_{cm} \tag{82}$$

where Z_{cd} and Z_{cm} is the characteristic impedance of the DSPSL and microstrip line, respectively. The equation (82) shows that characteristic impedance of the symmetrical DSPSL in Fig. 79.(a) is twice of that of the microstrip line in Fig. 79.(b). The characteristic impedance of the symmetrical DSPSL with the substrate height of h can also be expressed by the microstrip line's equations as

$$Z_c = 120(\varepsilon_{eff1})^{-1/2} \ln\left(\frac{4h}{w} + \frac{0.5w}{h}\right)[\Omega] \qquad for\ \frac{w}{h} \le 2 \tag{83}$$

$$Z_c = \frac{240\pi\left(\varepsilon_{eff2}\right)^{-1/2}}{\left(2w/h\right) + 1.393 + 0.667\ln(1.444 + 2w/h)}[\Omega] \quad for\ \frac{w}{h} \ge 2 \tag{84}$$

$$\varepsilon_{eff1} = \frac{(\varepsilon_r + 1)}{2} + \frac{(\varepsilon_r - 1)\left\{\frac{1}{\sqrt{1 + 6\frac{h}{w}}} + (1 - 2\frac{w}{h})^2\right\}}{2} \tag{85}$$

$$\varepsilon_{eff2} = \frac{(\varepsilon_r + 1)}{2} + \frac{(\varepsilon_r - 1)\frac{1}{\sqrt{1 + 6\frac{h}{w}}}}{2} \tag{86}$$

where ε_{eff1} and ε_{eff2} are the effective permittivity for each cases and ε_r is the relative permittivity of the substrate height $h/2$. The equations(83), (84) may be useful for the DSPSL design due to the lack of calculating commercial tools for characteristic impedance of the symmetrical DSPSL. In comparison with the microstrip line of the

same height, the DSPSL has wider stripline with the same characteristic impedance and shorter wavelength with the same stripline width.

8.3 Spiral design

A two-arm Archimedean spiral antenna is designed to illustrate the DSPSL feed design. Fig. 80 shows the geometry of the Archimedean spiral antenna for simulation. Each arm of an Archimedean spiral is linearly proportional to the angle ϕ, and the edge of each arm can be defined by the following equations [61].

$$r_1 = r_0\phi + b_1 \text{ and } r_2 = r_0\phi + b_2 \tag{87}$$

$$r_3 = r_0(\phi - \pi) \text{ and } r_3 = r_0(\phi - \pi) + b_2 \tag{88}$$

where *r1* and *r3* is the inner radius of the spiral arms, and *r2* and *r4* is the outer radius of the spiral arms. The width of the arm, *w* is given by $b_2 - b_1$.

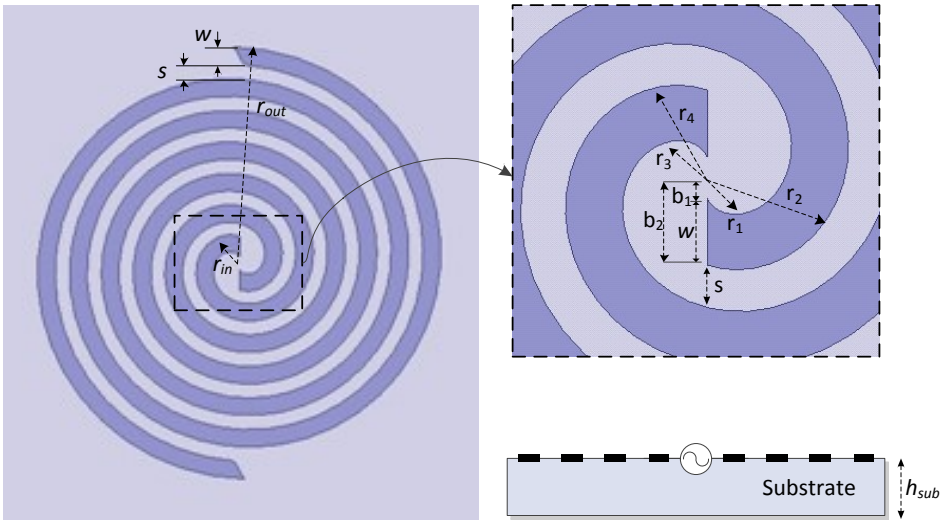

Fig. 80. Geometry of the two-arm spiral antenna

The Archimedean spiral antenna radiates from an active region where the circumference of the spiral equals one wavelength, and the currents on the adjacent transmission line are approximately in-phase [61] . The lowest and highest operating frequencies are determined by the outer and inner radius, respectively.

$$f_{low} = \frac{c}{2\pi r_{out}}, \quad f_{high} = \frac{c}{2\pi r_{in}} \tag{89}$$

Fig. 81 shows the simulated results for a design with the inner radii $r_1 = r_3 = 0.67mm$, the outer radius $r_{out} = 22mm$, the distance between the neighbor arms $s = 1.4mm$, and the arm width $w = 2.23mm$ using an RT/Duroid 5870 substrate with $\varepsilon_r = 2.33$ and $h_{sub} = 0.7874mm$. Quasi-frequency independent behavior is shown from 2.3GHz to 20GHz. The impedance is increasing gradually because the lumped port used in simulation is considerably larger than the highest frequency. The reactance across this bandwidth is zero.

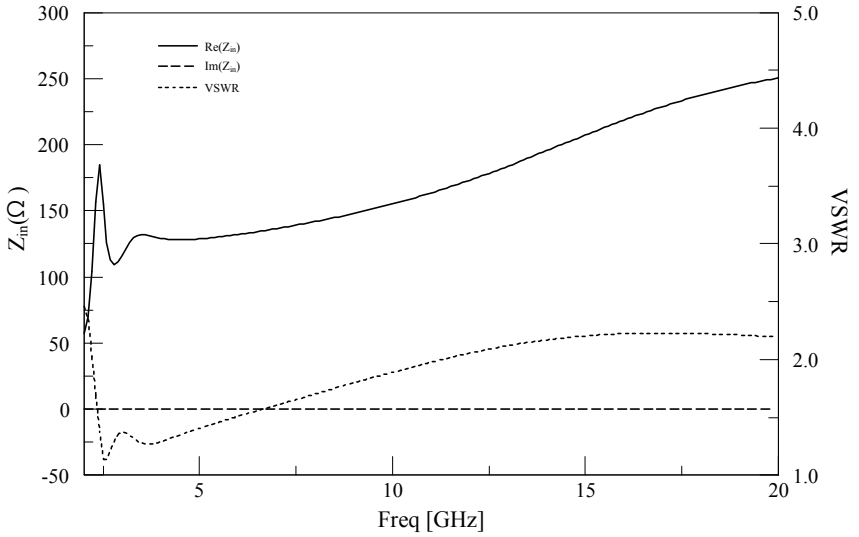

Fig. 81. Simulated input impedance and VSRW of the lumped-fed spiral antenna

8.4 Microstrip line to DSPSL transition design

The spiral antenna exhibits broadband behavior with high efficiency, but it is difficult to feed these antennas without degrading these performances. Several ways to feed spiral antennas have been developed to preserve the radiation and impedance bandwidths, while adapting the antennas to specific applications. [58, 62-67]. One of the DSPSL characteristics is a broadband bandwidth, which is appropriate to feed spiral antennas.

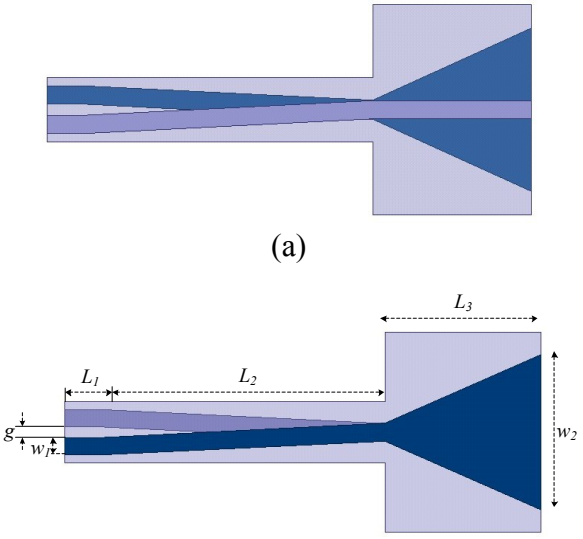

Fig. 82. DSPSL feed structure: (a) top view, (b) bottom view

Fig. 82 illustrates the geometry of the DSPSL feed for an Archimedean spiral antenna using same substrate with the spiral antenna, RT/Duroid 5870. This is synthesized by transforming the input impedance Z_1 of the spiral antenna into the measurement system's impedance $Z_0 = 50\Omega$. The DSPSL is designed with the line width w_1 = 2.23mm (same with the arm width of the spiral), the horizontal distance between

upper line and lower line g = 1.35mm, the DSPSL section length L_1 = 5mm, the intermediate section L_2 = 36mm, the microstrip line section L_3 = 20mm, and the ground width w_2 = 20mm. Fig. 83 shows the prospective view of the spiral antenna fed by DSPSL. Each arm of the spiral antenna is attached to the strip line with same width.

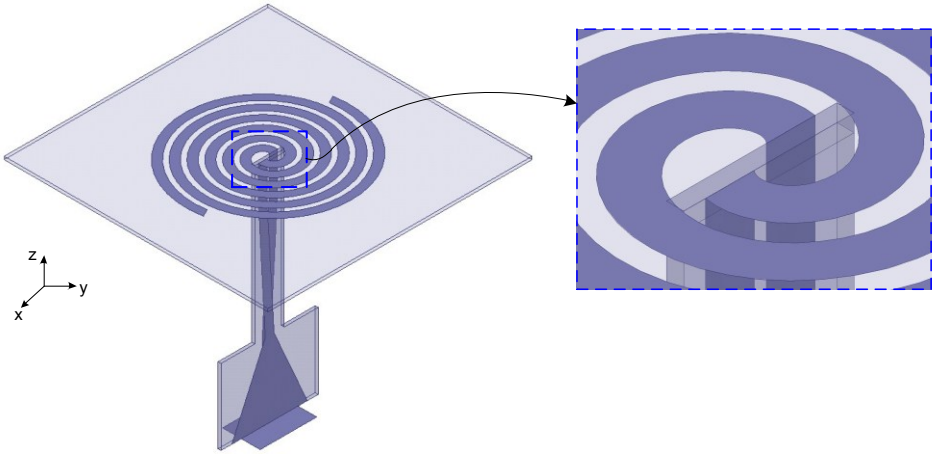

Fig. 83. Geometry of whole spiral antenna

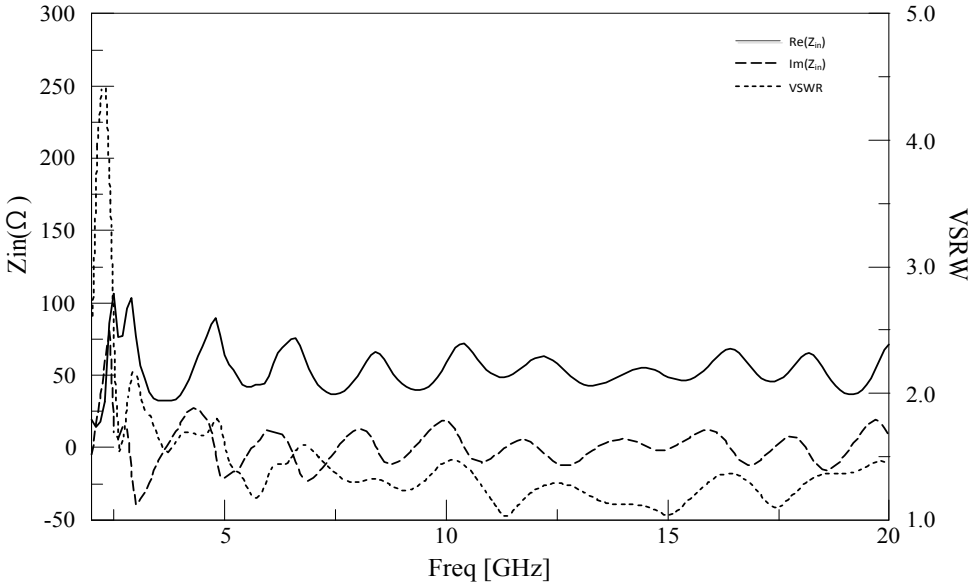

Fig. 84.Simulation result of whole spiral antenna

Fig. 84 shows the simulated results for the DSPSL-fed spiral antenna. The VSWR remains below 2.0 across the bandwidth from 2.5GHz to 20GHz.

8.5 Fabricated antenna and measurement result

Fig. 85 shows the fabricated spiral antenna and DSPSL feed structure. The center of spiral antenna is cut a slot, and the arms are soldered onto the DSPSL lines. Fig. 86 shows the VSWR of the measured and simulated the spiral antenna. The VSWR remains below 2 over the whole range, and these results are in good agreement until 17GHz. The disagreement in higher frequencies comes from an inaccuracy of cutting or soldering.

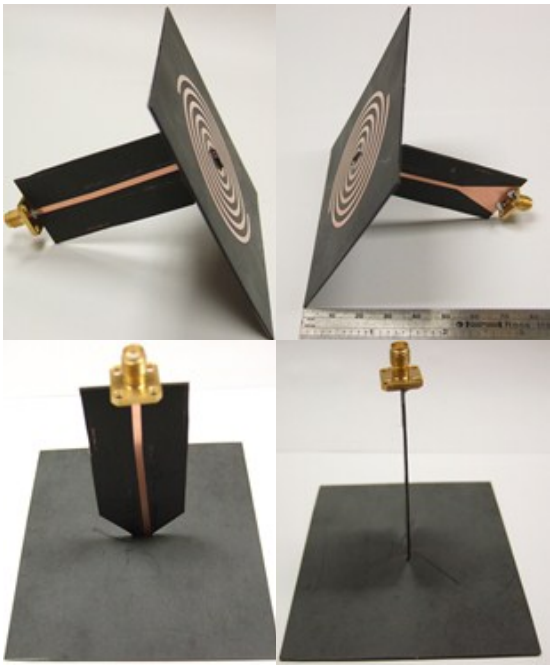

Fig. 85. Fabricated DSPSL-fed antenna

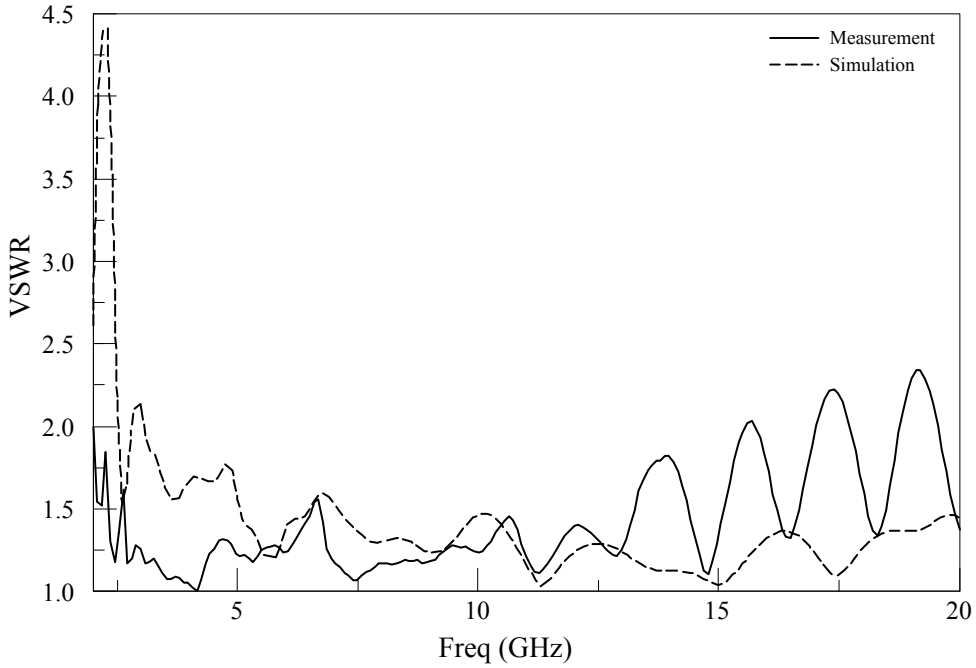

Fig. 86. VSWR of the measured and simulated DSPSL-fed spiral antenna

8.6 Conclusions

The design of a DSPSL-fed two arm Archimedean antenna has been proposed, fabricated, and measured. A wideband DSPS line transforms one arm of the spiral antenna into the stripline feed network, and transforms impedance. Measured and simulated results show wideband behavior and good agreement.

CHAPTER IX

SUMMARY AND CONCLUSIONS

9.1 Summary

As an alternative of a traditional parabolic reflector, the microstrip reflectarray has recently being investigated for high-gain applications because of low profile, light weight, and small masses. However, the microstrip reflectarray suffers from narrow bandwidth caused by its inherit distinct and differential spatial phase delay. To improve the bandwidth, wideband elements have been developed, but their structures are complicated and need multi-layers.

In this dissertation, several developments have been carried out to overcome this narrow bandwidth in simple structures. The reflectarrays using large phase range elements have been developed. A microstrip ring and slot element achieved large phase variation range about 700º on a single layer, and modified to have a linear phase responses which results in improving the bandwidth. The single layer reflectarray using coupled elements which are composed of split rings with strip lines have been developed and showed a wide bandwidth of 19%. Particle Swarm Optimization technique was used to obtain the proper phase distribution for each element over a given frequency band. The prototype reflectarray adjusted by PSO routine have shown the wide band characteristics and gain stability in a given frequency band.

As a different type of solution for the narrow bandwidth, a six-band reflectarray has been developed on two layers. Each three different frequency band elements are located

on each layer. The capabilities of phase variation range of each element and the coupling among elements have been investigated.

A new application of the reflectarray, the rectifying reflectarray, was presented in the last chapter. The rectifying reflectarray was composed of a reflectarray which focuses RF energy to the focal point and a rectenna located at the focal point which generates DC power. This configuration removed complicated rectenna array and showed conversion efficiency of 71%.

Lastly, a DSPSL-fed Archimedean spiral antenna has been developed. Using wide bandwidth characteristics of Double Sided Parallel Strip Line, the spiral antenna shows wide bandwidth from 2.5GHz to 20GHz.

9.2 Recommendations for future research

The beam shaping of reflectarrays can be achieved by adjusting the phase of the reflection coefficient at each element on the array surface. A Particle Swarm Optimization can be used to obtain the required phase distribution on the reflectarray surface which generates the shaped beam pattern.

A coupled element composed of a split ring and a stripline presented in Chapter IV can control the resonant frequency with the radius of the split ring and the reflected phase with the line length. By adding varactors in the split ring and diodes in the stripline, the element can have the capabilities of the phase shifting and the frequency shifting.

REFERENCES

[1] D. Berry, R. Malech, and W. Kennedy, "The Reflectarray Antenna," *IEEE Trans. Antennas Propag.,* vol. 11, pp. 645-651, Nov. 1963.

[2] D. M. Pozar, "Bandwidth of Reflectarrays," *Electron. Lett.,* vol. 39, pp. 1490-1491, Oct. 2003.

[3] J. Huang, "Bandwidth Study of Microstrip Reflectarray and a Novel Phased Reflectarray Concept," in *Antennas and Propagation Society International Symposium, AP-S. Digest*, 1995, pp. 582-585.

[4] C. Han, C. Rodenbeck, J. Huang, and C. Kai, "A C/Ka Dual Frequency Dual Layer Circularly Polarized Reflectarray Antenna with Microstrip Ring Elements," *IEEE Trans. Antennas Propag.,* vol. 52, pp. 2871-2876, Nov. 2004.

[5] Y. Fan, K. Yanghyo, Y. Ang, J. Huang, and A. Elsherbeni, "A Single Layer Reflectarray Antenna for C/X/Ka Bands Applications," in *ICEAA 2007 International Conference on Electromagnetics in Advanced Applications*, 2007, pp. 1058-1061.

[6] A. Yu, F. Yang, A. Z. Elsherbeni, and J. Huang, "Experimental Demonstration of a Single Layer Tri-Band Circularly Polarized Reflectarray," in *Antennas and Propagation Society International Symposium (APSURSI)*, 2010, pp. 1-4.

[7] E. Carrasco, M. Barba, and J. A. Encinar, "Reflectarray Element Based on Aperture-Coupled Patches with Slots and Lines of Variable Length," *IEEE Trans. Antennas Propag.,* vol. 55, pp. 820-825, Mar. 2007.

[8] M. R. Chaharmir, J. Shaker, N. Gagnon, and D. Lee, "Design of Broadband, Single Layer Dual-Band Large Reflectarray Using Multi Open Loop Elements," *IEEE Trans. Antennas Propag.,* vol. 58, pp. 2875-2883, Sept. 2010.

[9] J. A. Encinar and J. A. Zornoza, "Broadband Design of Three-Layer Printed Reflectarrays," *IEEE Trans. Antennas Propag.,* vol. 51, pp. 1662-1664, July 2003.

[10] W. C. Brown, "Electronic and Mechanical Improvement of the Receiving Terminal of a Free-Space Microwave Power Transmission System," Raytheon Company NASA Contractor Report 135194, 1997.

[11] P. E. Glaser, "Power from the Sun: Its Future," *Science,* vol. 162, pp. 857-861, 1968.

[12] P. E. Glaser, "Method and Apparatus for Converting Solar Radiation to Electrical Power," United States Patent, no. 3781647, Dec. 1973.

[13] R. M. Dickinson and W. C. Brown, "Radiated Microwave Power Transmission System Efficiency Measurements," Jet Propulsion Laboratory, Cal. Tech.,March 15, 1975.

[14] J. Huang and J. A. Encinar, *Reflectarray Antennas*. Hoboken, New Jersey: Wiley-IEEE Press, 2007.

[15] C. A. Balanis, *Antenna Theory : Analysis and Design*. Hoboken, New Jersey: Wiley-Interscience, 2005.

[16] HFSS™ V13.0, 3D Full-wave Electromagnetic Field Simulation, Ansoft, Inc., [Online]. Available at. http://www.ansoft.com/products/hf/hfss

[17] R. Marin, "Investigations on Liquid Crystal Reconfigurable Unit Cells for Mm-Wave Reflectarrays," Ph.D. dissertation, Darmstadter Univ. of Technology, Darmstadter, Germany, 2008.

[18] S. D. Targonski and D. M. Pozar, "Analysis and Design of a Microstrip Reflectarray Using Patches of Variable Size," in *Antennas and Propagation Society International Symposium, AP-S. Digest*, 1994, pp. 1820-1823.

[19] A. Yu, F. Yang, A. Z. Elsherbeni, J. Huang, and Y. Rahmat-Samii, "Aperture Efficiency Analysis of Reflectarray Antennas," *Microwave and Optical Technology Letters,* vol. 52, pp. 364-372, Feb. 2010.

[20] D. M. Pozar, S. D. Targonski, and H. Syrigos, "Design of Millimeter Wave Microstrip Reflectarrays," *IEEE Trans. Antennas Propag.,* vol. 45, pp. 287-296, Feb. 1997.

[21] B. Strassner, C. Han, and C. Kai, "Circularly Polarized Reflectarray with Microstrip Ring Elements Having Variable Rotation Angles," *IEEE Trans. Antennas Propag.,* vol. 52, pp. 1122-1125, Apr. 2004.

[22] D. Pozar and T. Metzler, "Analysis of a Reflectarray Antenna Using Microstrip Patches of Variable Size," *Electron. Lett.,* vol. 29, pp. 657-658, Apr. 1993.

[23] J. Huang and R. J. Pogorzelski, "A Ka-Band Microstrip Reflectarray with Elements Having Variable Rotation Angles," *IEEE Trans. Antennas Propag.,* vol. 46, pp. 650-656, May 1998.

[24] J. A. Encinar, "Design of Two-Layer Printed Reflectarrays Using Patches of Variable Size," *IEEE Trans. Antennas Propag.,* vol. 49, pp. 1403-1410, Oct. 2001.

[25] N. Misran, R. Cahill, and V. Fusco, "Reflection Phase Response of Microstrip Stacked Ring Elements," *Electron. Lett.,* vol. 38, pp. 356-357, Apr. 2002.

[26] F. C. E. Tsai and M. E. Bialkowski, "Designing a 161-Element Ku-Band Microstrip Reflectarray of Variable Size Patches Using an Equivalent Unit Cell

Waveguide Approach," *IEEE Trans. Antennas Propag.,* vol. 51, pp. 2953-2962, Oct. 2003.

[27] Rt/Duroid 5870/5880 Data Sheet, Rogers Copporation, [Online]. Available at: http://www.rogerscorp.com/documents/606/acm/RT-Duroid-5870-5880-Data-Sheet.aspx

[28] L. Qin-Yi, J. Yong-Chang, and Z. Gang, "A Novel Microstrip Rectangular-Patch/Ring- Combination Reflectarray Element and Its Application," *IEEE Antennas Wireless Propag. Lett.,* vol. 8, pp. 1119-1122, 2009.

[29] E. Carrasco, M. Barba, and J. A. Encinar, "Aperture-Coupled Reflectarray Element with Wide Range of Phase Delay," *Electron. Lett.,* vol. 42, pp. 667-668, Jun. 2006.

[30] C. Kai, *Microwave Ring Circuits and Antennas*: Wiley-Interscience, 1996.

[31] J. Kennedy and R. Eberhart, "Particle Swarm Optimization," in *IEEE International Conference on Neural Networks*, 1995, pp. 1942-1948.

[32] Y. Rahmat-Samii, "Genetic Algorithm (Ga) and Particle Swarm Optimization (Pso) in Engineering Electromagnetics," in *17th International Conference on Applied Electromagnetics and Communications*, 2003, pp. 1-5.

[33] J. Robinson and Y. Rahmat-Samii, "Particle Swarm Optimization in Electromagnetics," *IEEE Trans. Antennas Propag.,* vol. 52, pp. 397-407, Feb. 2004.

[34] C. B. Smith, "Wideband Dual-Linear Polarized Microstrip Patch Antenna," M.S. thesis, Electrical Engineering, Texas A&M University, College Station, 2008.

[35] E. S. Gopi, "Algorithm Collections for Digital Signal Processing Applications Using Matlab," 1st edition: Springer, 2007.

[36] W. C. Brown, "The History of Power Transmission by Radio Waves," *IEEE Trans. Microw. Theory Tech.,* vol. 32, pp. 1230-1242, Sept. 1984.

[37] J. O. McSpadden and J. C. Mankins, "Space Solar Power Programs and Microwave Wireless Power Transmission Technology," *Microwave Magazine, IEEE,* vol. 3, pp. 46-57, Dec. 2002.

[38] B. H. Strassner and K. Chang, "Microwave Power Transmission," in *Encyclopedia of Rf and Microwave Engineering*. vol. 4, Hoboken, NJ: Wiley, 2005, pp. 2906-2919.

[39] S. Young-Ho and C. Kai, "A High-Efficiency Dual-Frequency Rectenna for 2.45- and 5.8-Ghz Wireless Power Transmission," *IEEE Trans. Microw. Theory Tech.,* vol. 50, pp. 1784-1789, July 2002.

[40] B. Strassner and C. Kai, "5.8-Ghz Circularly Polarized Dual-Rhombic-Loop Traveling-Wave Rectifying Antenna for Low Power-Density Wireless Power Transmission Applications," *IEEE Trans. Microw. Theory Tech.,* vol. 51, pp. 1548-1553, May 2003.

[41] J. O. McSpadden, F. Lu, and C. Kai, "Design and Experiments of a High-Conversion-Efficiency 5.8-Ghz Rectenna," *IEEE Trans. Microw. Theory Tech.,* vol. 46, pp. 2053-2060, Dec. 1998.

[42] B. Strassner and C. Kai, "Highly Efficient C-Band Circularly Polarized Rectifying Antenna Array for Wireless Microwave Power Transmission," *IEEE Trans. Antennas Propag.,* vol. 51, pp. 1347-1356, June 2003.

[43] P. Ji-Yong, H. Sang-Min, and T. Itoh, "A Rectenna Design with Harmonic-Rejecting Circular-Sector Antenna," *IEEE Antennas Wireless Propag. Lett.,* vol. 3, pp. 52-54, Dec. 2004.

[44] J. Heikkinen and M. Kivikoski, "Low-Profile Circularly Polarized Rectifying Antenna for Wireless Power Transmission at 5.8 Ghz," *Microwave and Wireless Components Letters, IEEE,* vol. 14, pp. 162-164, Apr. 2004.

[45] M. Ali, G. Yang, and R. Dougal, "A New Circularly Polarized Rectenna for Wireless Power Transmission and Data Communication," *IEEE Antennas Wireless Propag. Lett.,* vol. 4, pp. 205-208, 2005.

[46] Y. Murao and T. Takano, "An Investigation on the Design of a Transmission Antenna and a Rectenna with Arrayed Apertures for Microwave Power Transmission," *Electronics and Communications in Japan (Part I: Communications),* vol. 83, pp. 1-9, 2000.

[47] L. H. Hsieh, B. H. Strassner, S. J. Kokel, C. T. Rodenbeck, M. Y. Li, K. Chang, F. E. Little, G. D. Arndt, and P. H. Ngo, "Development of a Retrodirective Wireless Microwave Power Transmission System," in *IEEE Antennas and Propagation Society International Symposium*, 2003, pp. 393-396.

[48] K. Hashimoto and H. Matsumoto, "Microwave Beam Control System for Solar Power Satellite," in *2004 Asia-Pacific Radio Science Conference, Proceedings*, 2004, pp. 616-617.

[49] C. T. Rodenbeck, L. Ming-yi, and C. Kai, "A Phased-Array Architecture for Retrodirective Microwave Power Transmission from the Space Solar Power Satellite," in *IEEE MTT-S International Microwave Symposium Digest*, 2004, pp. 1679-1682.

[50] V. F. Fusco and S. L. Karode, "Self-Phasing Antenna Array Techniques for Mobile Communications Applications," *Electronics & Communication Engineering Journal,* vol. 11, pp. 279-286, Dec. 1999.

[51] R. Y. Miyamoto and T. Itoh, "Retrodirective Arrays for Wireless Communications," *Microwave Magazine, IEEE,* vol. 3, pp. 71-79, Mar. 2002.

[52] Y. J. Ren and K. Chang, "Bow-Tie Retrodirective Rectenna," *Electron. Lett.,* vol. 42, pp. 191-192, Feb. 2006.

[53] R. Yu-Jiun and C. Kai, "New 5.8-Ghz Circularly Polarized Retrodirective Rectenna Arrays for Wireless Power Transmission," *IEEE Trans. Microw. Theory Tech.,* vol. 54, pp. 2970-2976, July 2006.

[54] W. C. Brown, "The Technology and Application of Free-Space Power Transmission by Microwave Beam," *Proc. IEEE,* vol. 62, pp. 11-25, Jan. 1974.

[55] J. O. McSpadden, T. Yoo, and K. Chang, "Theoretical and Experimental Investigation of a Rectenna Element for Microwave Power Transmission," *IEEE Trans. Microw. Theory Tech.,* vol. 40, pp. 2359-2366, Dec. 1992.

[56] A. Sedra and K. Smith, *Microelectronic Circuits,* Fourth ed. New York: Oxford University Press, Inc., 1998.

[57] J. Dyson, "The Equiangular Spiral Antenna," *IRE Transactions on Antennas and Propagation,* vol. 7, pp. 181-187, Apr. 1959.

[58] T. Wen-Hua, L. Ming-yi, and C. Kai, "Broadband Microstrip-Coplanar Stripline-Fed Circularly Polarized Spiral Antenna," in *IEEE Antennas and Propagation Society International Symposium*, 2006, pp. 3669-3672.

[59] H. A. Wheeler, "Transmission-Line Properties of Parallel Wide Strips by a Conformal-Mapping Approximation," *IEEE Trans. Microw. Theory Tech.,* vol. 12, pp. 280-289, May 1964.

[60] H. A. Wheeler, "Transmission-Line Properties of Parallel Strips Separated by a Dielectric Sheet," *IEEE Trans. Microw. Theory Tech.,* vol. 13, pp. 172-185, Mar. 1965.

[61] P. C. Werntz and W. L. Stutzman, "Design, Analysis and Construction of an Archimedean Spiral Antenna and Feed Structure," in *IEEE Energy and Information Technologies in the Southeast., Southeastcon '89. Proceedings*, 1989, pp. 308-313.

[62] M. Y. Li, K. Tilley, J. McCleary, and K. Chang, "Broadband Coplanar Waveguide-Coplanar Strip-Fed Spiral Antenna," *Electron. Lett.,* vol. 31, pp. 4-5, Jan. 1995.

[63] H. Nakano, Y. Shinma, and J. Yamauchi, "A Monofilar Spiral Antenna and Its Array above a Ground Plane-Formation of a Circularly Polarized Tilted Fan Beam," *IEEE Trans. Antennas Propag.,* vol. 45, pp. 1506-1511, Oct. 1997.

[64] W. Wen-Zhou, C. Tze-Hsuan, and K. Jean-Fu, "Broadband Slot Spiral Antenna with External Feed and Microstrip-to-Slotline Transition," in *IEEE Antennas and Propagation Society International Symposium*, 2004, pp. 767-770.

[65] Z. Song, M. Liu, and Z. Ding, "An Improved Design of Microstrip Archimedeam Spiral Antenna," in *ICMMT '07 International Conference on Microwave and Millimeter Wave Technology*, 2007, pp. 1-4.

[66] T. W. Eubanks and C. Kai, "A Compact Parallel-Plane Perpendicular-Current Feed for a Modified Equiangular Spiral Antenna," *IEEE Trans. Antennas Propag.,* vol. 58, pp. 2193-2202, July 2010.

[67] T. K. Chen and G. H. Huff, "Stripline-Fed Archimedean Spiral Antenna," *IEEE Antennas Wireless Propag. Lett.,* vol. 10, pp. 346-349, 2011.

VITA

Seong Won Oh was born in Jin-Hae, Republic of Korea. He received a B.S. degree in electrical engineering from the Naval Academy and from Yonsei University, Korea in 1996 and 2000, respectively. He received his M.S. degree in electronic engineering from the Pohang University of Science and Technology, Korea, in 2004. He received his Ph.D. in electrical and computer engineering from Texas A&M University in August 2011 under the advisement of Prof. Kai Chang. His present research includes reflectarrays, wireless power transmission, and multiband antennas. He can be reached through Prof. Kai Chang, Department of Electrical and Computer Engineering, Texas A&M University, College Station, TX 77843-3128.